Microstructure Controlling and Mechanical Property Improving in TiNi-based Crystalline/Amorphous Alloys

Doctoral Thesis

Microstructure controlling and mechanical property improving in TiNi-based crystalline/amorphous alloy

Department of Materials Science
Graduate school of engineering,
Tohoku University

Jing Jiang
B6TD5305

CONTENTS

Abstract

TiNi based bulk metallic glass (BMG) composites which have dual crystalline and amorphous phases were fabricated with excellent mechanical properties, combining a fairly strain of 20% in ductility and a high stress of 2300 MPa in strength. The compressive stress-strain curves has a double sigmoidal shape with three deformation stages, an elastic deformation stage, a plateau stage of martensitic transformation process and final plastic deformation stage. Two crystalline phases are observed in the as cast state of TiNi crystalline/amorphous alloy, a high temperature stable austenite B2 phase and a low temperature stable martensite B19' phase. The martensitic phase always appears near amorphous phase. Phase transformation between austenite phase and martensite phase could be induced by both thermal and stress. This study was carried out comprehensively from alloys synthesis and characterization to investigation of the amorphous phase and crystalline phase controlling, the effects of different phase on the mechanical properties and finally the improvement of mechanical properties.

The cooling rate employed during casting process affects the formation of amorphous phase. Compared with the larger rods formed at lower cooling rates, the smaller rods formed at higher cooling rates contains more amorphous phase. The present of amorphous phase surrounding the crystalline phases confines the phase transformation between austenite and martensite. Thus, the smaller sample which including more amorphous phase shows a higher critical phase transformation stress during the compressive deformation.

High pressure torsion (HPT) process induces severe plastic deformation in the TiNi crystalline/amorphous alloys, leading to different phase compositions in different HPT conditions. HPT process at 77 K induces the main austenite phase change to martensite phase but the room temperature processed HPT keeps the austenite phase. The microstructure reveals an increasing volume fraction of amorphous phase by the HPT process.

TiNi crystalline/amorphous alloy exhibits a martensitic transformation behavior which induces superelastic effect in the deformation process. Cyclic loading-unloading behavior performing in the superelastic mode leads to the low cycle mechanical fatigue. The fatigue in the TiNi crystalline-amorphous alloy is suppressed due to the presence of the amorphous phase which acts as a sink for dislocations generated upon the superelastic cycling. It prevents the accumulation of dislocations, and simultaneously promotes creation of the new dislocations.

After performing the cryogenic thermal cycling on TiNi crystalline/amorphous alloy, the critical stress (σ_m) for martensitic phase transformation displays an increase which is the opposite behavior in the low cycle mechanical fatigue. The thermal treatment activates the initial martensite phase and enable it transform into the high temperature stable austenite phase during the cycling. Thus after cryogenic thermal cycling the fraction of martensite phase reduces. On the other hand, the microstructure of crystal near the amorphous phase transformed during the thermal treatment. These effects are responsible for the increases of critical phase transformation stress.

Chapter 1

Introduction

1.1 Amorphous alloys (Metallic glasses)

1.1.1 The development of amorphous alloys

Amorphous alloys or metallic glasses that are comparative newcomers to the amorphous group were first developed over 50 years ago. In 1959, Duwez's group demonstrated the $Au_{75}Si_{25}$ amorphous alloy obtained by rapid cooling of the liquid [1]. Fig. 1.1 shows the first XRD pattern of the amorphous Au-Si alloy. Based on Duwez's work, the melt-spinning technique was developed by Pond, Maddin and Chen [2, 3] as an improved cooling technique that realized the vitrification of larger quantities of an alloy to be made into the amorphous state. The fabrication of the amorphous alloy ribbon or wires brought through the commercial application. The iron-based compositions were found to have soft magnetic properties that made the metallic glasses realized to have considerable commercial importance[4]. Since then, in the 1970s and 1980s, the metallic glasses research gained momentum by the developing of the continuous casting processes of metallic glasses ribbons, wire, sheets for commercial manufacture. The fabrication was limited by the rapid quenching at cooling rates as high as 10^5-10^6 K/s [5]. Following succeeds in making Pd-based BMGs [6] in late 1980s, by the finding of multicomponent alloy system consisting of common metallic elements [7, 8], which exhibit strong glass forming ability and sluggish crystallization kinetics, metallic glass developed to reach several centimeters

in casting thickness with low critical cooling rate [9, 10]. The development of bulk metallic glasses (BMGs) leads to the second blooming of the field of amorphous alloys, and a series of BMGs like Zr-, Cu-, Fe-, Ti-, Ni-, Hf-, Co-, Ca-, Au-based alloy[11-16] with large size and high glass-forming ability were fabricated and found the commercial applications.

1.1.2 The formation of the amorphous alloys

The glass formation process shown in Fig. 1.2 illustrates the temperature dependence of a liquid's volume (or enthalpy) at constant pressure [17]. Upon cooling down from the high temperatures the atomic motions slow down and when it passes the melting temperature (T_m) crystallization process usually takes place by nucleation and growth (see the blue line). This is a typical first-order phase transition that results in a decrease in the specific volume. However the crystallization could be suppressed if the liquid is cooled fast enough in the supercooled liquid region [18], until at a certain temperature range (near T_{ga} or T_{gb}) the supercooling liquid loses its mobility. The liquid therefore appears "frozen" on the laboratory timescale that the atoms lose the mobility in a large scale and hardly form new structure by changing positions [19]. The resulted material is a glass. The falling out of equilibrium occurs in a narrow temperature range where the relaxation time in the order of 10^2-10^3 seconds and the derivative of volume or enthalpy with respect to temperature has an abrupt change [20]. The change is finished at glassy transition temperature T_g, which normally occurs around $2T_m/3$ [21]. T_g is different for different cooling rates. The higher cooling rate the higher temperature at which the atoms are "frozen" and it is easier to

fall out of liquid-state equilibrium. Consequently, T_g increases with the cooling rate [22, 23]. In practice, the dependence of T_g upon cooling rate is weak (T_g changes by only 3-5 K when cooling rates change by an order of magnitude), and the transformation range is narrow [24]. T_g is an important transition temperature of liquid, and most useful to estimate the material characteristics of amorphous alloys.

1.1.3 The structure of amorphous alloys

Crystalline materials present a macroscopic anisotropy, so that the physical properties are different based on the spatial direction. In contrast, amorphous materials have a macroscopically homogeneous structure since they lack of the long-range order. The rapidly cooled amorphous alloy is the one that retains the disordered atomic structure of a liquid and avoids crystallization which induces a long-range ordered crystal structure. Fig. 1.3 shows the simulated amorphous and crystalline structures [25]. Amorphous state is normally described as “noncrystalline” since the atomic arrangements are random and no periodicity is found. Each atom in the amorphous alloy will have somewhat different nearest neighbors and coordination number [26]. The electron diffraction pattern shown in Fig. 1.4 [27] reveals a broad dispersion halo typical for the amorphous structure, not like the bright spots of the crystalline one. The high resolution transmission electron microscopy (HRTEM) figure presents the atomic structure of an amorphous solid and of a crystal. However, the density and electrical conductivity of the amorphous and crystalline alloys show no big difference which reveals that their local structures are not too much different [28]. It means that the disorder structure of an amorphous alloy is not like the

convention disorder in a gas. The amorphous alloy shows intrinsic short-range order in the atomic structure. Some data reveal the structural and dynamics un-uniformity of an amorphous solid on the nano-scale [29-33]. There are some “soft areas” in amorphous alloys which have low density and strength [34, 35]. The structural inhomogeneity of amorphous alloys is one of the key factors affecting their mechanical properties [30, 36-38].

1.1.4 The mechanical properties of amorphous alloys and their composites

Amorphous alloys especially the bulk metallic glasses shows unique mechanical properties like ultra-high strength, extreme hardness, low elastic modulus and a unique deformation behavior [39]. Since the absence of defects like dislocations or grain boundaries in the disordered structure, most of the amorphous alloys exhibit strength and elastic limits significantly higher than those of conventional crystalline alloys [40, 41]. Co-based bulk metallic glass is one of the strongest materials nowadays. Its yield strength is about 6.0 GPa [42]. Fig. 1.5 [43] and 1.6 show the range of elastic limit plotted against modulus and the stress-strain curves of different materials. The mechanical properties in amorphous alloys show a good combination of strength and elasticity, at same time it has the drawback of low ductility.

Due to the atomic disorder, metallic glasses show completely different deformation behavior from that of crystalline alloys. Upon yielding metallic glasses suffer from strong tendency towards shear localization which induces macroscopically brittle failure at room temperature [41]. As shown in Fig. 1.7 [41] the plastic shear along the shear band plane leaves some slip steps on the surface of

amorphous alloys. It is a highly localized flow and there are not slipping dislocations to divert the flow. Once the initial shear band forms in a metallic glassy sample, it becomes unstable and rapidly propagates, typically leading to a catastrophic fracture [44]. The widely recognized mechanism to explain the beginning of plastic flow is the "shear transformation zone" (STZ) model [41, 45, 46]. As proposed by Argon [46, 47], the "plastic flow event" can be described by a local plastic or inelastic rearrangement of the flow units. These flow units are atomic clusters commonly termed as the STZ.

Glassy matrix composites with heterogeneous microstructures combing a glassy matrix with crystalline particles, have been formed to improve the plasticity of amorphous alloys [48, 49]. The structural inhomogeneities like crystalline particles are associated with blocking and branching of the propagating localized shear bands, which results in an increase in the overall plastic strain [50]. This enables multiplication, branching and termination of the shear bands similar to the crystalline composites where cracks are blocked and blunted by the secondary phases. Dendritic crystals imbed in the glassy matrix as the second phase shows stronger blocking or blunting effect compared to other shapes [51]. Various glassy matrix composites [52-55] exhibiting the macroscopic ductility at room temperature and high thermal stability of the glassy matrix (Zr-[56-60], Ti-[52, 61-67], Co-[68], Mg-[69], La-[51, 70] Fe-based [71, 72]) were produced. In addition, a series of plastic TiZr-based BMG composites have been designed to improve the tensile ductility (Fig. 1.8) [58]. They developed "designed composites" by matching fundamental mechanical and microstructural length scales and reported TiZr-based BMG composites with room

temperature tensile ductility exceeding 10%, yield strengths of 1.2-1.5 GPa placing BMG composites among the toughest known materials. The microstructure shown in Fig. 1.8a and b display the dendrites crystal embedded in the glass matrix, the dendrites structure as second phase in the BMG composites shows better enhance properties due to the homogeneous dendritic arborizations high efficiently impede the propagation and extension of shear bands. Fig. 1.8c shows the ambient-temperature stress-strain tensile curves for samples with different volume fractions of dendrites, they are 42%, 51% and 67% for DH1, DH2 and DH3, respectively. With the fraction of the dendritic phase increase the tensile plasticity improved. The in situ composites exhibit plastic elongation of nearly 13% in DH3 and the necked regions is shown in Fig.1.8h.

1.2 TiNi alloys and the “superelastic” behavior

1.2.1 Martensitic transformation in TiNi alloys

Titanium-nickel (TiNi) shape memory alloys draw great attention owing to their excellent mechanical properties and the ability to transform close to room temperature [73]. The reversible temperature and stress induced phase transformation between B2 (cP2) austenite and B19’ (mP4) martensite results in the shape memory effect and the superelasticity, respectively. The martensitic transformation path is shown in Fig. 1.9 The austenite B2-cP2 TiNi phase has a cubic CsCl-type ordered structure with a lattice constant of 0.3015 nm at room temperature [74]. The monoclinic B19’-mP4 martensite phase is formed by the shear or shuffle of master B2 austenite phase

experiencing a B19’ martensite transforming [75]. The shear is necessary to create B19 structure which is lower in energy than B2 but mechanically unstable due to a negative elastic modulus[76].

When master austenite phase is applied loading and the free energy difference reaches a critical value, it transforms into the B19’ martensite phase and shows a plateau area in the stress-strain curve [77]. Since the martensite phase is not stable in the A_f temperature, during unloading the martensite phase transforms back into austenite phase [78].

1.2.2 Superelastic and cyclic loading-unloading behavior

The TiNi shape memory alloys have unique ability to recover the shape after undergoing large deformation on removal of load, known as the superelastic effect [79]. The characteristics of superelastic process include: (1) hysteretic damping; (2) large elastic strain range; (3) excellent fatigue properties; (4) a stress plateau. The superelastic effect under cyclic loading is a generic characteristic feature of the TiNi shape memory alloys[80, 81]. The low-cycle mechanical fatigue is an important feature which affects, the critical stress for the martensitic transformation, the hysteresis or the amount of energy dissipated and the residual strain after unloading. The characteristic of fatigue properties during superelastic cycling is that the residual strain grows with the number of cycles, while both the stress for inducing martensitic transformation and the stress hysteresis decrease [82]. At the same time it changes the shape of the stress-strain curve, shrinks the plateau area, which means that the energy dissipated in one cycle decreases. There is a need to know how microstructural

damage accumulates during cyclic loading and eventually affects the fatigue resistance. The low-cycle fatigue is frequently ascribed to the rise of internal stresses in the material upon the superelastic cycling which is caused by the accumulation of dislocations and the dislocation strain fields [83, 84]. The internal stresses related to plastic deformation favor the formation of martensite. Slip dislocations created by propagating austenite and martensite interfaces were experimentally observed in the superelastically deformed TiNi alloy by transmission electron microscopy (TEM) [85]. Fig. 1.10 [86] helps to understand the microstructural scenario how the dislocations are introduced during superelastic cyclic loading. At the first cycle, the B19' martensite (gray) grows into the parent B2 phase (white) during loading process. Dislocations are needed for the structural accommodation; mechanical twinning and dislocation plasticity both are responsible for energy dissipation of martensitic transformation[87]. The dislocations associated with the lattice shear can stabilize the martensite. After reached the maximum strain of cyclic loading, the martensite area moves back on unloading process and leaves the dislocations behind. These dislocations mark positions in the microstructure and easy for martensite move in during loading on the second cycle, as a consequence the martensite propagates further and accumulates more dislocations.

1.3 TiNiCuZr based BMG composites

Base on the concept of superelastic behavior and transformation induced plasticity, TiNiCuZr-based BMG composites were explored by fabricating the

dual-phase amorphous-crystalline alloy with austenitic B2 phase. They combine the advantageous properties of metallic glasses those of a crystal inducing large strain by homogeneous flow at low temperatures and high final stresses [88]. The composite structure changes the morphology of amorphous shear band, reduces the chance of shear flow instability and enhances mechanical properties. The BMG composites with B2 phase display significant plasticity and pronounced work hardening under compression [89-95], exhibit relieved work-softening effect under tension [94-97]. The TiNiCuZr BMG composites with a B2 crystalline phase draw a lot of attention in the amorphous alloy field.

Eckert *et al.* prepared a series CuZr-based (CuZrAl, CuZrCo, CuZrTi, CuZrAg, CuZrAlAg, CuZrZn)[65, 90, 96, 98]; TiCu-based (TiCuNi, TiCuNiZr) [66, 99-101] CuZr-based BMG composites show a unique microstructure consisting of B2-CuZr or B2-Ti (Cu, Ni) phase crystals embedded in a glassy matrix. It is suggested that the homogeneous nucleation and dendritic growth of the nuclei leads to the microstructure as shown in Fig. 1.11. The crystals growing and glassy solidification are happening coevally from the outside to the inside of the rod. While the melt solidified radially from the outside to the inside (large arrows), the B2 CuZr crystals grew radially at random positions, most likely because of homogeneous nucleation and differences in local cooling rate. The enhanced of the limited ductility due to the formation of in situ BMG composites in CuZr based alloys. The performances were concluded to result from the following effects [88]: (1) the B2 crystalline phase confine shear bands preventing the formation of a critical shear front; (2) the

martensitic transformation and shear band formation are mutual deformation processes, facilitating each other; (3) martensitic transformation changes the shear band morphology by broadening the shear band and reducing the elastic shear stress, thereby stabilizes the plasticity; (4) martensitic transformation competes the shear bands development by controlling the heterogeneous distribution of atomic strain and the absorb the stresses in amorphous phase.

A great variety of the TiNi-based BMG composites with B2-TiNi crystalline phase were produced in the previous works [102-107]. The structures and mechanical properties were investigated in detail. The mechanical properties of TiNiCuZr system-based dual-phase materials demonstrate a good combination of strength and ductility. The high strength comes from the amorphous phase, and a large fraction of the crystalline B2-TiNi phase provides good ductility. As shown in Fig. 1.12 the typical stress-strain curve of the compressive deformation process has a sigmoidal shape indicating the three stages of the deformation: i) elastic deformation; ii) martensitic transformation inducing superelasticity; iii) plastic deformation.

Based on the previous work, the $Ti_{40}Ni_{39.5}Cu_8Zr_{10}Co_2Y_{0.5}$ alloy composition of the series of TiNiCuZr-based amorphous crystalline alloy was chosen as the main alloy for further research. It combines the highest strength of 2300 MPa and good ductility (20 %). Y was added to increase the glass forming ability [108]. The addition of Co leads to the increase in the yield strength[109]. It was also reported to improve the glass-forming ability of Zr alloys [110].

1.4 Objectives and the outline of this thesis

Following the previous research activities, more detailed studies of the structure and deformation of the TiNi-based crystalline/amorphous alloys are required. For example, how the amorphous phase affects the mechanical properties of the dual-phase alloy, and how to control the volume fraction of crystalline and amorphous phases. We also put effort to improve the mechanical properties of the TiNi dual-phase alloys.

The outline of this thesis is listed as follows:

In chapter 1, fundamental concepts concerning amorphous alloys (metallic glasses) and TiNi shape memory alloys also their composites were briefly introduced, followed by the objective and outline of this thesis.

In chapter 2, the experimental method, some parameters of the measurements and unique technology were organized.

In chapter 3, the volume fraction of amorphous phase in the TiNi crystalline/amorphous alloy was controlled by the cooling rate during the casting process. The phase compositions were controlled by the high pressure torsion (HPT) process. The mechanical properties were characterized by the compressive strength measurements.

In chapter 4, the low cycle mechanical fatigue properties in TiNi crystalline/amorphous alloy and TiNi fully-crystalline alloy were developed for studying the effect of amorphous phase in the dual-phase alloys. The suppression of the fatigue in composite alloy due to the presence of the amorphous phase which acts

as a sink for dislocations generated upon the superelastic cycling.

In chapter 5, the cryogenic thermal cycling was performed in the TiNi crystalline/amorphous alloy to improve the mechanical properties. The compressive stress strain curves display an increase of the phase transformation stress after cryogenic thermal cycling. It is the opposite behavior with the low cycle mechanical fatigue. The fraction of martensite phase which formed in the casing process associated with amorphous phase decreased and the microstructure was changed by the cyclic thermal treatment, they are the reasons for increasing the phase transformation stress.

References

1. W.K. Jun, R. Willens, and P. Duwez, Nature, 1960. 187(4740): p. 869.

2. R. Pond, Trans. Met. Soc. AIME, 1969. 245: p. 2475-2476.

3. H. Chen, and C. Miller, Review of Scientific Instruments, 1970. 41(8): p.1237-1238.

4. H.H. Liebermann, Marcel Dekker, Inc, 270 Madison Ave, New York, New York 10016, USA, 1993. 788, 1993.

5. F. Luborsky, Amorphous metallic alloys. 1983: Butterworth and Co (Publishers): London, UK.

6. F. Spaepen, Acta metallurgica, 1977. 25(4): p. 407-415.

7. W.L. Johnson, MRS Bull., 1999. 24: p. 42.

8. A. Inoue, T. Zhang, and T. Masumoto, JIM, 1989. 30(12): p. 965-972.

9. W.L. Johnson, Fundamental aspects of bulk metallic glass formation in multicomponent alloys. in Materials science forum. 1996. Trans Tech Publ.

10. A. Inoue, Acta materialia, 2000. 48(1): p. 279-306.

11. W.K. Wang, H. Iwasaki, and K. Fukamichi, Journal of materials science, 1980. 15(11): p. 2701-2708.

12. A. Peker, and W.L. Johnson, Applied Physics Letters, 1993. 63(17): p. 2342-2344.

13. W. Jiao, K. Zhao, X.K. Xi, D.Q. Zhao, M.X. Pan, Journal of Non-Crystalline Solids, 2010. 356(35-36): p. 1867-1870.

14. B. Zhang, D.Q. Zhao, M.X. Pan, W.H. Wang, A.L. Greer, Physical review letters, 2005. 94(20): p. 205502.

15. Q. Luo, and W. Wang, Journal of Non-Crystalline Solids, 2009. 355(13): p. 759-775.

16. M.B. Tang, D.Q. Zhao, M.X. Pan and W.H. Wang, Chinese Physics Letters, 2004. 21(5): p. 901.

17. P.G. Debenedetti, and F.H. Stillinger, Nature, 2001. 410(6825): p. 259.

18. D. Turnbull, Contemporary physics, 1969. 10(5): p. 473-488.

19. C.A. Angell, Journal of non-crystalline solids, 1988. 102(1-3): p. 205-221.

20. C.A. Angell, Science, 1995. 267(5206): p. 1924-1935.

21. M.H. Cohen, and D. Turnbull, Journal of Chemical Physics, 1959. 31(5): p. 1164-1169.

22. M. Goldstein, and R. Simha, The glass transition and the nature of the glassy state. Vol. 279. 1976: New York Academy of Sciences.

23. R. Brüning, and K. Samwer, Physical Review B, 1992. 46(18): p. 11318.

24. M.D. Ediger, C.A. Angell, and S.R. Nagel, Journal of physical chemistry, 1996. 100(31): p. 13200-13212.

25. F. Wooten, and D. Weaire, Journal of Non-Crystalline Solids, 1989. 114: p.681-683.

26. D.V. Louzguine-Luzgin, M. Ito, S.V. Ketov, A.S. Trifonov, J. Jiang, C.L. Chen, K. Nakajima, Intermetallics, 2018, 93: p.312-317.

27. A. Hirata, P. Guan, T. Fujita, Y. Hirotsu, A. Inoue, Nature materials, 2011. 10(1): p.28

28. D.V. Louzguine-Luzgin, A.R. Yavari, G. Vaughan, A. Inoue, Intermetallics, 2009. 17(7): p. 477-480.

29. W.H. Wang, Nature materials, 2012. 11(4): p. 275.

30. H. Peng, M. Li, and W. Wang, Physical review letters, 2011. 106(13): p. 135503.

31. H. Wagner, D. Bedorf, S. Kuchemann, M. Schwabe, Nature materials, 2011. 10(6): p. 439.

32. Y.H. Liu, D. Wang, K. Nakajima, W. Zhang, A. Hirata, Physical Review Letters, 2011. 106(12): p. 125504.

33. T. Ichitsubo, T. Ichitsubo, E. Matsubara, T. Yamamoto, H.S. Chen, N. Nishiyama, J. Saida, and K. Anazawa, Phys. Rev. Lett., 2005. 95: p. 245501.

34. H.B. Yu, X. Shen, Z. Wang, L. Gu, W.H. Wang, H.Y. Bai, Physical review letters, 2012. 108(1): p. 015504.

35. Y.H. Liu, G. Wang, R.J. Wang, M.X. Pan, W.H. Wang, science, 2007. 315(5817): p. 1385-1388.

36. M.H. Lee, J.K. Lee, K.T. Kim, J. Thomas. J. Das, U. Kuhn, J. Eckert, Physical status solidi (RRL) – Rapid Research Letters, 2009. 3: p. 46-48.

37. J. Park, D. Kim, and J. Eckert, Intermetallics, 2012. 29: p. 70-74.

38. Z.W. Zhu, L. Gu, G.Q. Xie, W. Zhang, A .Inoue, H.F. Zhang. Acta Materialia, 2011. 59(7): p. 2814-2822.

39. J. Schroers, Bulk metallic glasses. Physics today, 2013. 66(2): p. 32.

40. M. Telford, Materials today, 2004. 7(3): p. 36-43.

41. C.A. Schuh, T.C. Hufnagel, and U. Ramamurty, Acta Materialia, 2007. 55(12): p. 4067-4109.

42. J. Wang, R. Li, N. Hua, T. Zhang, Journal of Materials Research, 2011. 26(16): p. 2072-2079.

43. M.D. Demetriou, M.E. Launey, G. Garrett, J.P. Schramm, D.C. Hofmann, W. L. Johnson, R.O. Ritchie, Nature materials, 2011. 10(2): p. 123.

44. W.H. Wang, C. Dong, and C. Shek, Materials Science and Engineering: R: Reports, 2004. 44(2-3): p. 45-89.

45. K. Ngai, Relaxation and diffusion in complex systems. 2011: Springer Science & Business Media.

46. A. Argon, Acta metallurgica, 1979. 27(1): p. 47-58.

47. A. Argon, and H. Kuo, Materials science and Engineering, 1979. 39(1): p. 101-109.

48. C. Hays, C. Kim, and W.L. Johnson, Physical Review Letters, 2000. 84(13): p. 2901.

49. F. Szuecs, C. Kim, and W. Johnson, Acta Materialia, 2001. 49(9): p. 1507-1513.

50. A. Inoue, W. Zhang, T. Tsurui, A.R. Yavari, A. L. Greer, Philosophical Magazine Letters, 2005. 85(5): p. 221-237.

51. M. Lee, Y. Li, and C. Schuh, Acta Materialia, 2004. 52(14): p. 4121-4131.

52. G. He, J. Eckert, W. Loser, L. Schultz, Nature materials, 2003. 2(1): p. 33.

53. W.H. Wang, Progress in Materials Science, 2007. 52(4): p. 540-596.

54. Y.J. Zhou, Y. Zhang, Y.L. Wang, G.L. Chen, Applied physics letters, 2007. 90(18): p. 181904.

55. U. Kuhn, J. Eckert, N. Mattern, L. Schultz, Applied Physics Letters, 2002. 80(14): p. 2478-2480.

56. W. Loser, J. Das, A. Guth, H.J. Klaub, C. Mickel, U. Kuhn, Intermetallics, 2004. 12(10-11): p. 1153-1158.

57. F.F. Wu, Z.F. Zhang, S.X. Mao, A. Peker, J. Eckert Physical Review B, 2007. 75(13): p. 134201.

58. D.C. Hofmann, J.Y. Suh, A. Wiest, G. Duan, M.L. Lind, M.D. Demetriou and W.L. Johnson, Nature, 2008. 451(7182): p. 1085.

59. J.W. Qiao, S. Wang, Y. Zhang, P.K. Liaw. G. L. Chen, Applied Physics Letters, 2009. 94(15): p. 151905.

60. S. Roberts, C. Zachrisson, H. Kozachkov, A. Ullah, A. A.Shapiro, W.L. Johnson, D.C. Hofmann, Scripta Materialia, 2012. 66(5): p. 284-287.

61. F. Guo, S. Poon, and G. Shiflet, Philosophical Magazine Letters, 2008. 88(8): p. 615-622.

62. D.C. Hofmann, J.Y. Suh, A. Wiest, Proceedings of the National Academy of Sciences, 2008. 105(51): p. 20136-20140.

63. J.W. Qiao, A.C. Sun, E.W. Huang, Y. Zhang, P.K. Liaw, Acta Materialia, 2011. 59(10): p. 4126-4137.

64. J.W. Qiao, J.T. Zhang, F. Jiang, Y. Zhang, P.K. Liaw, Materials Science and Engineering: A, 2010. 527(29-30): p. 7752-7756.

65. Y.S. Oh, C.P. Kim, S. Lee, N.J. Kim, Acta Materialia, 2011. 59(19): p. 7277-7286.

66. C. Jeon, C.P. Kim, S.H. Joo, H.S. Kim, .S Lee, Acta Materialia, 2013. 61(8): p. 3012-3026.

67. J.W. Qiao, T. Zhang, F.Q. Yang, P.K. Liaw, S. Pauly, B. S. Xu, Scientific reports, 2013. 3: p. 2816.

68. J. Fan, Z. Zhang, B. Shen, S.X. Mao, Scripta Materialia, 2008. 59(6): p. 603-606.

69. M. Ferry, K.J. Laws, C. White, D.M. Miskovic. K.F. Shamlaye, W. Xu and O. Biletska, MRSCommunications, 2013. 3(1): p. 1-12.

70. Y. Zhang, W. Xu, H. Tan, Y. Li, Acta materialia, 2005. 53(9): p. 2607-2616.

71. S.F. Guo, L. Liu, N. Li, Y. Li, Scripta Materialia, 2010. 62(6): p. 329-332.

72. J.E. Gao, Z.P. Chen, Q. Du, H.X. Li, Y. Wu, H. Wang, X.J. Liu Acta Materialia, 2013. 61(9): p. 3214-3223.

73. K. Otsuka, and X. Ren, Progress in materials science, 2005. 50(5): p. 511-678.

74. T. Philip, and P.A. Beck, Journal of The Minerals, Metals & Materials Society, 1957. 9(10): p. 1269-1271.

75. K. Otsuka, and X. Ren, Intermetallics, 1999. 7(5): p. 511-528.

76. X. Huang, G.J. Ackland, and K.M. Rabe, Nature materials, 2003. 2(5): p. 307.

77. J.Y. Huang, Y.T. Zhu, X.Z. Liao, R. Z. Valiev, Magazine Letters, 2004. 84(3): p. 183-190.

78. W.S. Ko, S.B. Maisel, B. Grabowski, J.B. Jeon, J. Neugebauer, Acta Materialia, 2017. 123: p. 90-101.

79. R. DesRoches, J. McCormick, and M. Delemont, Journal of Structural Engineering, 2004. 130(1): p. 38-46.

80. S. Miyazaki, K. Mizukoshi, T. Ueki, T. Sakuma, Y. Liu, Materials Science and Engineering: A, 1999. 273: p. 658-663.

81. K. Melton, and O. Mercier, Acta Metallurgica, 1979. 27(1): p. 137-144.

82. B. Strnadel, S. Ohashi, H. Ohtsuka, S. Miyazaki, T. Ishihara, Materials Science and Engineering: A, 1995. 203(1-2): p. 187-196.

83. K. Gall, and H. Maier, Acta Materialia, 2002. 50(18): p. 4643-4657.

84. R.F. Hamilton, H. Sehitoglu, Y. Chumlyakov, H.J. Maier, Acta Materialia, 2004. 52(11): p. 3383-3402.

85. J. Hurley, A.M. Ortega, J. Lechniak, K. Gall, Zeitschrift für Metallkunde, 2003. 94(5): p. 547-552.

86. A.Yawny, M. Sade, and G. Eggeler, Zeitschrift für metallkunde, 2005. 96(6): p. 608-618.

87. M. Ahlers, Philosophical Magazine A, 2002. 82(6): p. 1093-1114.

88. D. Sopu, K. Albe, and J. Eckert, Acta Materialia, 2018. 159: p. 344-351.

89. S. Pauly, G. Liu, G. Wang, J. Das, K.B. Kim, J. Eckert, Applied Physics Letters, 2009. 95(10): p. 101906.

90. S. Pauly, G. Liu, G. Wang, U. Kuhn, N. Mattern, J. Eckert, Acta Materialia, 2009. 57(18): p. 5445-5453.

91. K.K. Song, S. Pauly, Y. Zhang, R. Li, S. Gorantla, N. Narayanan, U. Kuhn, T. Gemming, J. Eckert, Acta Materialia, 2012. 60(17): p. 6000-6012.

92. P. Gargarella, S. Pauly, K.K. Song, J. Hu, N.S. Barekar, M.Samadi Khoshkhoo, A.Teresiak, H.Wendrock, U.Kuhn, C.Ruffing, E.Kerscher, J.Eckert, Acta Materialia, 2013. 61(1): p. 151-162.

93. Z.Y. Zhang, Y. Wu, J. Zhou, H. Wang, X.J. Liu, Z.P. Lu, Scripta Materialia, 2013. 69(1): p. 73-76.

94. Y. Wu, Y. Xiao, G. Chen, C.T. Liu, Z. Lu, Advanced materials, 2010. 22(25): p. 2770-2773.

95. Y. Wu, H. Wang, H.H. Wu, Z.Y. Zhang, X.D. Hui, G.L. Chen, Acta Materialia, 2011. 59(8): p. 2928-2936.

96. Z. Liu, R. Li, G. Liu, W. Su, H. Wang, Y. Li, M. Shi, X. Luo, G. Wua, T. Zhang, Acta Materialia, 2012. 60(6-7): p. 3128-3139.

97. Y. Wu, D.Q. Zhou, W.L. Song, H. Wang, Z.Y. Zhang, D. Ma, Physical review letters, 2012. 109(24): p. 245506.

98. D.Y. Wu, K.K. Song, P. Gargarella, C.D. Cao, R. Li, I.Kaban, J.Eckert, Journal of Alloys and Compounds, 2016. 664: p. 99-108.

99. H. Sun, K. Song, X. Han, H. Xing, X. Li, S. Wang, J.T. Kim, N. Chawake, T. Maity, L.Wang and J. Eckert, Metals, 2018. 8(3): p. 196.

100. P. Gargarella, S. Pauly, M.S. Khoshkhoo, C.S. Kiminami, U. Kuhn, J. Eckert, Journal of Alloys and Compounds, 2016. 663: p. 531-539.

101. P. Gargarella, S. Pauly, M.S. Khoshkhoo, U. Kuhn, J. Eckert, Acta Materialia, 2014. 65: p. 259-269.

102. A.A. Tsarkov, A.Y. Churyumov, V.Y. Zadorozhnyy, D.V. Louzguine-Luzgin, Journal of Alloys and Compounds, 2016. 658: p. 402-407.

103. D.V. Louzguine-Luzgin, A Vinogradov, G. Xie, S. Li, A. Lazarev, S. Hashimoto, A. Inoue, Philosophical Magazine, 2009. 89(32): p. 2887-2901.

104. A.Y. Churyumov, A.I. Bazlov, A.N. Solonin, G. Q. Xie, S. Li, D.V. Louzguine-Luzgin, The Physics of Metals and Metallography, 2013. 114(9): p. 773-778.

105. J. Jiang, S. Ketov, H. Kato, D.V. Louzguine-Luzgin, Materials Science and Engineering: A, 2017. 704: p. 147-153.

106. I.S. Golovin, V.Y. Zadorozhnyy, A.Y. ChuryumovJournal of Alloys and Compounds, 2013. 579: p. 633-637.

107. I.S. Golovin, V.Y. Zadorozhnyy, A.Y. ChuryumovJournal of Alloys and Compounds, 2013. 579: p. 633-637.

108. G.J. Hao, Y. Zhang, J.P. Lin, Y.L. Wang, Z. Lin, G.L. Chen, Materials Letters, 2006. 60(9-10): p. 1256-1260.

109. C. Bewerse, L.C. Brinson, D.C. Dunand, Materials Science and Engineering: A, 2015. 627: p. 360-368.

110. A. Inoue, T. Shibata, and T. Zhang, JIM, 1995. 36(12): p. 1420-1426.

111. R.Z. Valiev, Y.V. Ivanisenko, E.F. Rauch, B. Baudelet, Acta Materialia, 1996. 44(12): p. 4705-4712.

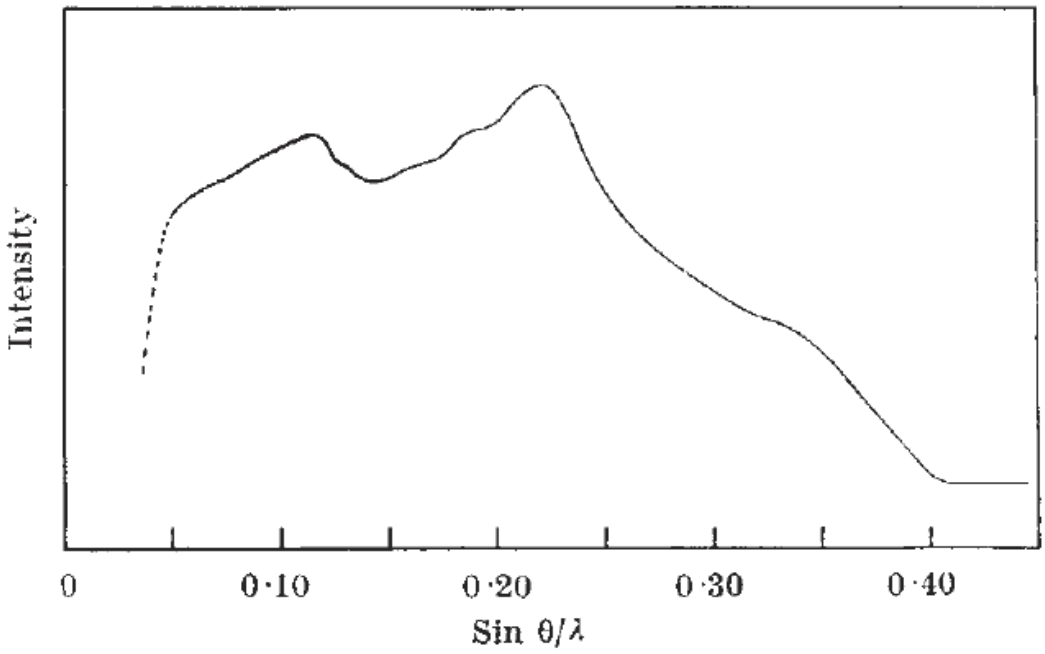

Fig. 1.1. X-ray diffraction pattern of gold-silicon alloy

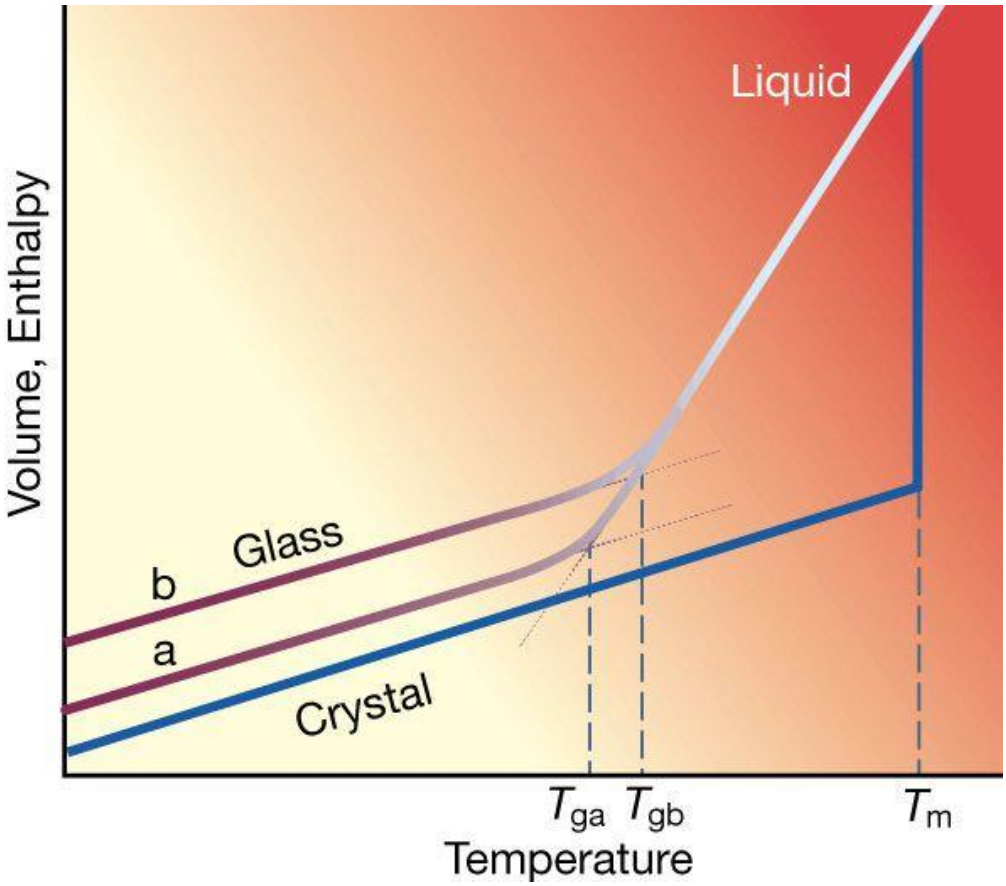

Fig. 1.2. Temperature dependence of a liquid's volume or enthalpy at constant pressure.

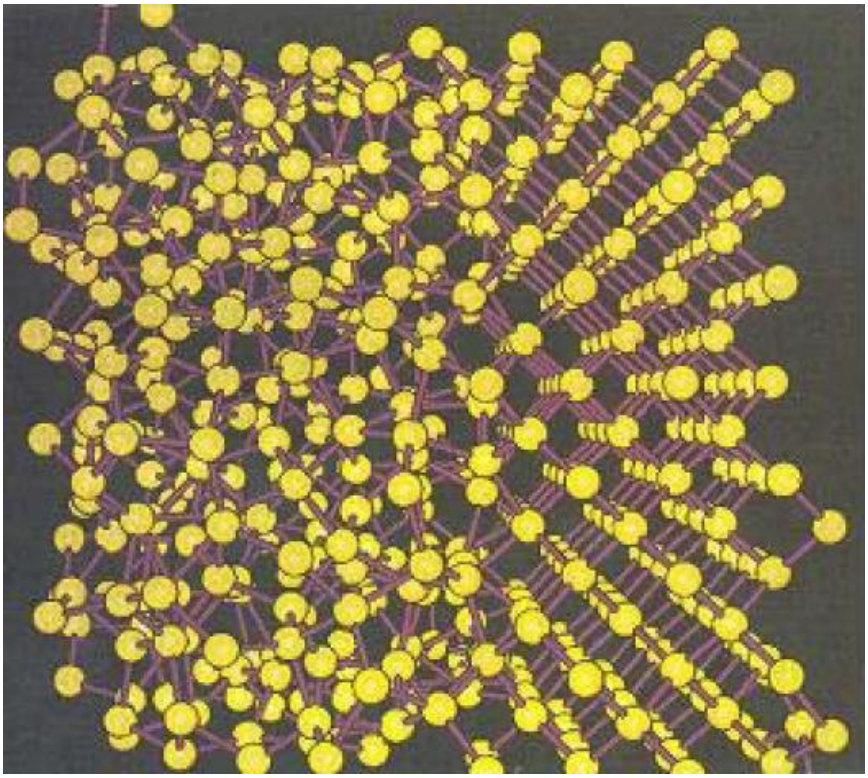

Fig. 1.3. A computer-generated picture of the crystalline/amorphous silicon interface model. Left side is the disordered amorphous structure, right is the ordered crystalline structure.

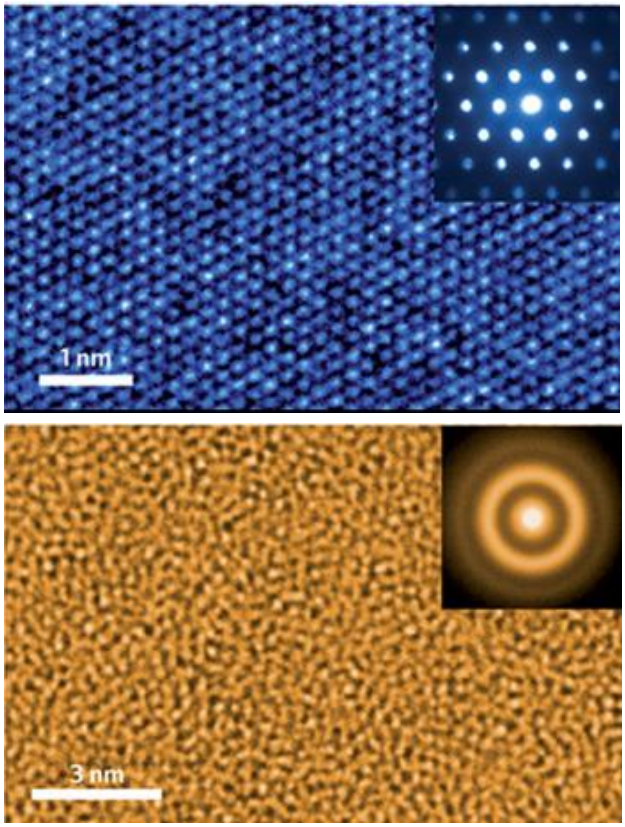

Fig. 1.4. Diffraction patterns and atomic images of crystalline and amorphous materials

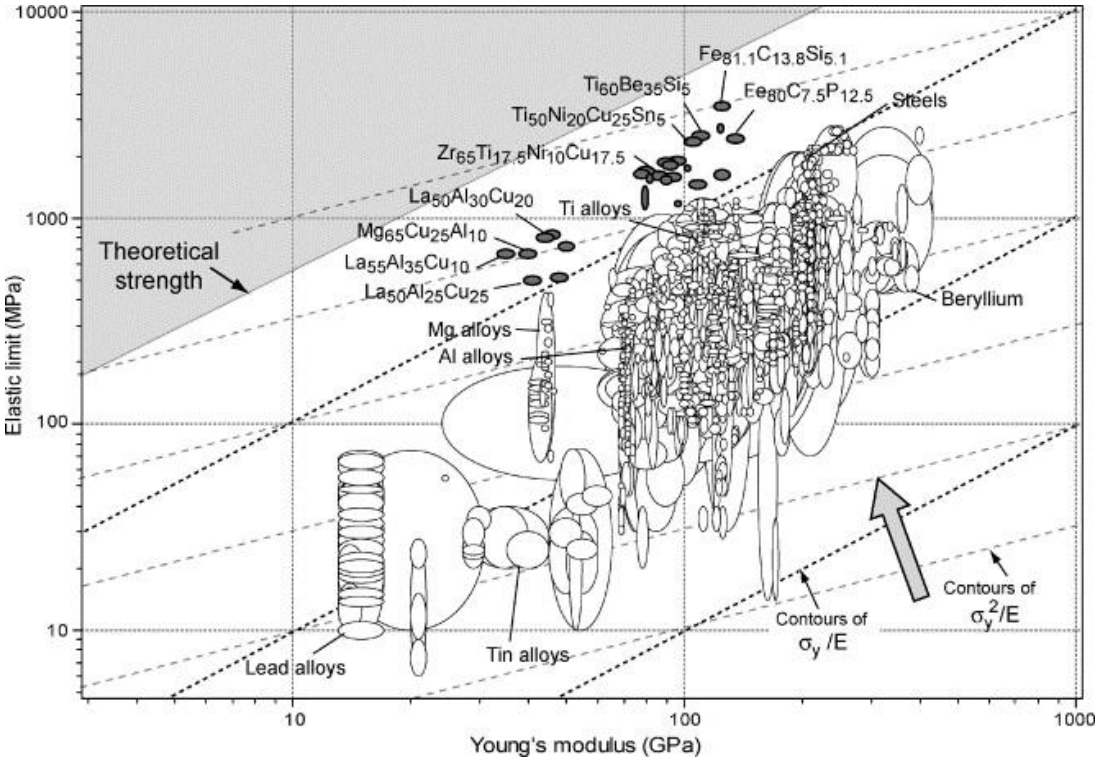

Fig. 1.5. Ranges of elastic limit σy plotted against modulus E

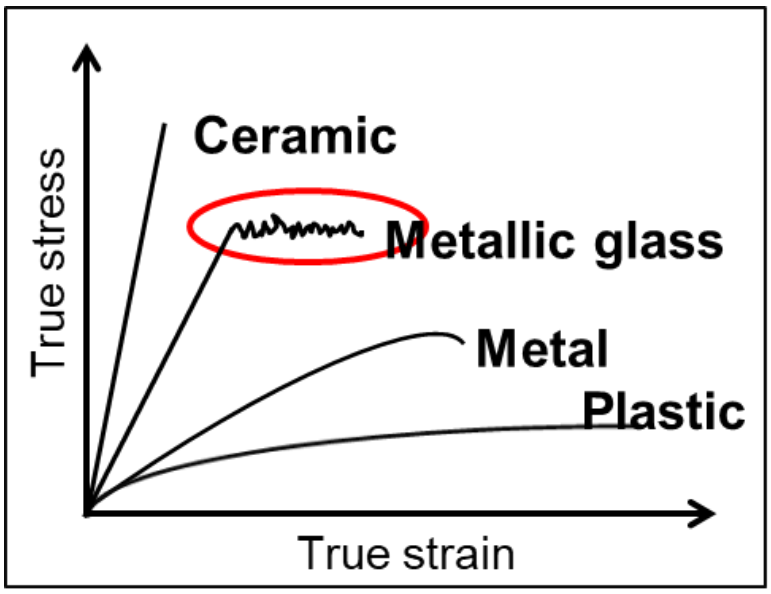

Fig. 1.6. The true stress-strain curves of different materials

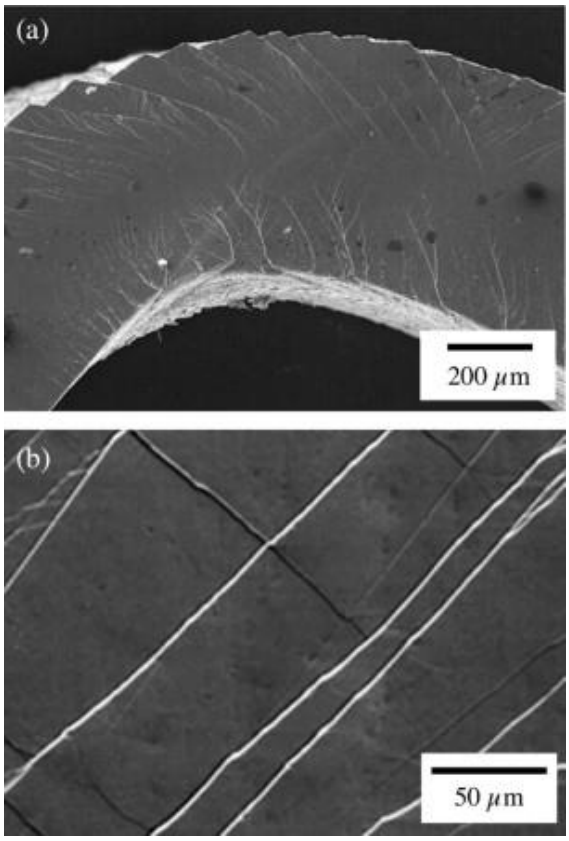

Fig. 1.7. Scanning electron micrographs illustrating the “slip steps” or surface offsets associated with shear bands in deformed metallic glasses. In (a) a bent strip illustrates slip steps formed in both tensile and compressive modes of loading, on the top and bottom surfaces, respectively. In (b) the side of a compression specimen is shown, for which the loading axis was vertical; here the slip steps document shear deformation at an inclined angle to the applied compressive load.

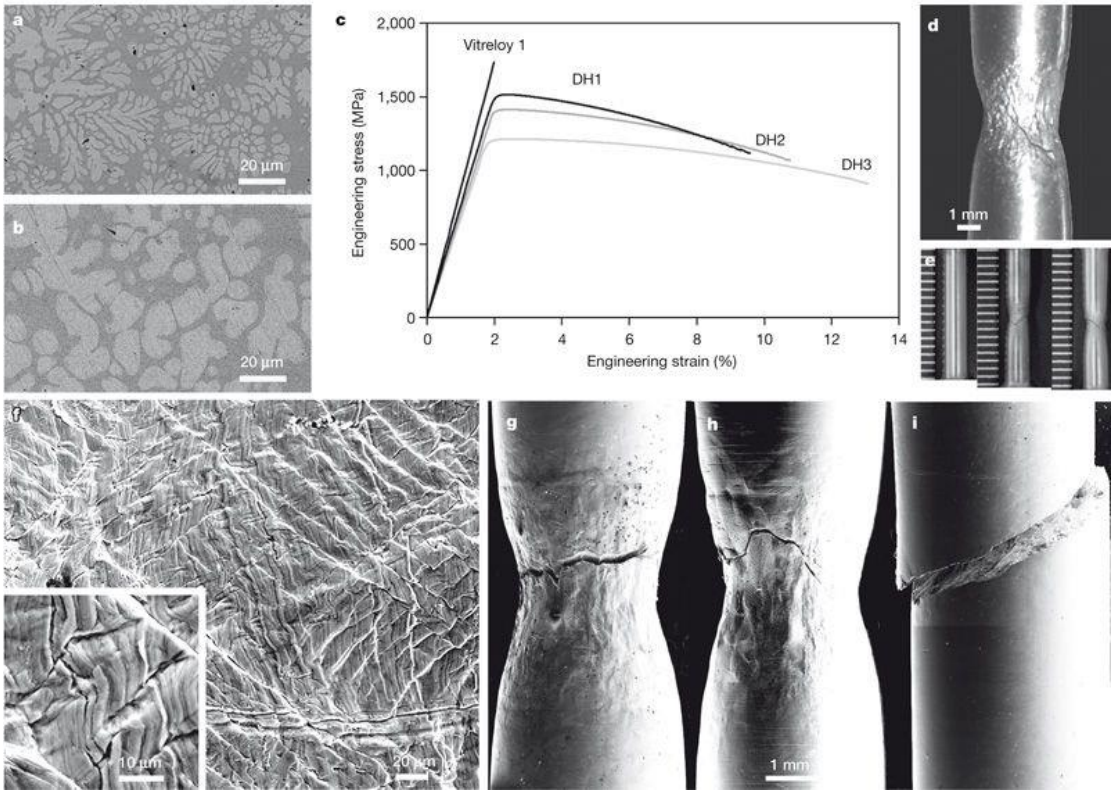

Fig. 1.8. Backscattered SEM micrographs showing the microstructure of TiZr-based BMG composites where the dark contrast is from the glass matrix and the light contrast is from the dendrites. (c) Engineering stress–strain curves for Vitreloy 1 and TiZr-based BMG composites in room-temperature tension tests. (d) Optical micrograph of necking. (e) Optical micrographs showing an initially undeformed tensile specimen contrasted with TiZr-based BMG composites specimens after tension testing. (f) SEM micrograph of the tensile surface with higher magnification shown in the inset. (g,h) SEM micrographs of necking. (i) Brittle fracture representative of all monolithic BMGs.

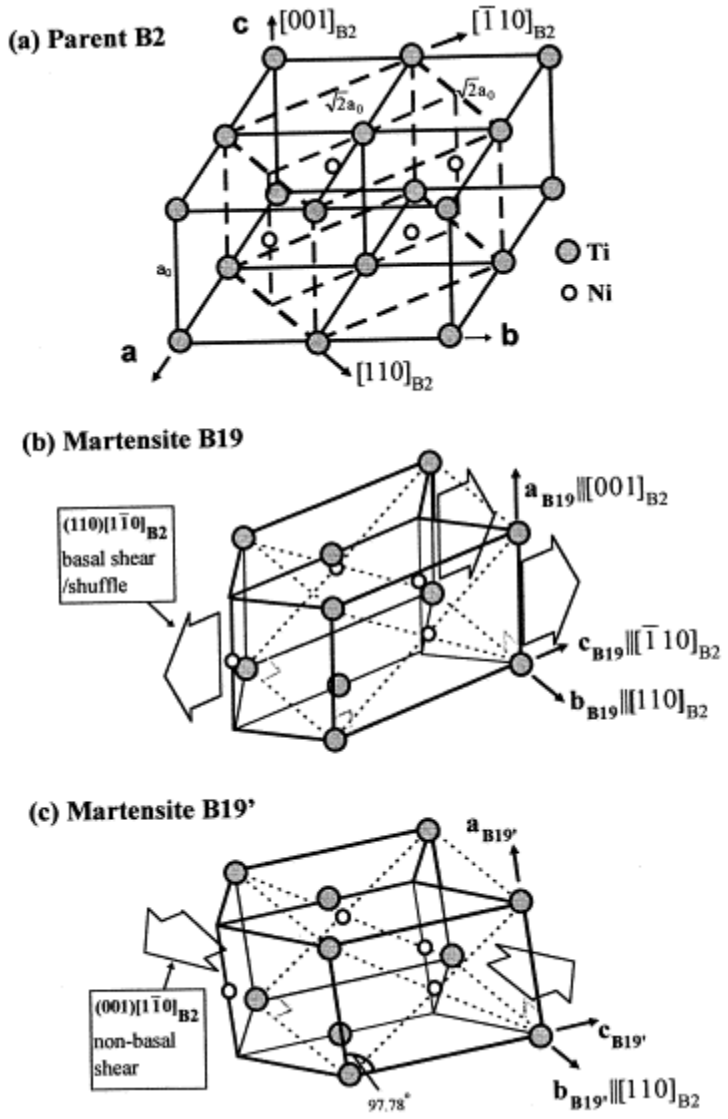

Fig. 1.9. Structural relationship among cubic parent phase (B2) and two kinds of martensites B19 and B19'. (a) The parent B2 cells with a FCT cell outlined, where close-packed planes or basal planes are indicated with thin dashed lines; (b) orthorhombic martensite B19, formed by shear/shuffle of the basal plane (110) B2 along $[\bar{1}10]$ B2 direction; (c) monoclinic B19' martensite of Ti-Ni, formed by a non-basal shear (001) $[\bar{1}10]$ B2 to the B19 structure to produce a monoclinic β angle.

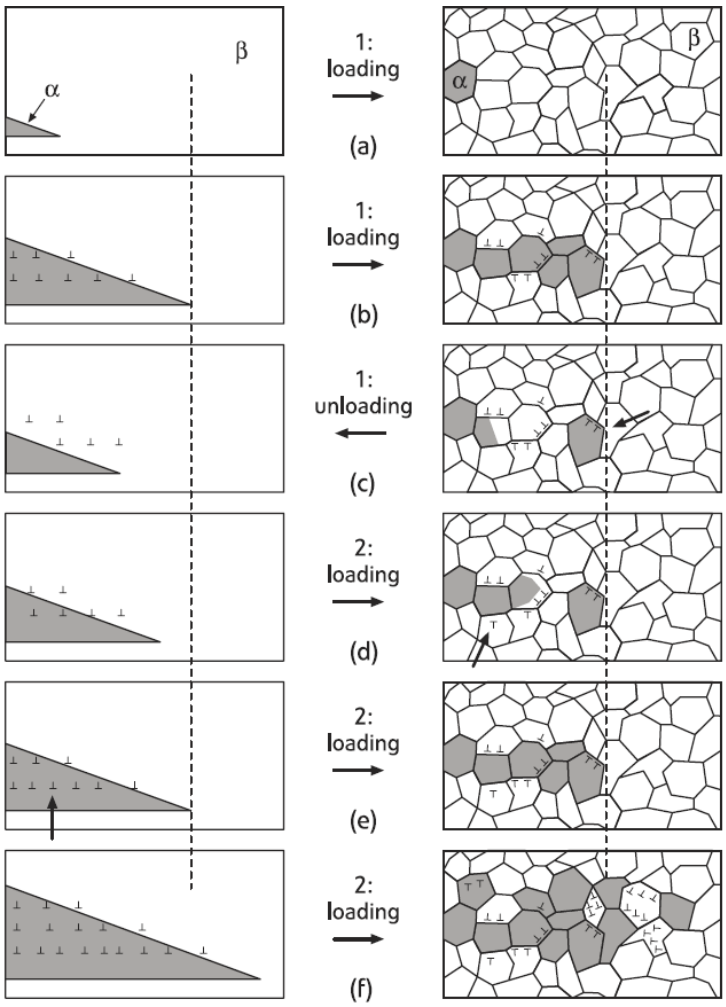

Fig. 1.10. A simple micromechanical scenario which rationalizes how pseudoelastic NiTi remembers previous cycles in strain-controlled testing (at lower maximum strain) in a single crystal (left) and in an ultrafine-grained material (right). (a) and (b): loading part of cycle 1, (c): unloading part of cycle 1, (d), (e) and (f): loading part of cycle 2.

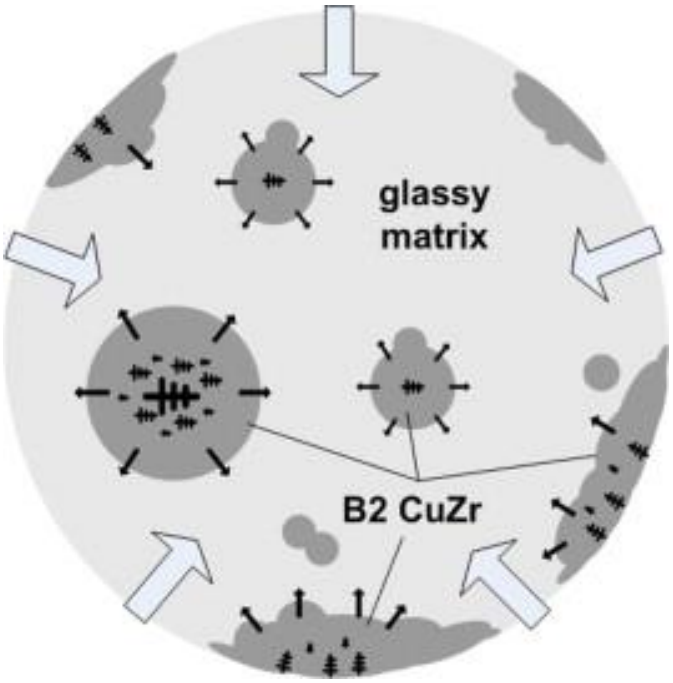

Fig. 1.11. Schematic illustration of the solidification mechanism of the CuZrAl melt. While the melt solidified radially from the outside to the inside (large arrows), the B2 CuZr crystals grew radially at random positions, most likely because of homogeneous nucleation and differences in local cooling rate.

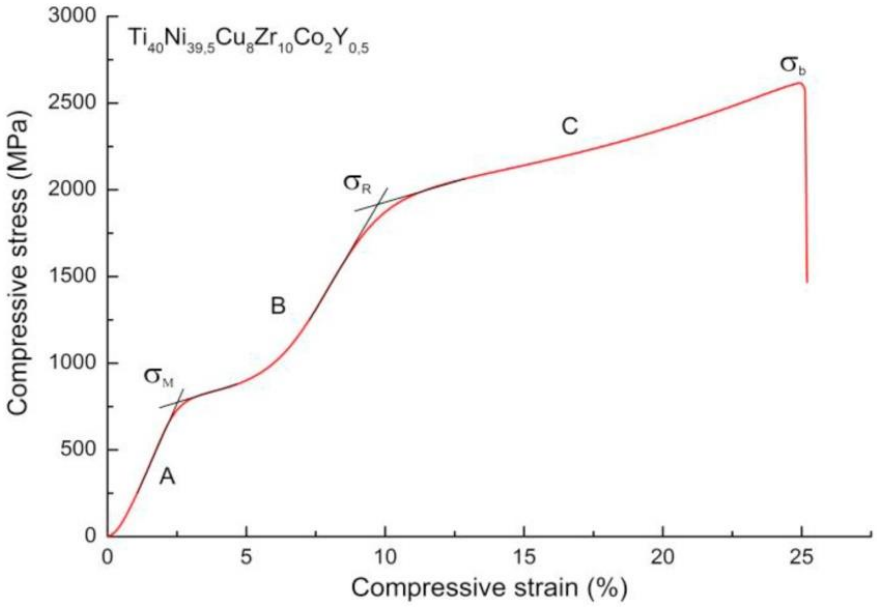

Fig. 1.12. Compressive stress–strain curves of the composite materials that demonstrate large irreversible deformation.

Chapter 2

Experimental methods

2.1 Sample preparation

2.1.1 Arc melting

The master alloys were prepared by arc-melting mixtures of raw metals (purity >99.9 mass %) in an Ar atmosphere purified with a Ti getter. The raw metals were processed by polishing and ultrasonic cleaning to ensure the surface purity which is important to forming the amorphous phase. The illustration of arc-melting procedure is shown in Fig. 2.1a. The master alloy prepared by the arc melting is shown in Fig. 2.1b. Raw metals were melted on a water-cooled copper hearth, then turned and remelted at least 5 times to make sure the chemical homogeneity. After arc melting process, the master alloys were polished to remove the impurity surface which was forming during the arc-melting process.

2.1.2 Casting in different methods

Cylindrical specimens (length: 50 mm) with different diameters (2 mm, 3 mm, and 5 mm) were obtained via pressurized injection-casting of the master alloys into a copper mold using Ar gas. The illustration of injection-casting procedure is shown in Fig. 2.2a. The photo of rod samples with different diameters prepared by the arc melting is shown in Fig. 2.2b.

Ribbon samples with thickness of 20-50 μm, width of 2-3 mm were prepared

from the master alloy ingot pieces by melt-spinning onto the rotating Cu wheel in an Ar atmosphere. The illustration of melt spinning procedure is shown in Fig. 2.3a. The photo of ribbons prepared by the arc melting is shown in Fig. 2.3b. The length of the ribbons is normally hundreds of millimeter. The thickness is controlled by the rotation speed of Cu wheel and the melt injection pressure.

Plate samples of 4 mm in thickness, 30-40 mm in width and 50-80mm in length were prepared by using a tilt casting method in an argon atmosphere purified with a Ti getter. Tilt-casting transferred the molten master alloy into copper mould by simple gravity viscous flow without surface turbulence therefore improves the forming ability of amorphous phase. The illustration of tilt casting procedure is shown in Fig. 2.4a. The photo of plate sample prepared by the tilt casting is shown in Fig. 2.4b.

2.1.3 The high pressure torsion process

One of the methods to obtain the amorphous microstructure is macroscale severe plastic deformation (SPD) like high pressure torsion (HPT) that induces high strain at hydrostatic pressure. As shown in Fig. 2.5, the process of HPT was conducted by an apparatus with two massive anvils, each anvil was machined to have a central depression 0.25 mm in depth and 10 mm in diameter. An imposed pressure of 5 GPa was applied for 10 s during compressive stage in the HPT process. Then the lower anvil was rotated at a rotation speed of 1 rpm under the same constant pressure for 1 turn during torsional stage. Two different temperature conditions were used to perform the HPT: room temperature (273 K) and liquid nitrogen temperature (77 K). Fig. 2.6 shows the photo of as cast sample and HPTed sample, reveals the shape

change of the sample before and after the HPT process. The as cast sample having 10 mm in diameter and 1.8 mm in thickness, was compressed to 1.12 mm in thickness. We define the strain imposed on the disk during HPT process as a simple shear deformation, normally shear strain γ can be given by the expression $\gamma = 2\pi rN/t$ [111], where N is the number of revolutions, r and t are the distance to the torsion axis and the height (or thickness) of the disk, respectively. As follows from this equation the shear strain varies across the disk from a maximum at the edge to minimum in the center where r is 0. In our work, the maximum shear strain γ located the edge area is nearly 18 %.

2.1.4 The cryogenic thermal cycling process

The cryogenic thermal cycling process was performed between room temperature and liquid nitrogen temperature. Samples dipped two minutes in ethanol solution which was kept around 30 ℃ by hot plate then directly transformed into liquid nitrogen for 2 minutes. This is one thermal cyclic loop.

2.2 Microstructure observation

The phase compositions of the samples were examined by X-ray diffraction (XRD) with Cu-Kα radiation, λ = 1.5406 Å (D8 Advance from Bruker AXS operated at 40 kV and 30 mA equipped with LynxEye detector). The amorphous phase presents a broad diffraction peak in the XRD patterns around 2θ values ranging from 35 to 45 degrees.

The microstructure was observed by scanning electron microscope (SEM, Carl

Zeiss ULTRA55, Germany) combined with an energy dispersive X-ray spectroscopy (EDX). The SEM observations were conducted at an accelerating voltage of 15.0 kV and the samples were placed on conductive carbon tapes. Before SEM observation the samples were polished by mechanically (polish paper 400#-2000#) and mechano-chemically (polish solution, OP-S suspension).

The fine structure of the specimens was evaluated via transmission electron microscopy (TEM) using JEOL 2010 microscope. High-resolution transmission electron microscopy (HRTEM) imaging was also performed. The specimens for TEM were produced initially by mechanical polishing to 10 μm thickness and subsequently by the ion polishing technique to electron-beam transparency with liquid N_2 as a coolant.

2.3 Properties characterization

The compressive mechanical tests were performed in an INSTRON-5581 testing machine. The specimens (diameter to height ratio of 1:2) were subjected to compressive deformation at a strain rate of 1×10^{-4} s^{-1}. The mechanical tests were performed at room temperature, which is above the austenite transformation finish temperature A_f of about 275 K. The original crystalline phase was the austenite B2 phase. The cyclic mechanical loading-unloading tests were performed under the strain-controlled conditions by setting the same unloading stress in each loop.

Phase transformations were studied by differential scanning calorimetry (DSC; PerkinElmer DSC 8500) in Ar at a heating rate of 40 K/min (0.67 K/s) using the

second heating cycle from room temperature to crystallization temperature as the baseline for subtraction from the first cycle.

Dynamic mechanical analysis (DMA) was using to measure the loss and storage moduli of the ribbon samples to explore the nature of the cryogenic thermal cycling effect. The loss modulus shows a sharp maximum near the glass transition, and a small peak near the martensitic phase transformation temperature.

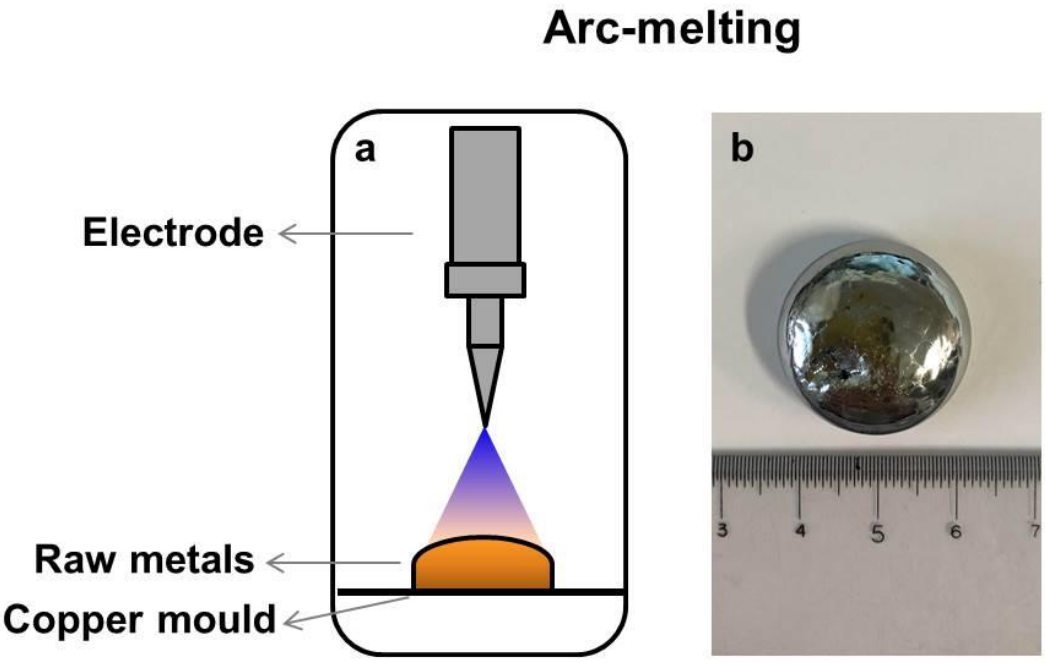

Fig. 2.1. The illustration of arc-melting (a) and the master alloy (b) prepared by arc-melting.

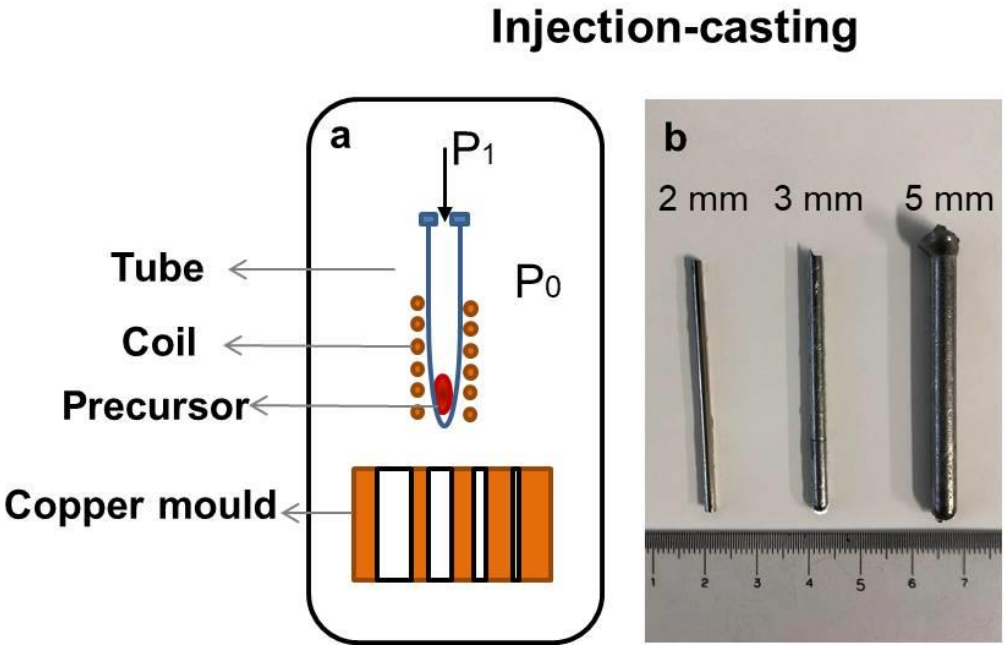

Fig. 2.2. The illustration of injection-casting (a) and rod samples with different diameters (b) prepared by injection-casting.

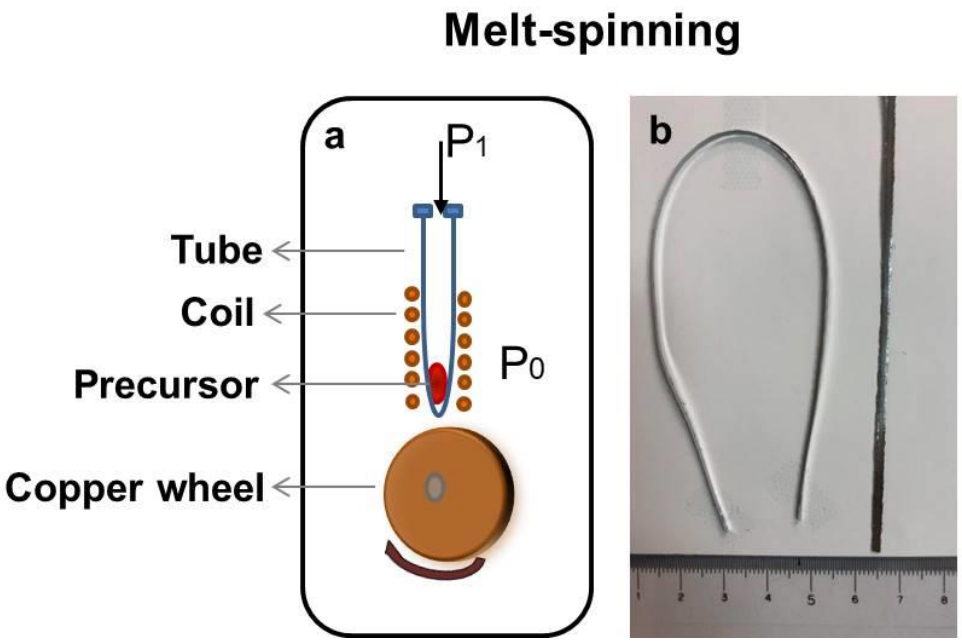

Fig. 2.3. The illustration of melt-spinning (a) and ribbon sample (b) prepared by melt-spinning.

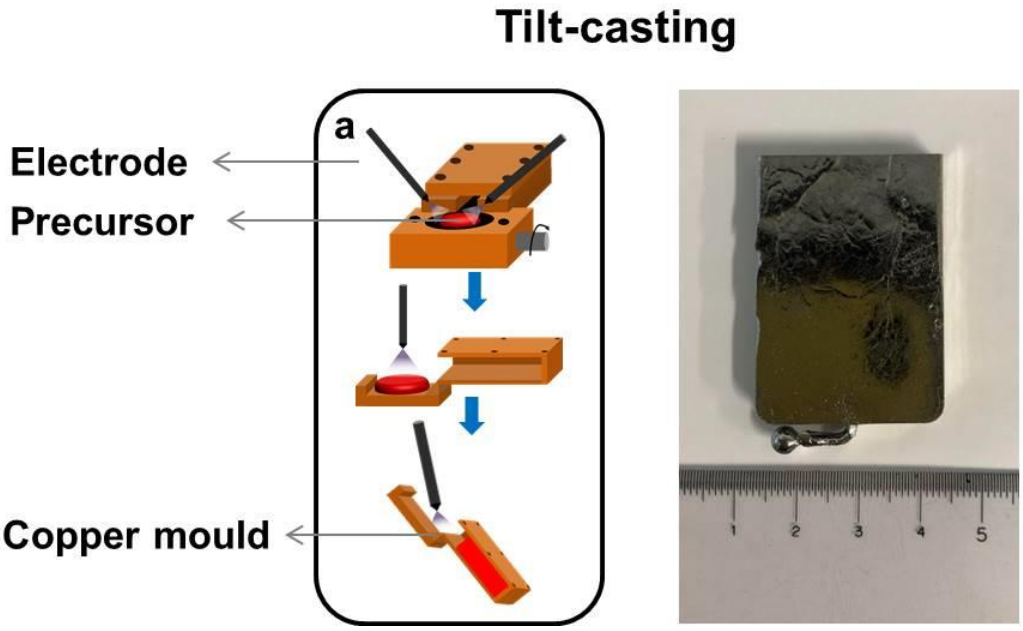

Fig. 2.4. The illustration of tilt-casting (a) and the plate shape sample (b) prepared by tilt-casting.

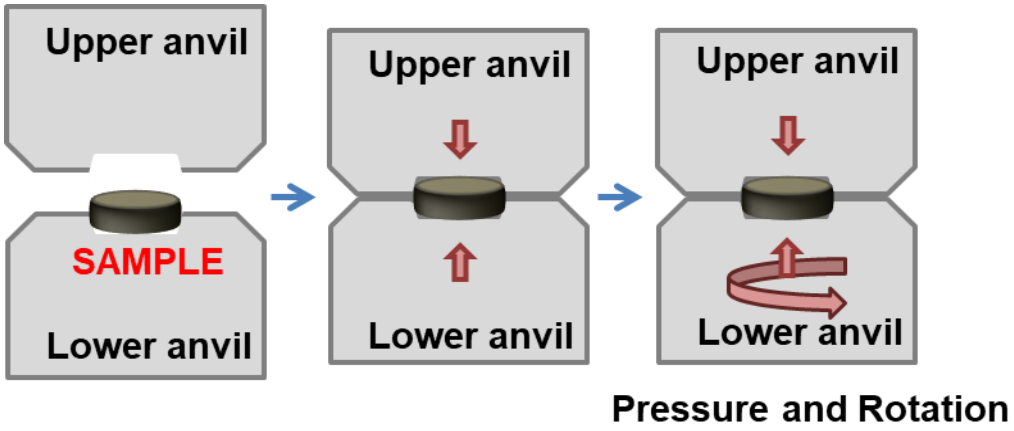

Fig. 2.5. Schematic illustration showing the principles of high pressure torsion (HPT) where a disk is subjected to a high applied pressure and concurrent torsional straining.

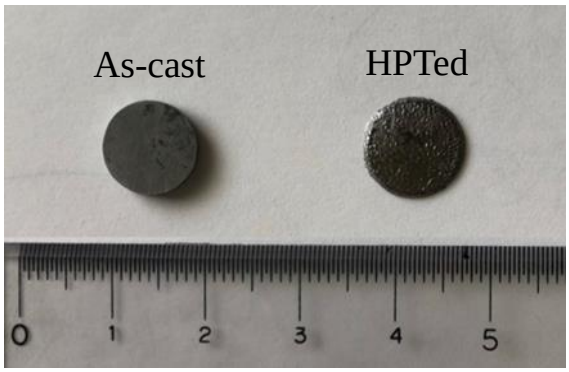

Fig. 2.6. The photos of as cast sample (left, 10 mm in diameter and 1.8 mm in thickness) and the sample with HPT treated (right, 1.2 mm in thickness).

Chapter 3

Effect of cooling rate and severe plastic deformation on the microstructure of TiNi-based crystalline/amorphous alloy

3.1 Introduction

Since being first reported in 1960 [1], amorphous alloys and bulk metallic glasses (BMGs), in particular, have received significant attention in the materials field, owing to their excellent combination of mechanical and functional properties [2-4]. These materials are considered promising for the structural engineering materials field. Ongoing research activities on BMGs range from investigations of the basic structure and properties to the structural and functional applications [5-7]. Various multicomponent (especially Zr-Cu-based, Ti-based, and Ni-based) alloys have been produced and extensively studied [8-11].

BMGs have unique mechanical properties including high strength combined with large elastic strain. However, due to the absence of long-range order atomic structue and, hence, dislocation slip systems. All macroscopic deformation is localized in so-called shear bands, which are extremely narrow. Therefore, most BMGs are macroscopically brittle and exhibit limited room-temperature ductility (mainly during compression) accompanied by limited fatigue resistance [12, 13]. Various approaches have been used to overcome these drawbacks. For example, a heterogeneous structure consisting of crystalline and amorphous phases was generated to improve the plasticity[14]. These in-situ and ex-situ glassy-crystal dual-phase materials, referred

to as bulk metallic glass composites (BMGCs), emerged at the end of the 20th century [7]. BMGCs are high-strength materials that exhibit better room-temperature plasticity than the homogeneous BMGs [15, 16]. In-situ BMGCs can be directly produced via casting or devitrification of a amorphous phase upon heating. Crystalline particles, which are formed by in-situ crystallization, act as barriers to shear band propagation. These particles also lead to shear band branching, which results in an increase in the overall plastic strain [17].

Some of these high-strength amorphous alloy composites exhibit the transformation induced plasticity (TRIP) effect and superelasticity, which are commonly observed in the Fe-, Ti- and Ni-based crystalline alloys [18]. During plastic deformation, the austenite phase transforms into martensite, which significantly enhances the ductility and toughness of the alloys [19]. This effect is associated with a composite effect resulting in stress redistribution and subsequent highly uniform plastic deformation [20]. Owing to superelasticity, a large load-induced strain can be imposed and then recovered during the unloading process. The occurrence of this phenomenon is attributed to the reversible phase transformation between martensite and austenite during deformation [21]. Several ductile TiNi-based glassy composites, which exhibit high strength and plasticity and contain B2-TiNi type crystalline phase precipitates in a glassy matrix have recently been prepared [22-27].

Here, we chose Y-, Co-containing Ti-Ni-Cu-Zr-based alloy ($Ti_{40}Ni_{39.5}Cu_8Zr_{10}Co_2Y_{0.5}$) that were considered in previous studies [24-27] as the main alloy for detail researches. The alloy exhibits excellent mechanical properties

and undergo a martensitic transformation during deformation. Cylindrical samples with different diameters were cast. The cooling rate has a significant impact on the formation of the amorphous phase. The main goal of this work is to determine the effect of cooling rate and volume fraction of the amorphous phase on the mechanical properties and deformation behavior of the studied alloys. The other method we use to control the phase composition is the high pressure torsion (HPT) which induces severe plastic deformation. The HPT process at 77 K induces a phase transformation between martensite and austenite, while HPT at room temperature keeps the main austenite phase.

3.2 Fabrication of TiNi-based crystalline/amorphous alloy exhibiting martensitic transformation during deformation

3.2.1 Morphology and element distribution

Scanning electron microscopy (SEM) was used to characterize the microstructure of as-cast TiNi crystalline-amorphous alloy. Fig. 3.1 shows the backscattered SEM images and the corresponding EDS mapping of different elements for the polished cross-section of the as cast $Ti_{40}Ni_{39.5}Cu_8Zr_{10}Co_2Y_{0.5}$ alloy. The clear light and dark contrast regions show the dual-phase structure. The dark area belongs to the B2-TiNi austenite crystalline phase and the bright area surrounding the crystalline phase is rich in the amorphous phase [20] A small amount of B19'-martensitic phase was also observed in XRD patterns (Fig.3.3d). The amorphous phase surrounding crystals acts as a boundary that obstructs the dislocation activity between grains during

deformation. The molar fraction of the elements Ti, Ni, Cu, Zr (Co and Y are hardly counted since the light weight) were obtained from the energy dispersive X-ray spectroscopy spectra in two regions, the dark area and the surrounding light area are listed in Table 3.1. Based on the experimental analysis, the dark area is enriched in Ti and Ni, the light area is enriched in Cu and Zr, which is also suggested as evidence that TiNi crystalline phase is surrounded by the amorphous phase.

Fig.3.2 shows the microstructures observed in TEM foils prepared from the as-cast $Ti_{40}Ni_{39.5}Cu_8Zr_{10}Co_2Y_{0.5}$ alloy. The HRTEM image clearly reveals the presence of amorphous and crystalline phases while the phase boundary is indicated by the red line. Selected area electron diffraction (SAED) patterns (insets in Figs.3.2b, c) show a diffuse halo, which is typical of the amorphous phase, and also indicates that the crystalline phases are the parent B2 phase (Fig. 3.2b) and the daughter B19' phase (Fig. 3.2c). According to the X-ray diffractometry in $Ti_{40}Ni_{39.5}Cu_8Zr_{10}Co_2Y_{0.5}$ alloy, this parent phase has a lattice parameter of 3.075 Å, which is larger than that (3.015 Å, as determined via XRD) of the equiatomic NiTi-B2 phase. The increase in the lattice parameter is attributed to the simultaneous introduction of Cu and Zr atoms, which are larger than Ni and Ti atoms, respectively.

The fracture surface of the $Ti_{40}Ni_{39.5}Cu_8Zr_{10}Co_2Y_{0.5}$ sample was also evaluated via SEM and XRD (see Fig. 3.3). Peaks corresponding to B2 austenite and B19' martensite occur in the XRD patterns of the as-cast sample and the fractured sample (Fig. 3.3d). However, the fraction of the martensite increases after fracture owing to the martensitic transformation occurring during deformation and fracture. In the case

of the fracture surface (Figs. 3.3a and 3b), the normal vector is inclined at~45 °to the loading axis corresponding to the maximum shear stress plane. The SEM image in Fig. 3.3a shows a few martensitic plates with sizes of ~400-800 nm. In addition, a vein pattern paired with a mirror-like flat region, typical of BMGs, occurs on the fracture surface (Fig. 3.3b). Bothe slip band lines and shear bands occur on the deformed lateral surface (see Fig. 3.3c).

3.2.2 Phase transformation

Unlike the serrated plastic flow typical for BMGs, the compressive stress-strain curves of the present alloys are smooth and serrations are absent. The sigmoidal shape (Fig. 3.4a) of the curves represents a common characteristic of crystalline TiNi alloys. These curves can be divided into three stages corresponding to (i) elastic deformation, at the beginning, the amorphous and crystal are elastically deformed. The curve exhibit a linear regimes of 0-0.2% in total strain, with the young's modulus E about 80±10 GPa; (ii) stress-induced martensitic transformation, after the period of elastic deformation, the transformation of martensite is triggered at a critical stress σ_m, and showing a plateau area in strain range from 0.2%-5%. During this process the initial B2 austenite phase transforms to B19' martensite phase and could be recovered by the reverse unloading process; (iii) plastic deformation, after the phase transform finishing the stress induced martensite experiences an elastic deformation in the strain range near 5%, a second yielding occurs at 1700 MPa- 2000 MPa. After the second yielding, the sample continues to deform plastically in the strain range from 7% to 20%. The martensitic phase forms via heterogeneous nucleation and is influenced by

the lattice strain [28]. This phase can induce two types of effects, i.e., superelastic and "TRIP", which yield a significant increase in the plasticity of dual-phase alloys [26, 29]. Song et al. obtained similar deformation curves for Cu-Ni-based composites, which they discussed as "triple yielding"[30].

The XRD analysis reveals the phase transformation process during the deformation of the TiNi crystalline/amorphous alloy. The corresponding XRD patterns with different loading stresses are shown in Fig. 3.4b. The sharp diffraction peaks correspond to the B2-type TiNi crystalline phase, attributed to the austenitic phase which transforms into the martensitic B19'-type TiNi phase during deformation. The XRD-patterns of the samples when loading was terminated at different stresses (σ), namely 650, 1700 and 2000 MPa on the corresponding loading-unloading curves (Fig. 3.4a), present the phase composition after the superelastic and plastic deformation regimes. The diffraction patterns of the as-cast sample and the sample which loading was stopped at point "a" (σ= 650 MPa, within the deformation-induced martensitic transformation process) show no big difference: both of them contain the peaks of austenitic phase (Fig. 3.4b). The martensitic phase peaks appear after loading up to near the second yielding point "b" (σ= 1700 MPa), between two yielding points after the beginning of the martensitic transformation. By contrast, the sample which loading was stopped at point "c" (σ= 2000 MPa, after the second yielding point that going plastic deformation) presents the XRD patterns similar to those of the fractured sample, all peaks are correspond to the martensite phase.

The martensitic transformation of TiNi alloys is not only induced by stress. More

commonly it is discussed as thermally induced phase transformation. Therefore the effect of superelasticity is strongly affected by the martensitic transformation temperature. A differential scanning calorimetry (DSC) trace of the TiNi crystalline/ amorphous alloy indicating thermal phase transformation is shown in Fig. 3.5. An endothermic peak of the austenitic transformation on heating and an exothermic peak of martensitic transformation on cooling are clearly observed. The austenitic transformation start temperature (A_s) is around 260 K and austenitic transformation finish temperature (A_f) is near 285 K. The mechanical tests and XRD measurements were performed at room temperature of 295 K where the crystalline phase is the austenitic B2 phase. Thus, the temperature induced phase transformation taking place below room temperature has no influence on the superelastic behavior related to the stress-induced martensitic transformation.

3.3 The effect of cooling rate on the volume fraction of amorphous /crystalline phases and the impact of the mechanical properties

3.3.1 The effect of cooling rate on the volume fraction of different phases

Fig. 3.6 shows the XRD spectrum of the $Ti_{40}Ni_{39.5}Cu_8Zr_{10}Co_2Y_{0.5}$ rod samples with different diameters. The XRD results indicate that the structures of the Ti-Ni-Cu-Zr based alloys contain an amorphous phase (as evidenced by a broad diffuse peak at 2θ of 37-45 °). The presence of this phase is confirmed by the HRTEM results (see Fig. 3.2), where the sharp diffraction peaks correspond to a B2-type crystalline phase. This B2-TiNi phase is the high-temperature austenitic phase, which

may transform to the low-temperature martensitic B19'-TiNi phase during deformation. The XRD patterns of samples in the as-cast state also contain peaks corresponding to the B19' phase. The crystalline phases act as obstacles to shear band propagation in the amorphous phase, induce ductility and strength enhancement during plastic deformation.

The XRD patterns in Fig. 3.6 were fitted by three Gaussian function peaks, obtained from the ribbon sample of $Ti_{40}Ni_{39.5}Cu_8Zr_{10}Co_2Y_{0.5}$ alloy which has fully amorphous phase. All the measurements were made by the same size scanning area as the ribbon sample to demonstrate the reliability of the fitting procedure. The volume fraction of the amorphous phase in the rod samples with different diameters is normalized by that of the ribbon sample containing 100 % of the amorphous phase, the result is displayed in Table. 3.2. The volume fraction of amorphous phase is dramatically decreasing from 25.7 % to 3.8 % with the diameter increase. It indicates that the cooling rate controls the formation of amorphous phase.

3.3.2 The impact of the mechanical properties by cooling rate

The stress-strain curves during compressive deformation of rod samples with different diameters are shown in Fig. 3.7. The values of critical stress (σ_m) inducing martensitic transformation as a function of the sample diameter are shown in Table. 3.3. The value of σ_m is decreasing with the rod diameter increasing. σ_m of the larger rod samples is lower than that of the smaller samples. The size of the sample is directly correlated with the cooling rate employed during the casting process, i.e., the cooling rate decreases with increasing diameter [24]. The lower cooling rate of the

larger samples (compared to that of the smaller samples) lead to precipitation of the crystalline phase and leads to a decrease in the volume fraction of the amorphous phase (the results are shown in Fig. 3.6). Therefore, compared to that formed in the smaller samples, a larger fraction of the high-temperature stable B2 phase can be formed from the metallic liquid in the larger samples. The presence of the abundant B2 phase induces martensitic transformation, which occurs easily at relatively low stresses. Higher cooling rate of the smaller samples induces a higher volume fraction of the amorphous phase. It is surrounding the crystalline one and restricts the dislocation movement during the martensitic transformation process. The confinement effects make the phase transformation difficult, hence, the critical stress (σ_m) is higher in the smaller samples.

The curves in Fig. 3.8 show the work-hardening rate of $Ti_{40}Ni_{39.5}Cu_8Zr_{10}Co_2Y_{0.5}$ alloy samples with different diameters. These curves, which are obtained from the calculated true stress (σ_{true}) and true strain (ε_{true}), also reflect three stages of deformation. After the elastic deformation (stage i), yielding induces the martensitic transformation, thereby resulting in a significant decrease (at ε values ranging from 0.2% to 2%) in the work-hardening rate. The martensitic transformation is a reversible shear deformation producing dislocations. The martensitic transformation is confined by the surrounding amorphous matrix which hampers generation of dislocations as well as shear band propagation. Therefore, the martensitic transformation (stage ii) finishes at lower strain (but at higher stress) in the 2-mm-diameter sample, which contains a larger fraction of the amorphous phase, than in the other samples. The

combination of elastic deformation and plastic deformation (stage iii) starts when the martensitic transformation is finished. The work-hardening rate increases after this transformation and shows maximum value during plastic deformation. Here we should note that the elastic deformation of the sample prevails over the plastic one at the beginning of stage iii. The initial increase at the end of stage ii is attributed to local dislocation movement in the austenitic grains and martensitic plates developed during martensitic transformation [31, 32]. Moreover, the strain hardening decreases with increasing volume fraction of the martensitic phase. Self-accommodation combined with twin formation influences the plastic transformation, leading to a gradual decrease in the work-hardening rate [33].

3.3.3 The universal effect on TiNi amorphous/crystalline alloys

To estimate the effect of the cooling rate on the volume fraction of the amorphous and crystalline phases, TiNi alloys with other compositions were fabricated because the Ti/Ni ratio influences the mechanical properties. Alloys with a nearly 1:1 Ti/Ni ratio (see Fig. 3.9) exhibit a slightly higher plasticity than those based on $Ti_{33}Ni_{40}$, where the compositional ratio is similar to that of the TiNi-B2 crystalline phase. The mechanical properties of two samples with the Ti/Ni content ratio of ~40 at% are shown in Fig.3.9 (alloy a and b), and the properties of samples with a $Ti_{33}Ni_{40}$ ratio are shown in Fig.3.9 (alloy c and d). The average values of the Young's modulus (E), stress that induces the martensitic transformation (σ_m), stress at the onset of plastic deformation (σ_r), ultimate stress (σ_b), and total strain (ε) for rod alloys with different diameters (d) are presented in Table 3.3. Here, the average values are obtained from at

least three sample tests, and the confidence interval (CI) is calculated (using the Student's standard test) as follows: CI = S × t/ n where S is the standard deviation, n is the number of tests, t is the value of the Student's t distribution, which depends on the probability (p = 95 %) and the degree of freedom (f = n-1). The critical stress (σ_m) in the four studied alloys shows the same tendency as in the base $Ti_{40}Ni_{39.5}Cu_8Zr_{10}Co_2Y_{0.5}$ one that is σ_m increasing with the sample size decreasing

3.4 Effect of the severe plastic deformation (SPD) on the phase transformation

3.4.1 The microstructure deformed by the high pressure torsion (HPT) process

High temperature stabilizes the austenite phase which could be transformed to low temperature martensite one by change in temperature or application of stresses. X-ray diffraction analysis (Fig. 3.10) reveals the phase transformation behavior of the TiNi crystalline/amorphous alloy by HPT process. After HPT at different temperature, the alloy structure contains B19' martensitic phase or combines B2 and B19' phase. It can be understood that during HPT at 77 K the B2 phase transformed to B19' martensitic one from austenite by the thermal effects and the temperature-induced martensite was processed by the HPT at severe stain. That martensite cannot recover to austenite even when the temperature rose up. After HPT at room temperature the alloy contains mainly B2 austenitic phase, which means that the martensitic phase induced by the stress during the HPT can recover to austenite when the stress is released. The intensity of diffraction peaks of B2 phase gradually decreases at both

two conditions of HPT, leading to an extremely broad peak, nearly 10 degrees of 2θ from 35 to 45 degrees. The peak of as cast sample is relatively narrow and sharp, as discussed in previous work, it includes three phases in the as cast samples. The main phase is B2 austenite phase, plus small amount of B19' austenite phase and the amorphous phase. The broadening of the peak in XRD patterns is induced by the severe plastic strain that refines the crystal size and raises the inner lattice strain. The grain size refinement is a typical effect of HPT and more of the amorphous phase may be formed.

Fig. 3.11 shows the SEM backscattering electron (BSE) micrographs of the specimen processed by HPT at different temperature together with that of the as cast crystalline/amorphous alloy. The micrographs were taken from the polished cross-section surface. The amorphous and crystalline phases look different in the BSE images as discussed before. Namely, the amorphous phase is located in the bright area surrounding the dark crystalline phase area. The microstructure is refined greatly at both HPT processes, the round shape dendrite like structure was destroyed to form a structure with narrow strips. The dark area crystalline phase becomes narrow and tiny. The light area is distributed widely and uniformly in both sample processed by HPT at room temperature and liquid nitrogen temperature.

3.4.2 The mechanical properties effect by the high pressure torsion (HPT) process

Vickers microhardness of TiNi based crystalline/amorphous alloys before and after HPT process in different conditions are plotted as a function of distance from the edge to the center of the disk. The HV values were tested on smooth and clean

polished surfaces of the samples. The data were recorded on each disk using an FM microhardness tester equipped under loading of 300 gf and a dwell time of 15s for each measurement. These measurement were taken at varies positions across a diameter of disk with three points recorded around each selected position. As shown in Fig. 3.12 the plots of microhardness of the specimens in three stages have no substantial differences with the location from edge to the center. The hardness of HPT process samples at both room temperature and at 77 K is around HV 450 which is higher than that in the as cast alloy of HV 300. The increase of the microhardness is attributed to an increase in dislocation density during the HPT process which induced severe plastic deformation.

The TEM images with selected area electron diffraction (SAED) patterns obtained from sample after HPT process at different conditions. HPT at 77 K and HPT at room temperature (r.t.) are shown in Fig. 3.13 and Fig. 3.14, respectively. With HPT at both conditions the microstructures are homogeneous compared with the as cast state (see Fig. 3.2). The SAED patterns correspond to the XRD results, which are B19’ martensite phase at 77 K (inset of Fig. 3.13a) and B2 austenite phase at r.t. (inset of Fig. 3.14a), respectively. Thus, the employed HPT technique enabled to obtain the dual martensite-amorphous phase and austenite-amorphous phase alloys. Fig. 3.13a exhibits the martensite plate structure and in Fig.3.14a the microstructure of austenite phase also of layered microstructure. The SAED patterns of both phases include a halo which indicates the present of amorphous phase. The high resolution images (Fig. 3.13b and 3.14b) demonstrate the mix of amorphous phase and

nano-crystalline phase. The homogeneous mixture of crystalline and amorphous phases after HPT treatment is benefit for improving the microhardeness. The corresponding bright field (Fig. 3.13c and 3.14c) and dark field (Fig. 3.13d and 3.14d) graphics reveals the layer structure are constituted by layer of crystalline phase and layer of mixed amorphous and crystalline phase.

3.5 Conclusion

Ti-Ni based crystalline/amorphous alloys with a homogeneous dual-phase structure consisting of an amorphous phase and two crystalline phases, high temperature stable B2 austenite and low temperature stable B19' martensite. The phase transformation between martensite and austenite could be induced by both thermal and stress. The TiNi crystalline/amorphous composite alloys exhibit a good combination of strength and ductility. The specimens were deformed to a fairly large strain of 20% and tolerated a high stress of 2300 MPa prior to fracture. The compressive deformation stress-strain curves had a double sigmoidal shape with three deformation stages, elastic deformation process, a plateau state corresponding to the martensitic transformation process and final plastic deformation process. The extraordinary mechanical properties can be attributed to the interplay between dislocation slip and shear deformation of the dual-phase material, in conjunction with the "superelastic" behavior operating during martensitic transformation. The occurrence of both amorphous and crystalline phases in the microstructure was confirmed by XRD, SEM, and TEM. The microstructure reveals a main austenite

phase surrounding by the amorphous phase and a small amount of martensite phase which normally appears together with the martensite phase.

The mechanical properties are influenced by the cooling rate (which induces the difference in crystalline phases and affects the fraction of amorphous phase) employed during casting. Compared with the larger rods formed at lower cooling rates, the smaller rods formed at higher cooling rates contain a larger fraction of amorphous phase and require a higher stress for martensitic transformation. The present of amorphous phase surrounding the crystalline phase confines the phase transformation between austenite and martensite. Thus, the smaller sample which including more amorphous phase shows a higher critical phase transformation stress during the deformation.

We preformed the High Pressure Torsion (HPT) process at different temperature, 77 K and room temperature, to control the phase composition. The austenite main phase in TiNi crystalline/amorphous as cast state transform to the martensite phase after HPT at 77 K process. Comparably, the room temperature HPT process induces the main phase is still austenite phase. The XRD patterns of the disks with HPT process at two conditions show broaden peaks which indicate the grain size dramatically refinement or amorphous phase increase by the severe plastic deformation. The TEM images reveal a homogenerous mixture of amorphous phase and nano size crystalline phase in the samples after HPT process at both conditions. Thus, the employed HPT technique enabled to obtain the dual martensite-amorphous phase and austenite-amorphous phase alloys. The homogeneous mixture of crystalline

and amorphous phases after HPT treatment at 77K and room temperature both improve the microhardeness.

References

1. W.K. Jun, R. Willens, and P. Duwez, Nature, 1960. 187(4740): p. 869.

2. C. Suryanarayana and A. Inoue, Bulk metallic glasses. 2017: CRC press.

3. A. Inoue, Acta materialia, 2000. 48(1): p. 279-306.

4. A.Inoue, B. Shen, and A. Takeuchi, Materials Science and Engineering: A, 2006. 441(1-2): p. 18-25.

5. Y.H. Liu, G. Wang, R.J. Wang, M.X. Pan, W. H. Wang, science, 2007. 315(5817): p. 1385-1388.

6. D.V. Louzguine-Luzgin, and A. Inoue, Bulk Metallic Glasses: Formation, Structure, Properties, and Applications, in Handbook of magnetic materials. 2013, Elsevier. p. 131-171.

7. J. Qiao, H. Jia, and P.K. Liaw, Materials Science and Engineering: R: Reports, 2016. 100: p. 1-69.

8. T. Zhang, A. Inoue, and T. Masumoto, Materials Transactions, JIM, 1991. 32(11): p. 1005-1010.

9. D.C. Hofmann, J.Y. Suh, A. Wiest, G. Duan, M.L. Lind, Nature, 2008. 451(7182): p. 1085.

10. J. Eckert, J. Das, S. Pauly, C. Duhamel, Journal of materials research, 2007. 22(2): p. 285-301.

11. S. Pauly, G. Liu, G. Wang, U. Kühn, N. Mattern, J. Eckert, Acta Materialia, 2009. 57(18): p. 5445-5453.

12. A.L. Greer, Science, 1995. 267(5206): p. 1947-1953.

13. W.L. Johnson, MRS bulletin, 1999. 24(10): p. 42-56.

14. A.L. Greer, Materials Today, 2009. 12(1-2): p. 14-22.

15. A. Inoue, T. Zhang, M.W. Chen, T. Sakurai, Applied Physics Letters, 2000. 76(8): p. 967-969.

16. V.Y. Zadorozhnyy, A. Inoue, and D. Louzguine-Luzgin, Materials Science and Engineering: A, 2012. 558: p. 472-477.

17. D.V. Louzguine, H. Kato, and A. Inoue, Applied physics letters, 2004. 84(7): p. 1088-1089.

18. F. Gil, and J. Planell, Journal of Biomedical Materials Research, 1999. 48(5): p. 682-688.

19. K. Otsuka, and X. Ren, Progress in materials science, 2005. 50(5): p. 511-678.

20. K.A. GschneidnerJr., MinJi, C.Z. Wang, K.M. Ho, A.M. Russell, Ya. Mudryk, A.T. Becker, J.L. Larson, Acta materialia, 2009. 57(19): p. 5876-5881.

21. T. Grosdidier, and M.-J. Philippe, Materials Science and Engineering: A, 2000. 291(1-2): p. 218-223.

22. A. Yu. Churyumov, A.I. Bazlov, A.N. Solonin, V.Yu. Zadorozhnyi, G.Q. Xie, S. Li, D.V. Louzguine-Luzgin, The Physics of Metals and Metallography, 2013. 114(9): p. 773-778.

23. N. Hatcher, O.Y. Kontsevoi, and A. Freeman, Physical Review B, 2009. 79(2): p. 020202.

24. D.V. Louzguine-Luzgin, T. Saito, J. Saida. A. Inoue, Journal of Materials Research, 2008. 23(8): p. 2283-2287.

25. A.A. Tsarkov, A.Y. Churyumov, V.Y. Zadorozhnyy, D.V. Louzguine-Luzgin, Journal of Alloys and Compounds, 2016. 658: p. 402-407.
26. D.V. Louzguine-Luzgin, A. Vinogradov, G. Xie, Philosophical Magazine, 2009. 89(32): p. 2887-2901.
27. I.S. Golovin, V.Y. Zadorozhnyy, A.Y. Churyumov, D.V. Louzguine-Luzgin, Journal of Alloys and Compounds, 2013. 579: p. 633-637.
28. A. Ibarra, D. Caillard, J. San Juan, M.L. No, Applied Physics Letters, 2007. 90(10): p. 101907.
29. S. Pauly, J. Das, J. Bednarcik, N. Mattern, K.B. Kim, J.Eckert, Scripta Materialia, 2009. 60(6): p. 431-434.
30. K.K. Song, S. Pauly, Y. Zhang, R. Li, S. Gorantla, N.Narayanan, U.Kühn, T.Gemming, J.Eckert, Acta Materialia, 2012. 60(17): p. 6000-6012.
31. T. Ezaz, H. Sehitoglu, and H. Maier, Acta Materialia, 2011. 59(15): p. 5893-5904.
32. K. Gall, H. Sehitoglu, Y. I. Chumlyakov, I. V. Kireeva and H. J. Maier, Journal of engineering materials and technology, 1999. 121(1): p. 28-37.
33. C.M. Wayman,and K. Otsuka, Shape memory materials. 1998: Cambridge University Press.

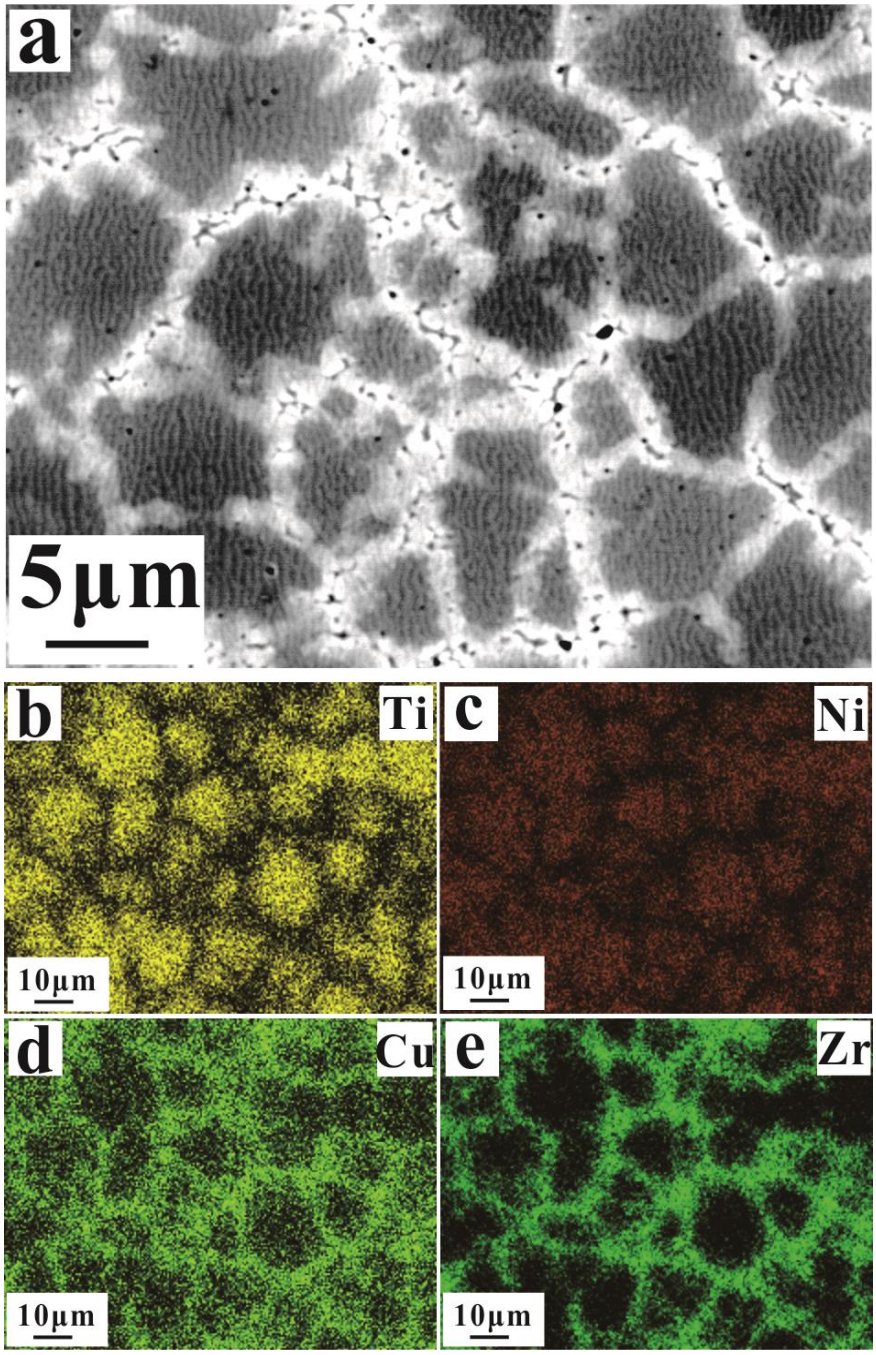

Fig. 3.1. the backscattered scanning electron microscope (SEM) images and the corresponding EDS mapping of different elements for the polished as cast $Ti_{40}Ni_{39.5}Cu_8Zr_{10}Co_2Y_{0.5}$ alloy

Table 3.1. The molar/aromic fraction of the elements in $Ti_{40}Ni_{39.5}Cu_8Zr_{10}Co_2Y_{0.5}$ alloy

at.%	Ti	Ni	Cu	Zr	Co	Y
Dark area	38.5	40.8	8.8	9.5	2.5	
Light area	33.7	38.6	10.9	15.1	1.6	0.2

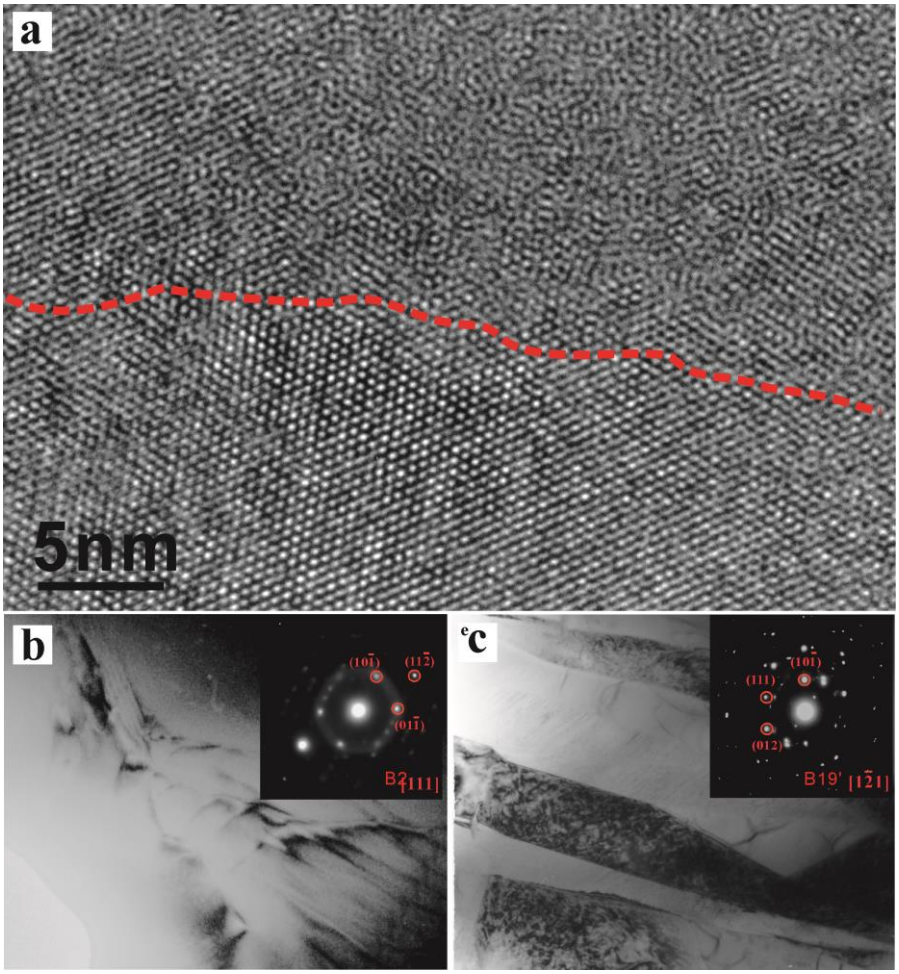

Fig. 3.2. (a) HRTEM image of the as-cast Ti40Ni39.5Cu8Zr10Co2Y0.5 alloy showing the interface of the crystalline and amorphous phases, (b) SAED patterns with cP2 crystalline diffraction spot, and (c) mP4 crystalline diffraction spot. The halo pattern of the amorphous phase and the corresponding bright-field images occur in the SAED patterns.

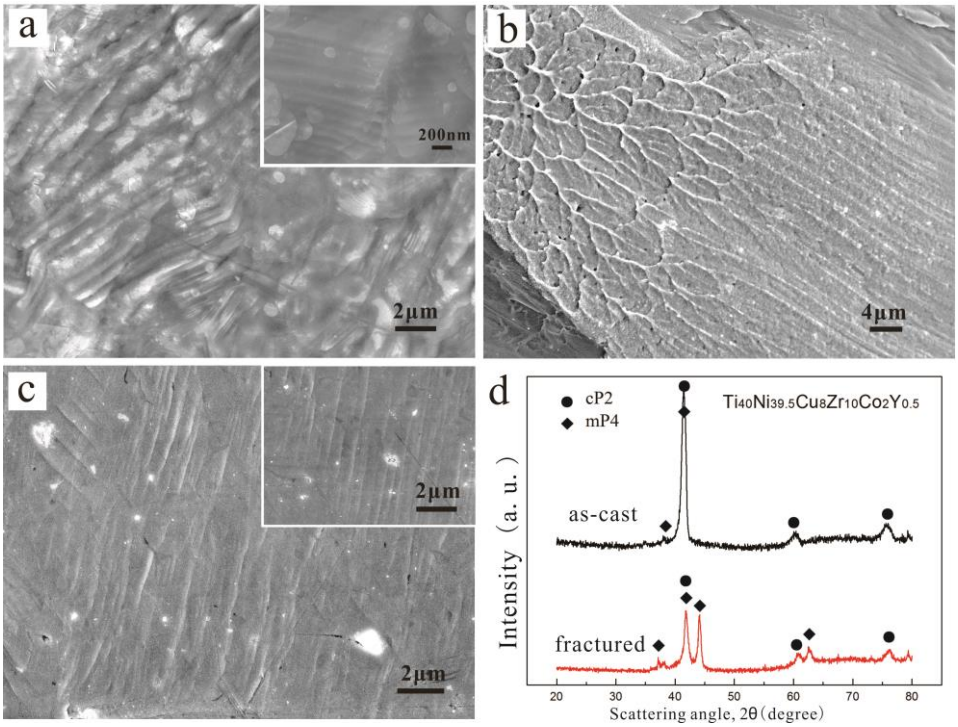

Fig. 3.3. (a, b) SEM images showing the fracture surface of the Ti40Ni39.5Cu8Zr10Co2Y0.5 alloy with the basic structure of martensite and vein-type patterns of the amorphous phase, (c) structure of the lateral surface, and (d) XRD patterns of the as-cast and the fractured samples.

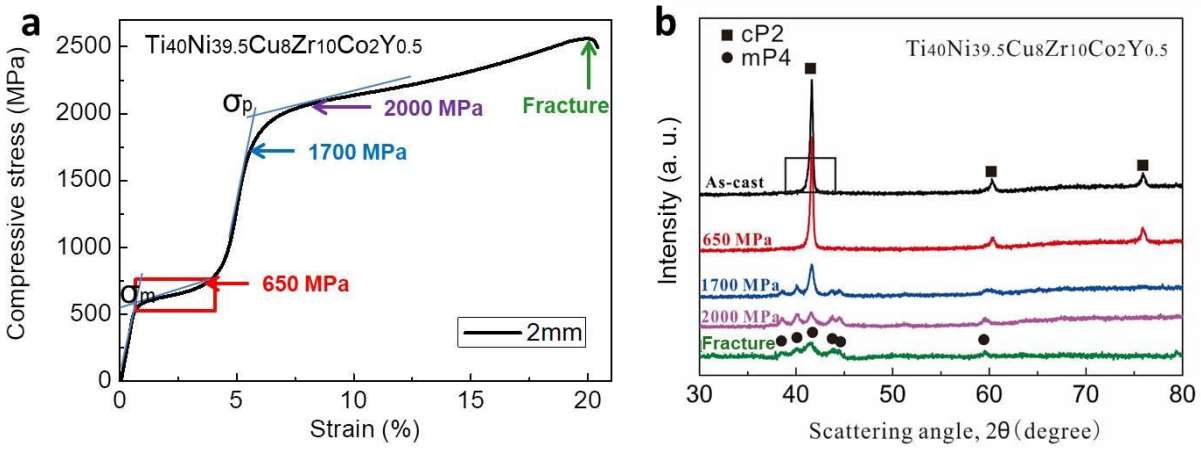

Fig. 3.4. The compressive stress-strain curve of TiNi crystalline/amorphous alloy (a), and the corresponding XRD patterns (b) of as cast sample with different loading stresses.

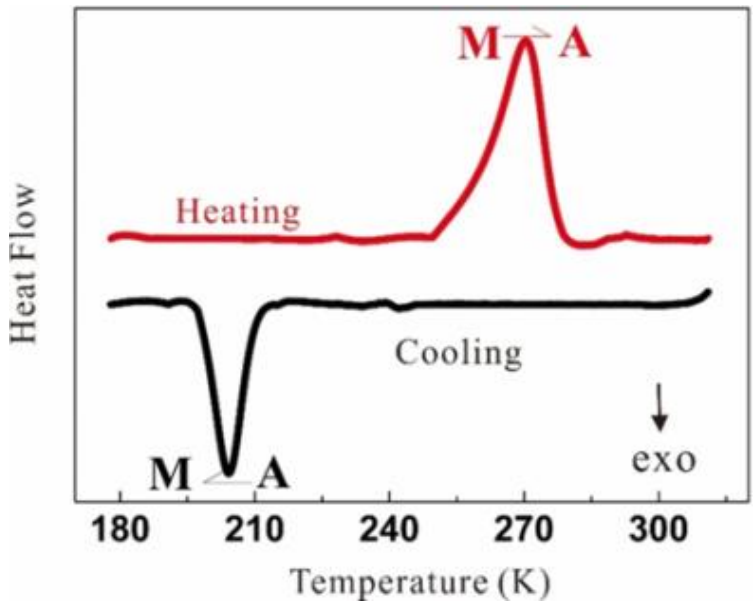

Fig. 3.5 The DSC heating and cooling traces of TiNi crystalline/amorphous alloy showing the martensitic and austenitic transformation

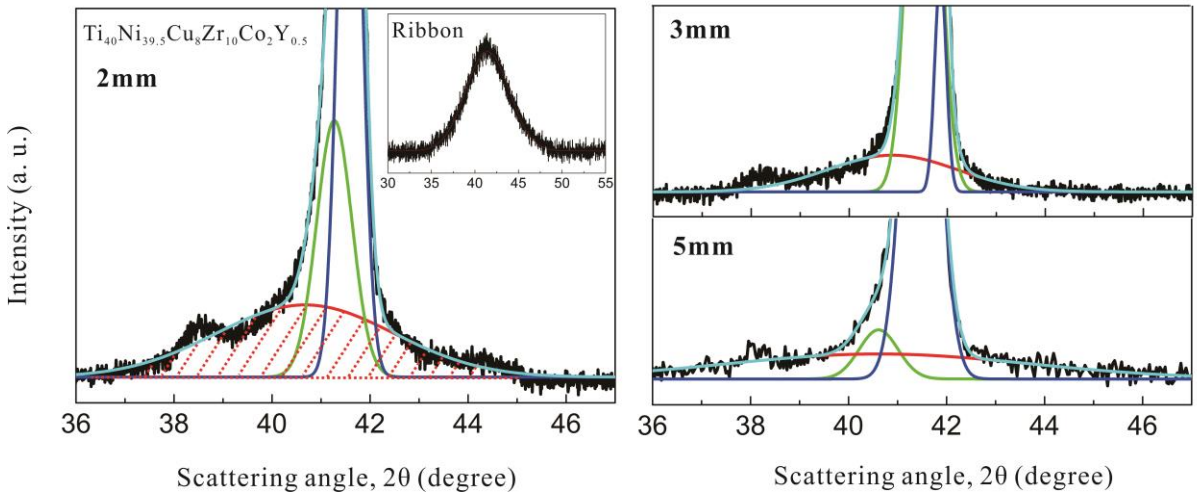

Fig. 3.6. XRD patterns (fitted by Gauss equation) of the as-cast TiNi crystalline/amorphous samples with different diameters

Table.3.2. the volume fraction of the amorphous phase in rod samples as a function of diameter (d).

Diameter (d)	**2 mm**	**3 mm**	**5 mm**
A_{vol} (%)	**25.7 ±6.4 %**	**9.7 ±3.5 %**	**3.8 ±2.4 %**

***** **A_{vol}** is the volume fraction of amorphous phase in crystalline/amorphous alloy calculated by fitting XRD patterns.

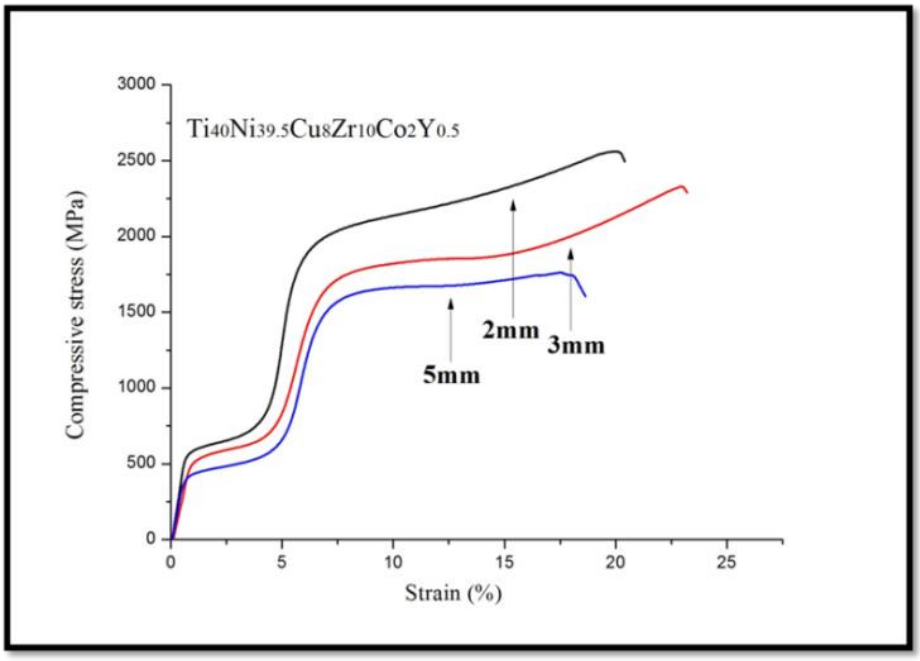

Fig.3.7. The compressive stress-strain curves of the as-cast $Ti_{40}Ni_{39.5}Cu_8Zr_{10}Co_2Y_{0.5}$ rod samples with different diameters showing a plateau area of martensitic phase transformation

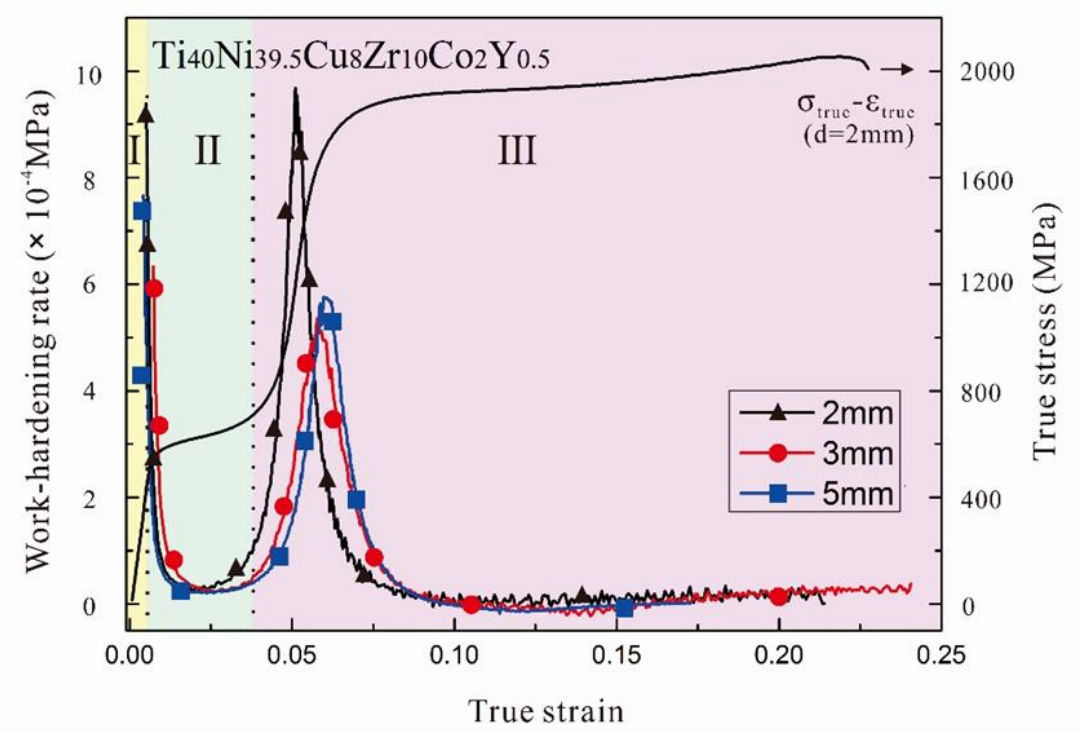

Fig.3.8. Curves showing the work-hardening rate of the $Ti_{40}Ni_{39.5}Cu_8Zr_{10}Co_2Y_{0.5}$ alloys with different diameters. The true stress-strain curve of the 2-mm-diameter sample is shown as a guide for three stages.

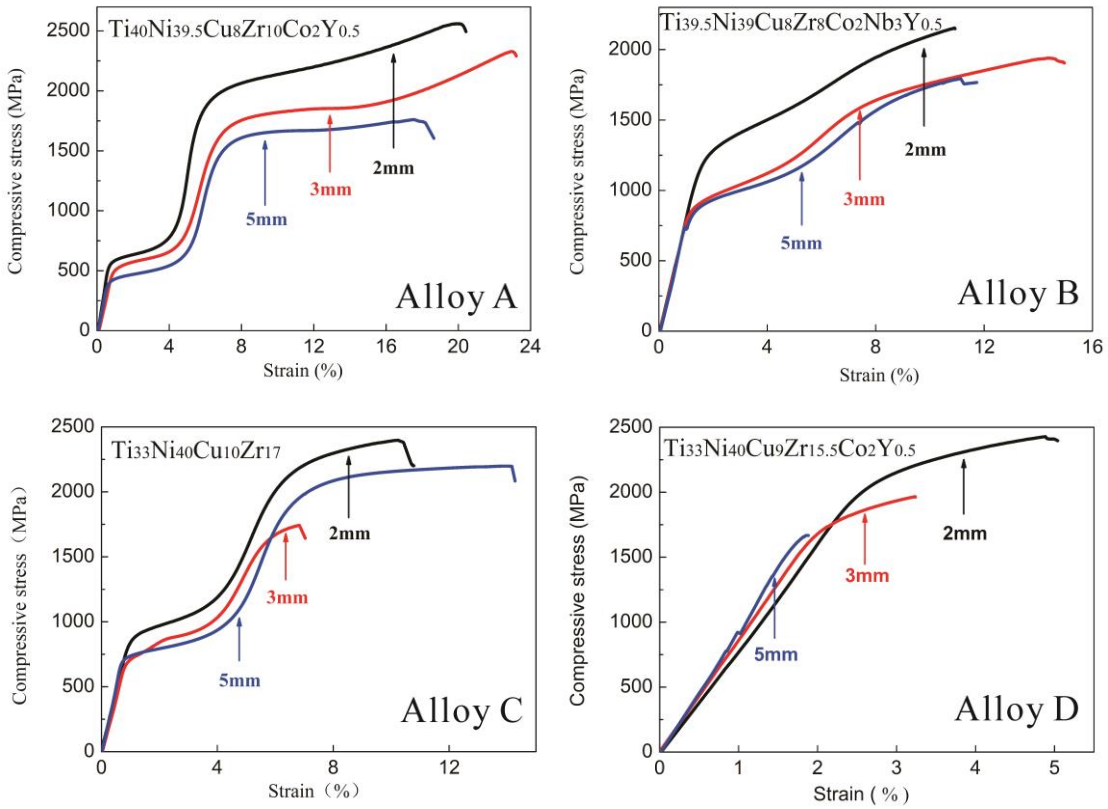

Fig.3.9. The compressive stress-strain curves of the as-cast rod samples with different diameters. For the alloy A: $Ti_{40}Ni_{39.5}Cu_8Zr_{10}Co_2Y_{0.5}$ and alloy B: $Ti_{39.5}Ni_{39}Cu_8Zr_8Co_2Nb_3Y_{0.5}$ (the Ti/Ni ratio of this group is nearly 1:1).Results of the alloy C: $Ti_{33}Ni_{40}Cu_{10}Zr_{17}$ and alloy D: $Ti_{33}Ni_{40}Cu_9Zr_{15.5}Co_2Y_{0.5}$

Table 3.3 Mechanical properties of the studied alloys as a function of the sample diameter (d).

Composition	d (mm)	E (GPa)	σ_m (MPa)	σ_r (MPa)	σ_b (MPa)	ε (%)
$Ti_{40}Ni_{39.5}Cu_8Zr_{10}Co_2Y_{0.5}$	2	86 ±11	552 ±31	1948 ±90	2390 ±210	18.7 ±2.2
	3	68 ±8	505 ±28	1693 ±78	2295 ±210	22.2 ±2.8
	5	77 ±8	408 ±20	1601 ±75	1761 ±170	17.6 ±2.1
$Ti_{39.5}Ni_{39}Cu_8Zr_8Co_2Nb_3Y_{0.5}$	2	97 ±14	1262 ±60	1920 ±89	2143 ±210	11.2 ±1.3
	3	81 ±9	881 ±48	1582 ±70	1925 ±200	14.5 ±1.5
	5	90 ±12	849 ±42	1542 ±68	1798 ±180	11.2 ±1.3
$Ti_{33}Ni_{40}Cu_{10}Zr_{17}$	2	91 ±13	875 ±43	2161 ±93	2412 ±220	10.3 ±1.1
	3	84 ±11	727 ±38	1615 ±76	1737 ±180	6.8 ±0.5
	5	95 ±12	727 ±37	2068 ±91	2194 ±210	14.5 ±1.5
$Ti_{33}Ni_{40}Cu_9Zr_{15.5}Co_2Y_{0.5}$	2	81 ±11			2310 ±220	4.9 ±0.5
	3	87 ±13			1970 ±180	3.2 ±0.3
	5	93 ±14			1663 ±160	1.9 ±0.2

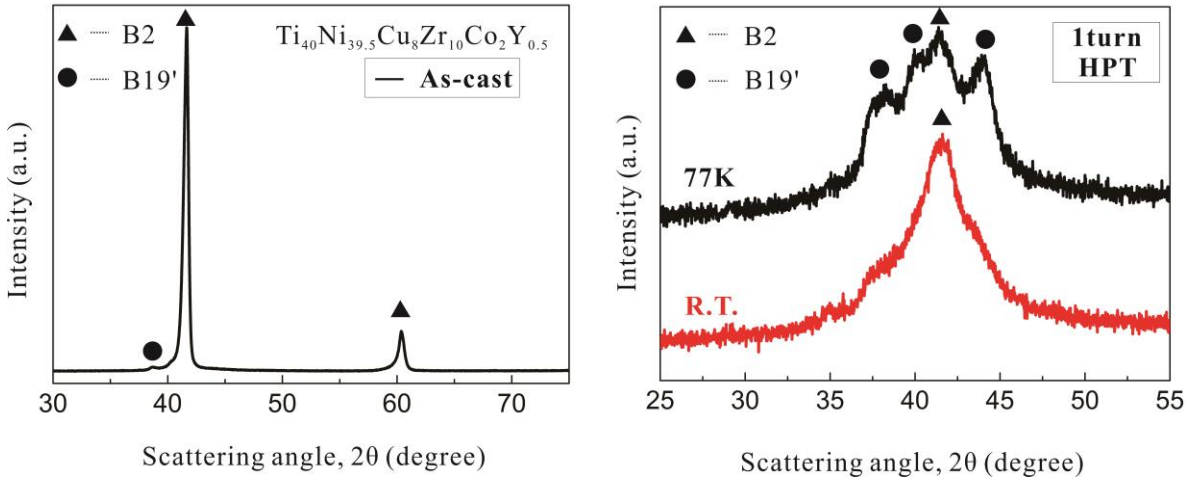

Fig. 3.10. The XRD patterns of the surface of as cast sample (a),and the samples after HPT performing in two conditions, 77K and room temperature.

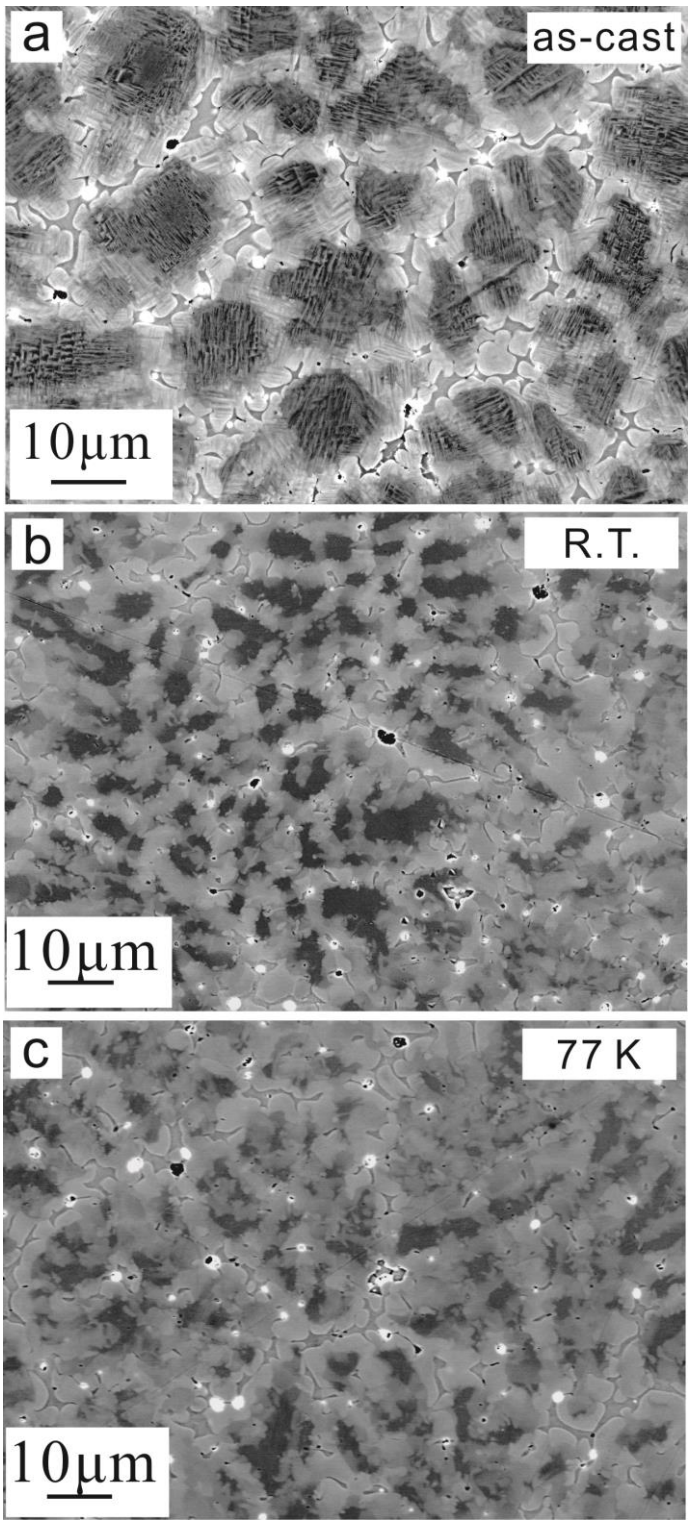

Fig. 3.11. The SEM-BSE images of the as cast TiNi crystalline/amorphous sample and specimens processed by HPT at different temperature as indicated.

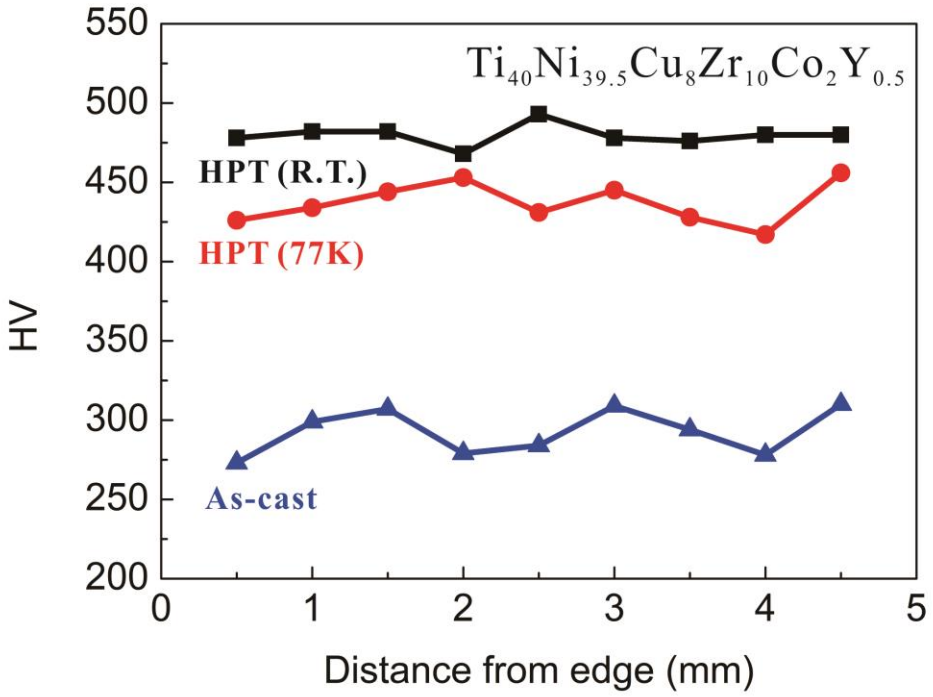

Fig. 3.12. Vickers microhardness of the TiNi crystalline/amorphous alloy from the disk center to edge after HPT at room temperature and 77k comparing as cast state

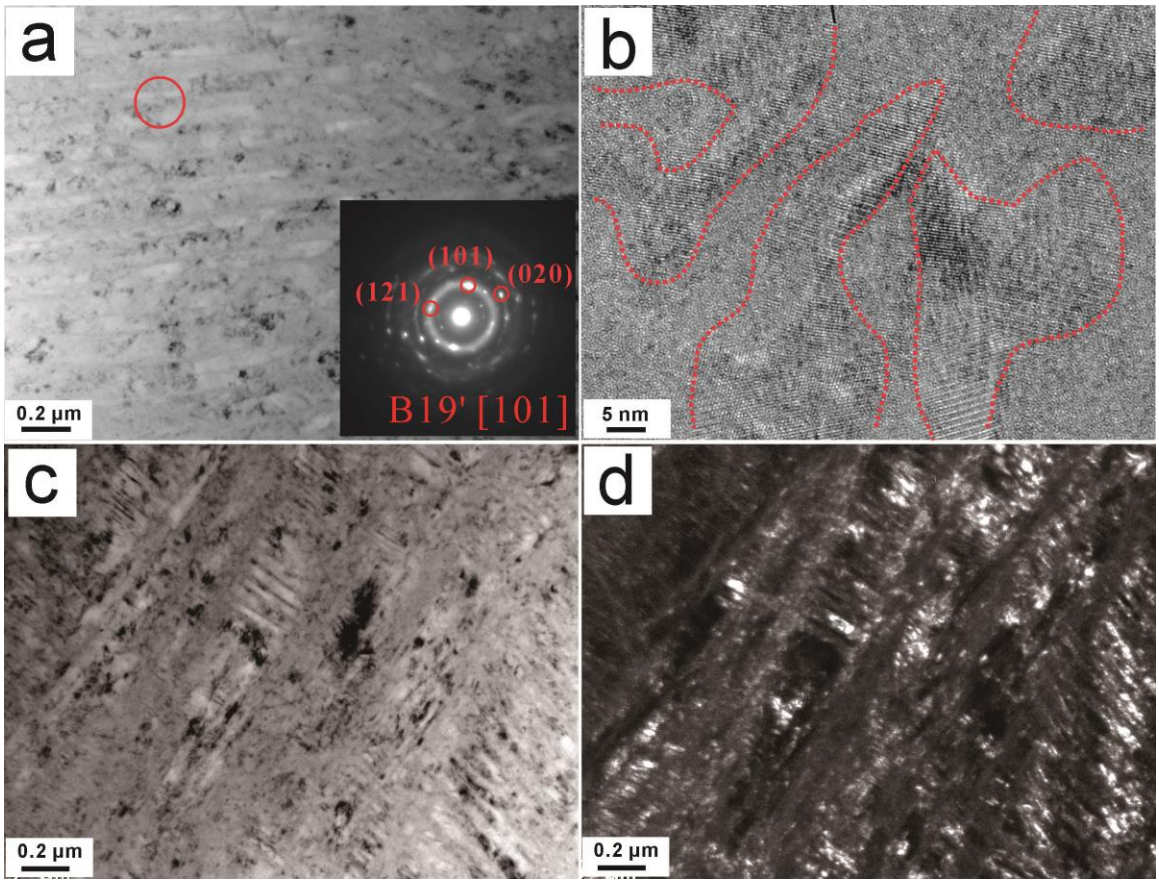

Fig. 3.13. (a) The TEM images of the TiNi crystalline/amorphous specimen after HPT process at 77K. The SAED patterns show in inset; the corresponding high-resolution images (b) and bright field (c) dark field (d) images, respectively.

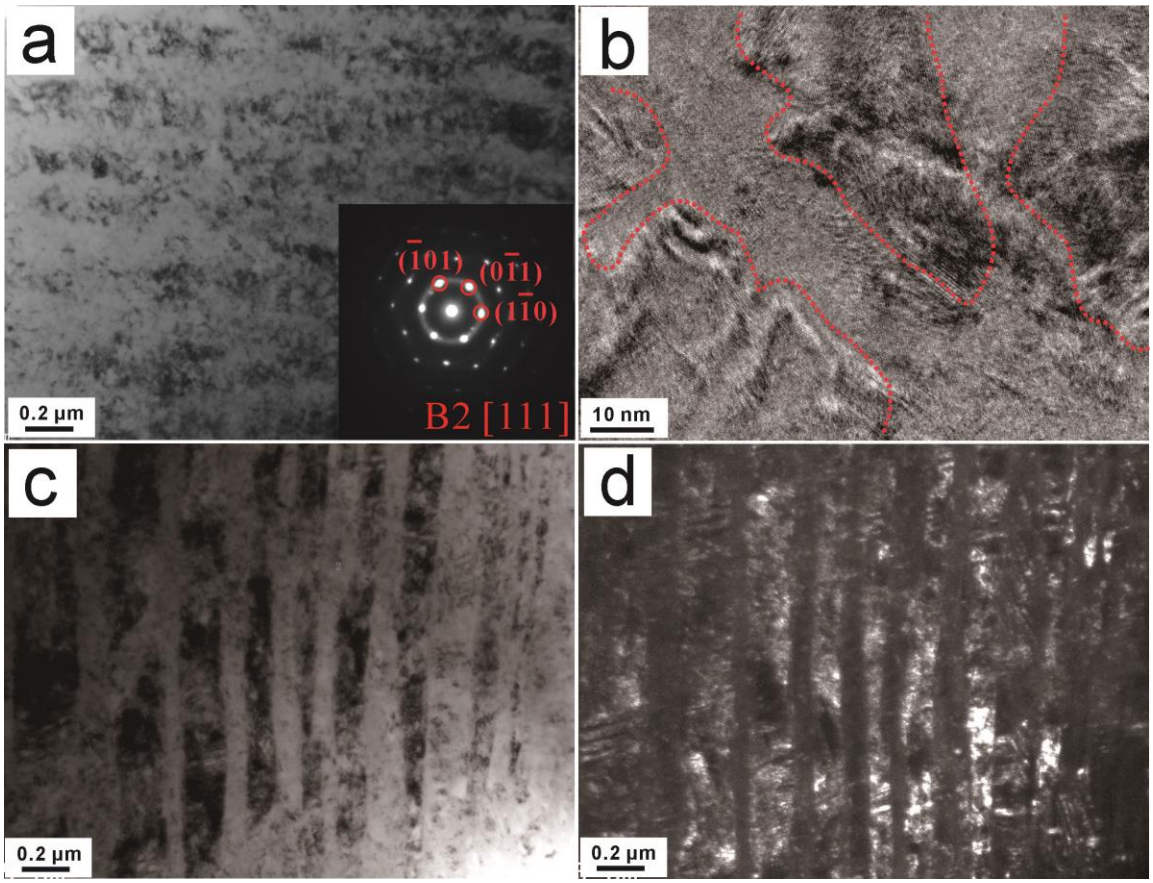

Fig. 3.14. (a)The TEM images of the TiNi crystalline/amorphous specimen after HPT process at room temperature. The SAED patterns show in inset; the corresponding high-resolution images (b) and bright field (c) dark field (d) images, respectively.

Chapter 4

Influence of the amorphous phase on mechanical cycling behavior

4.1 Introduction

Bulk metallic glasses (BMGs) have unique and diverse mechanical, chemical and physical properties which are used in various areas [1]. These intriguing properties originate from their atomically disordered structure. Therefore, investigations of BMGs structure and properties are important for future structural and functional applications [2, 3]. However, owing to inherently absent long-range ordered structure in amorphous phase all macroscopic deformation is situated in the highly localized shear bands and promote structural collapse via a shear-band-to-crack transition [4, 5]. Thus most of BMGs exhibit macroscopically brittle show limited ductility and fatigue resistance at room temperature[6]. One way to overcome these drawbacks is to generate a composite structure consisting of crystalline and amorphous phases [7]. Crystalline-amorphous dual phase materials are referred to as bulk metallic glass composites (BMGCs) exhibiting both high strength and room temperature plasticity attracted significant attention [8, 9]. Crystalline phase in BMGCs acts as barriers to shear band propagation and prevent the dominant shear band formation, which leads to the shear bands branching and, hence, increase in plastic strain [10].

Superelasticity effect is induced by the solid to solid phase transformation from austenite to martensite on loading which is accompanied by a strain accumulation.

The reverse martensitic transformation during unloading induces the strain recovery. It is one of the most notable behaviors in the Ti-, Fe- and Ni-based crystalline shape memory alloys [11, 12]. In the process of deformation, imposed load induces a transformation of an austenite phase into a martensite phase that could recover during unloading. The superelastic shape memory alloys exhibit a stress plateau which causes large elastic strain. They also show hysteretic damping and excellent cyclic fatigue properties that make them desirable for applications in seismic resistant design [13]. Some ductile TiNi-based BMGCs, containing TiNi B2-type crystalline phase precipitates in an amorphous matrix, also show superelastic behavior. The TiNi-based BMGCs exhibit high strength and plasticity which are attributed to the reversible phase transformation between martensite and austenite [7].

The superelastic effect under cyclic loading is a generic characteristic feature of the TiNi shape memory alloys [14, 15]. Mechanical-fatigue on cyclic loading is an important feature which affects the residual strain after unloading, the critical stress for the martensitic transformation and the hysteresis or the amount of energy dissipated. The characteristic of fatigue properties during superelastic cycling is that the residual strain grows with the number of cycles, while both the stress for inducing martensitic transformation and the stress hysteresis decrease [16]. At the same time it changes the shape of the stress-strain curve, shrinks the plateau area, which means that the energy dissipated in one cycle decreases. There is a need to know how microstructural damage accumulates during cyclic loading and eventually affects the fatigue resistance. The mechanical-fatigue is frequently ascribed to the rise of internal

stresses in the material upon the superelastic cycling which is caused by the accumulation of dislocations and the dislocation strain fields [17, 18]. Slip dislocations created by propagating austenite and martensite interfaces were experimentally observed in the superelastically deformed TiNi alloy by transmission electron microscopy (TEM) [19]. The amorphous phase in BMGCs influences the dislocation slip process during loading and reduces the accumulation of irreversible strain and decelerates a decrease in martensite transformation inducing stress.

In the present work, we designed Ti-Ni BMGCs with amorphous and crystalline composite phases and studied the martensitic transformation behavior, the superelastic effect and the mechanical properties during cyclic loading-unloading deformation. $Ti_{49.5}Ni_{50.5}$ (at. %) was prepared as TiNi fully crystalline alloy to compare the low times mechanical-fatigue behavior with the TiNi crystalline/amorphous alloy. The different response characteristics of two compared materials reveal the role of amorphous phase during the cyclic deformation and present a way to evaluate the role of amorphous phase for cyclic loading-unloading behavior.

4.2 The recovering behavior for different deformation stages

The phase transformation between martensite and austenite in the TiNi alloys induces the effect of “superelasticity” that influences yield strength and significantly improves the plasticity. Therefore, the designed TiNi BMGC has a good combination of strength (2500 MPa) and ductility (more than 20% in plastic deformation). The effect of superelasticity and residual strain are strongly affected by the martensitic

transformation temperature. As discussed in chapter 3, the austenitic transformation start temperature (A_s) is around 260 K and austenitic transformation finish temperature (A_f) is near 285 K. The martensitic transformation start temperature (Ms) is around 215 K and martensitic transformation finish temperature (Mf) is near 190 K. The measurements were performed at room temperature of 295 K where the crystalline phase is the austenitic B2 phase. Thus, the temperature induced phase transformation has no influence on the superelastic behavior related to the stress-induced martensitic transformation. The mechanical properties of the TiNi BMGC alloy at different unloading stages are shown in Fig. 4.1a. The compressive stress-strain curves of the TiNi BMGC alloy exhibit a smooth sigmoidal shape unlike the serrated flow typical for BMGs. The unloading curve during the martensitic transformation stage (point a, 650MPa) showing a reversible deformation argues for the superelastic effect in this alloy. The reversible phase transformation between martensite and austenite acting in the presence of the amorphous phase induce a small permanent residual strain. Unloading from 1700 MPa, between two yielding points after the beginning of the martensitic transformation, presents a partly plastic deformation that contains a small amount of elastic reversible strain. By contrast, unloading from 2000 MPa, after the second yielding point, induces almost no reversible superelastic deformation and indicates mostly plastic deformation and transformation induced plasticity at this stage. The above mechanical behaviors with different unloading stresses indicate that the TiNi BMGC still retains its superelasticity.

Fig. 4.1b shows the corresponding XRD patterns for the cross sections of TiNi crystalline/amorphous rod samples with different unloading stresses. The sharp diffraction peaks correspond to the B2-type TiNi crystalline phase, attributed to the austenitic phase which transforms to the martensitic B19'-type TiNi phase during deformation. The XRD patterns of the rod samples terminated loading at different stresses, namely 650, 1700 and 2000 MPa, from the corresponding loading-unloading curves (Fig. 4.1a), present the phase composition in different deformation process, after the superelastic and plastic deformation regimes. The diffraction patterns of the as-cast sample and the sample stopped loading at 650MPa (within the deformation-induced martensitic transformation process) show no big difference: both of them contain the peaks of austenitic phase (Fig. 4.1b). The martensitic phase peaks appear after loading up to near the second yielding point, 1700 MPa, which means after the superelasetic process some unrecoverable martensite formed in the alloy. The sample whose loading was stopped at 2000 MPa presents a similar XRD patterns as the fracture sample, the peaks are all corresponding to the martensite. After second yielding point the crystalline phase in the TiNi all changed to martensite phase from master austenite phase. The phase transform process is generated by loading stress.

During the compressive deformation process, the crack starts to shown at near 7% in strain (Fig. 4.2b), where the superelastic process finished and formed unrecoverable martensite phase. Before the second yielding point no crack and big microstructure changes could be found. The microstructure of fracture surface is shown in Fig. 4.2c and d. The backscattered SEM micrograph of cross surface (Fig. 4.2c) reveals a

net-work like structure similar with the as cast state. The bright area which is rich in amorphous phase is surrounding the dark area crystalline phase. Due to the high compressive stress, the round shape dendrites become narrow and tiny. The net-work structure was refinement by the compressive deformation process. The lateral surface of the fracture sample shown in Fig. 4.2d is same as we discussed before in chapter 3, both slip band lines and shear bands occur on the deformed lateral surface and also the mirror like flat region, typical for BMGs structure.

4.3 Influence of the amorphous phase on mechanical cycling behavior

The loading-unloading cyclic curves were obtained after different mechanical cycles with same unloading strain values, which is called hard-cycling mode [20]. It ensures relatively enough fraction of the martensitic transformation to take place at each cycle. Fig. 4.3a and 4.4a represent the 1st, 5th, 10th and 40th cycle of TiNi crystalline/amorphous alloy and TiNi-fully crystalline sample respectively. The reverse transformation finished at around 600 MPa for the 5% cycle, referred to as the unloading strain. The cyclic loading unloading behavior in the superelastic mode presents the three typical properties of low cycle mechanical fatigue in the TiNi shape memory alloys, both the plateau range and the hysteresis area shrink with the increase in the number of cycles at same time the residual strain increase, because of the increase in dislocation density produced by the reverse martensitic transformation [21]. The curves of TiNi BMGC alloy show more apparent phase transformation plateau area than the fully crystalline one.

XRD patterns (Fig. 4.3b and 4.4b) were obtained from the cross-section of rods with different loading cycles. As discussed in chapter three, TiNi crystalline/amorphous alloys contain an amorphous phase (a broad diffuse peak at 2θ of 37 °- 45 °), and sharp diffraction peaks corresponding to a B2-type austenite phase and a B19'-type martensite phase. No obvious peak shift or phase changes could be observed until 20 mechanical cyclic loading-unloading, but the pattern of sample experienced 40 mechanical cycles shows a small peak around 44 ° corresponding to the B19'-type martensitic phase. The accumulated strain inducing an unrecoverable martensite starts to show with the cyclic loading process which is similar to the mechanical fatigue effect. The mechanical cycling produces various micro mechanical changes such as slip, grain to grain interactions, dislocations, and lattice distortion during phase transformation and reverse process[22]. The accumulation of micro defects in the loading and unloading cycles influences the shape of strain-stress curves while only a tiny fraction of the retained martensite exists in the microstructures[23]. The X-ray diffraction peaks of the $Ti_{49.5}Ni_{50.5}$ as cast sample (Fig. 4.4b) correspond to the single TiNi-phase. The dominating peak of B2-TiNi austenitic phase is located around 2 theta of 41.6 degree where could demonstrate the distinction of phase changes in martensitic transformation. No obvious peak shift or phase changes could be observed as shown in Fig. 4.3b and 4.4b. However, the full width at half maximum (FWHM) of the peaks list in Table.4.1 indicate that, the value of FWHM increases while the cycle number increases, which can be attributed to the accumulation of the internal strain.

Low cycle mechanical-fatigue, referring as the decrease in the stress inducing martensitic transformation with increase in the number of mechanical cycles, was well discussed in shape memory alloy research field [24]. The effect was considered in the crystalline phase as generation of dislocations and localized slip during the transformation that induces accumulated irreversible strain [19]. However the creation of new dislocations is always required since dislocations assist in nucleation of the martensite [25]. Compared to $Ti_{49.5}Ni_{50.5}$ crystalline alloy, the TiNi crystalline/ amorphous alloys presents the sluggish fatigue effect after the cyclic loading in the superelastic deformation area owing to the presence of amorphous phase. In the composite alloy the amorphous layer interfaces likely act as high capacity sinks for dislocations from crystal [26]. It prevents accumulation of dislocations in the crystalline phase and, at same time promotes creation of new dislocation.

Plots in Fig. 4.5a depict the normalized martensitic transformation stress σ_m^n / σ_m^1 with increasing the loading-unloading cycles in two compared alloys. σ_m^1 is the first-round martensitic transformation stress and σ_m^n is the n-round martensitic transformation stress. The cyclic behavior for shape memory alloys is strongly affected by the critical phase transformation stress σ_m which reveals the properties varying with the cycles. The plateau range and σ_m^n apparently diminish with the increased cycling. It is corresponding to the previous studies which have shown generally decreases of the unloading plateau stress during cycling[27]. The cyclic deformation behavior was described as two steps of martensitic transformation [28]. Firstly, the deformation is accompanied by back and forth movements of the patent

martensite interfaces creating dislocations and resulting in larger residual strain. Secondly deformation associated with twinning is reversible without creating dislocations. However, compared with $Ti_{49.5}Ni_{50.5}$, the attenuation of σ_m^n in TiNi crystalline/amorphous alloy is relatively suppressed due to the presence of the amorphous phase preventing the accumulation of dislocation which is responsible for the low time mechanical-fatigue.

Fig. 4.5b presents the changes in the residual strain and hysteresis area with the cyclic numbers in the TiNi crystalline/amorphous alloy and the reference TiNi fully crystalline alloy. The hysteresis area of one cycle represents the energy loss during the loading-unloading process induced by movement of the interfaces. Both alloys show an obvious energy loss in the 1st cycle. For the same loading condition, TiNi crystalline/amorphous alloy exhibits much bigger area than the TiNi crystalline alloy. Because the amorphous phase in TiNi composite alloy acts as the sink for dislocations, the uneasy accumulation of dislocation leads to a smooth progress of martensitic transformation. On the other hand, rapid accumulation of dislocations in the TiNi fully crystalline hampers martensitic transformation process, and thus hysteresis area decreases much faster than that for the TiNi crystalline/amorphous alloy. The dislocations created during superelastic cycling are responsible for the accumulated irreversible strains. In Fig. 4.4b the residual strain for the $Ti_{49.5}Ni_{50.5}$ sample is larger than that of TiNi crystalline/amorphous alloys even after the 1st cycling route also due to the effect of the dislocation annihilation in the amorphous phase.

Fig. 4.6 shows the microstructures that observed in TEM foils prepared from the

TiNi crystalline/amorphous with superelastic cycles. The structure has no significant differences with the structure of the alloy in the as-cast state, which was discussed in chapter 3. The diffraction spots and diffuse halo in the selected area electron diffraction (SAED) patterns further confirm the amorphous-crystalline composite structure of TiNi dual-phase alloy as shown in the insets of Fig. 4.6a and 6b. The austenite structure with visible straight dislocation lines is clearly presented in Bright-field TEM micrograph (Fig. 4.6a). The amorphous phase surrounding the crystal acts as the grain boundary to restrict the dislocation slip during the loading process. The restriction effect results the depressed mechanical-fatigue behavior as shown in Fig. 4.5a. However some martensitic particles of submicron size could be found in TiNi crystalline/amorphous alloy after cycling as shown in Fig. 4.6b. Compared with previous works [23], fully-crystal TiNi alloy didn't exhibit residual martensite phase in the microstructures after cycling. It is assumed that martensite retransforms back to austenite in each cycle and the residual strain after cycling is due to dislocation slip and twinning deformation. However, the effect of amorphous phase in TiNi dual-phase alloy confines the martensite-austenite transition during unloading process that results in the remnant martensite phase and larger energy lose as shown in Figs. 4.6b and 4.5b We assume this is the reason why there is some martensite not transformed back to austenite after cycling. The restriction behavior of amorphous phase causes the obvious hysteresis loop and improves the mechanical-fatigue resistance property of TiNi crystalline/amorphous alloy.

Fig. 4.7 shows the TEM microstructure of TiNi crystalline/amorphous alloy with

20 mechanical cycles. Area A and area B display different contrasts corresponding to different phase composition. The diffraction spots and diffuse halo in the SAED patterns of area A shown in Fig. 4.7b reveal the composite of B19’ martensite and amorphous phase in the light area, the SAED patterns in Fig. 4.7c indicates the B2 austenite phase in the dark area. The dislocations are locating in the dark area austenite phase but not in the light area which has an amorphous phase, which demonstrates the effect of the amorphous phase as a sink for the dislocation. The dislocation movement was blocked by the amorphous phase between the austenite phases. As reported by Y. Wang, *et al.* [26], they use molecular dynamics (MD) simulation to get the conclusion that the dislocation structures, which could localize in grains and at grain boundaries and cause large stress concentrations and keep by jumping between grains, have been disrupts and dissolved by the amorphous layers. The bursting dislocations at the beginning of deformation decrease dramatically because of the attraction and annihilation of dislocations in the amorphous phase. Not only the mobile dislocation but also the existing sessile dislocations are sink in the amorphous disordered structure because of the reactions with new mobile dislocations. In this case, the activity dislocations are beneficial to the reversibility of phase transformation process in TiNi dual-phase alloy leading to good mechanical fatigue properties in low cycling mode.

4.4 Conclusion

We fabricated TiNi composite alloy with dual crystalline and amorphous phases.

The TiNi crystalline/amorphous alloy exhibits a good combination of strength and ductility in compressive deformation. The strain-stress curve shows a sigmoidal shape with a plateau stage corresponding to the martensitic transformation. The phase transformation induces superelastic behavior which causes large elastic strain. Low cycle mechanical-fatigue properties during superelastic cyclic loading perform differently in TiNi-crystalline/amorphous alloy and TiNi fully crystalline alloy. TiNi dual-phase alloy show better anti damping performance than the fully crystal one. The low cycle mechanical fatigue induced the decrease in σ_m and hysteresis area shrink is suppressed in the TiNi crystalline-amorphous alloy due to the presence of the amorphous phase. During the deformation the amorphous phase, which is surrounding the crystalline phase, acts as a sink for dislocations generated upon the superelastic cycling. It prevents the accumulation of dislocations, and simultaneously promotes creation of the new dislocations. The amorphous phase in TiNi dual-phase alloy assists to the smooth progress of the martensitic transformation, dramatically decreases the bursting dislocations at the beginning of deformation by the attraction and annihilation. Both the mobile and existing sessile dislocations are sink in the amorphous disordered structure by the reactions with new mobile dislocations and beneficial to the reversibility of phase transformation between martensite and austenite. The TiNi amorphous composites pave a new way to fabricate and design composite material with high ductility and good anti-fatigue behaviors.

References

1. B.A. Sun, and W.H. Wang, Progress in Materials Science, 2015. 74: p. 211-307.

2. Y.H. Liu, G. Wang, R.J. Wang, D.Q. Zhao, M.X. Pan, W.H. Wang, science, 2007. 315(5817): p. 1385-1388.

3. D.V. Louzguine-Luzgin, Journal of Alloys and Compounds, 2014. 586: p. 216-219.

4. S. Küchemann, C. Liu, E.M. Dufresne, J. Shin, R. Maaß, Physical Review B, 2018. 97(1): p. 014204.

5. K. Georgarakis, M. Aljerf, Y. Li, A. LeMoulec, F. Charlot, A.R. Yavari, K. Chornokhvostenko, E. Tabachnikova, G.A. Evangelakis, D.B. Miracle, A.L. Greer, and T. Zhang, Applied Physics Letters, 2008. 93(3): p. 031907.

6. Greer, A.L., Metallic glasses. Science, 1995. 267(5206): p. 1947-1953.

7. A.A. Tsarkov, A.Yu. Churyumov, V.Yu. Zadorozhnyy, D.V. Louzguine-Luzgin, Journal of Alloys and Compounds, 2016. 658: p. 402-407.

8. J.W. Qiao, H. Jia, and P.K. Liaw, Materials Science and Engineering: R: Reports, 2016. 100: p. 1-69.

9. P. Gargarella, S. Pauly, K.K. Song, J. Hu, E. Kerscher, J. Eckert, Acta Materialia, 2013. 61(1): p. 151-162.

10. D.C. Hofmann, J.Y. Suh, A. Wiest, M.L. Lind, M.D. Demetriou, W.L. Johnson, Proceedings of the National Academy of Sciences, 2008. 105(51): p. 20136-20140.

11. K.K. Song, S. Pauly, Y. Zhang, R. Li, S. Gorantla, N. Narayanan, U. Ku, T. Gemminga, J. Eckert, Acta Materialia, 2012. 60(17): p. 6000-6012.

12. I.S. Golovin, V.Yu. Zadorozhnyy, A.Yu. Churyumova, D.V. Louzguine-Luzgin,

Journal of Alloys and Compounds, 2013. 579: p. 633-637.

13. R. DesRoches, J. McCormick, and M. Delemont, Journal of Structural Engineering, 2004. 130(1): p. 38-46.
14. S. Miyazaki, K. Mizukoshi, T. Ueki, T. Sakuma, Y. Liu, Materials Science and Engineering: A, 1999. 273: p. 658-663.
15. K.N. Melton, O. Mercier, Acta Metallurgica, 1979. 27(1): p. 137-144.
16. B. Strnade, S. Ohashi, H. Ohtsuka, S. Miyazaki, T. Ishihara, Materials Science and Engineering A 203 (1995): p. 187-196
17. K. Gall, H. Maier, Acta Materialia, 2002. 50(18): p. 4643-4657.
18. R. Hamilton, H. Sehitoglu, Y. Chumlyakov, H. Maier, Acta Materialia, 2004. 52(11): p. 3383-3402.
19. J. Hurley, A. Ortega, J. Lechniak, K. Gall, H. Maier, Zeitschrift für Metallkunde, 2003. 94(5): p. 547-552.
20. S. Myazaki, Y. Sugaya, K. Otsuka, in Proceedings of the MRS International Meeting on Advanced Materials. 1988.
21. T. Ikeda, Journal of Intelligent Material Systems and Structures, 2008. 19(5): p. 533-540.
22. S. Manchiraju, D. Gaydosh, O. Benafan, R. Noebe, R. Vaidyanathan, P.M. Anderson, Acta Materialia, 2011. 59(13): p. 5238-5249.
23. R. Delville, B. Malard, J. Pilch, P. Sittner, D. Schryvers, International Journal of Plasticity, 2011. 27(2): p. 282-297.
24. G. Eggeler, E. Hornbogen, A. Yawny, A. Heckmann, M. Wagner, Materials

Science and Engineering: A, 2004. 378(1-2): p. 24-33.

25. T. Simon, A. Kroger, C. Somsen, A. Dlouhy, G. Eggeler, Acta Materialia, 2010. 58(5): p. 1850-1860.
26. Y. Wang, J. Li, A.V. Hamza, T.W. Barbee, Proceedings of the National Academy of Sciences, 2007. 104(27): p. 11155-60.
27. A.F. Saleeb, A. Kumar, S.A. Padula, B. Dhakal, Mechanics of Materials, 2013. 63: p. 21-47.
28. A. Yawny, M. Sade, G. Eggeler, Zeitschrift für metallkunde, 2005. 96(6): p. 608-618.

.

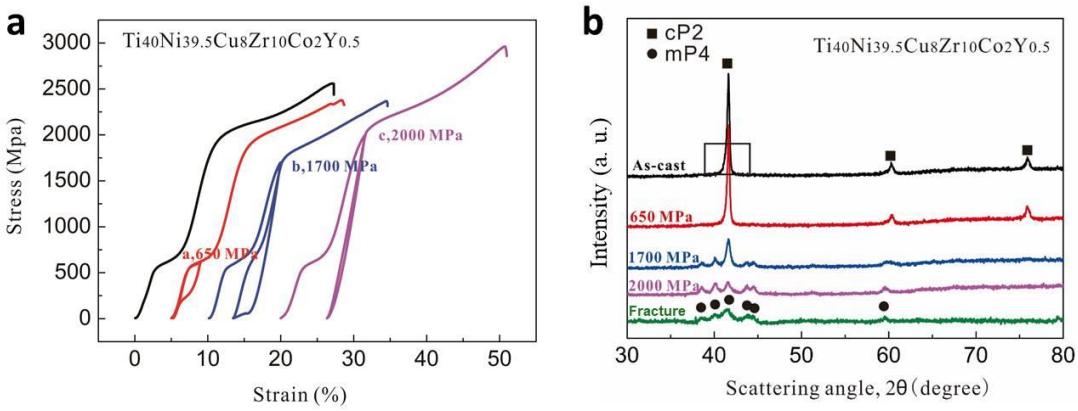

Fig. 4.1. The strain-stress curves of TiNi-based crystalline/amorphous alloy with different unloading stress (a) and the corresponding XRD patterns (b).

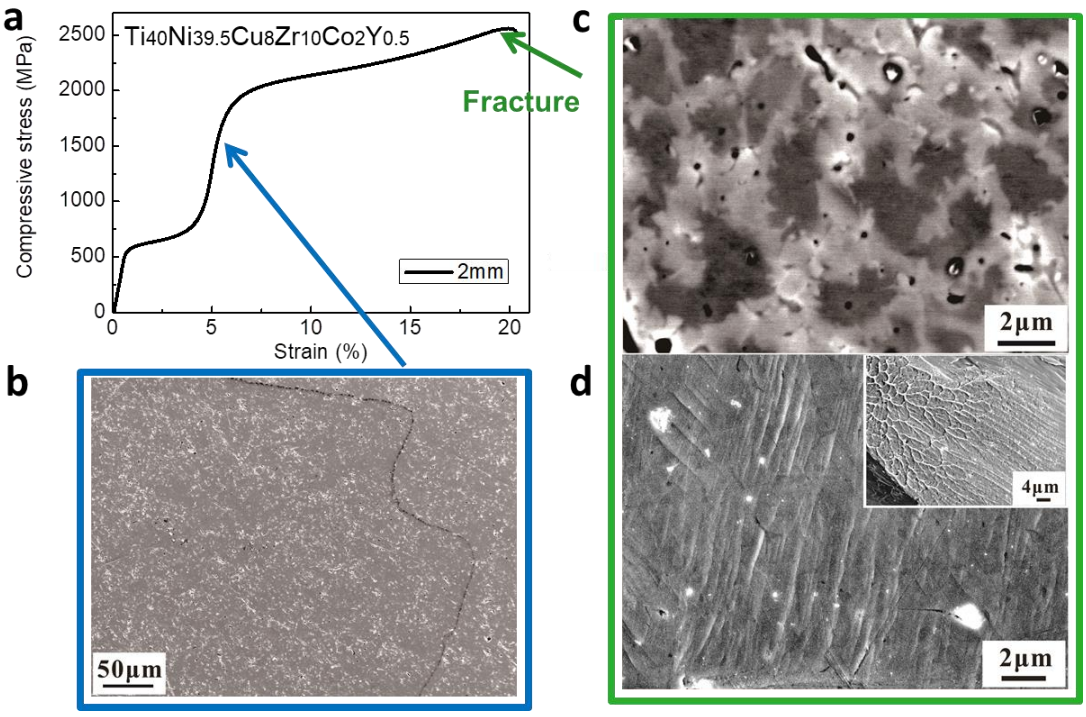

Fig. 4.2 the microstructure in different compressive process states of TiNi crystalline/ amorphous alloy

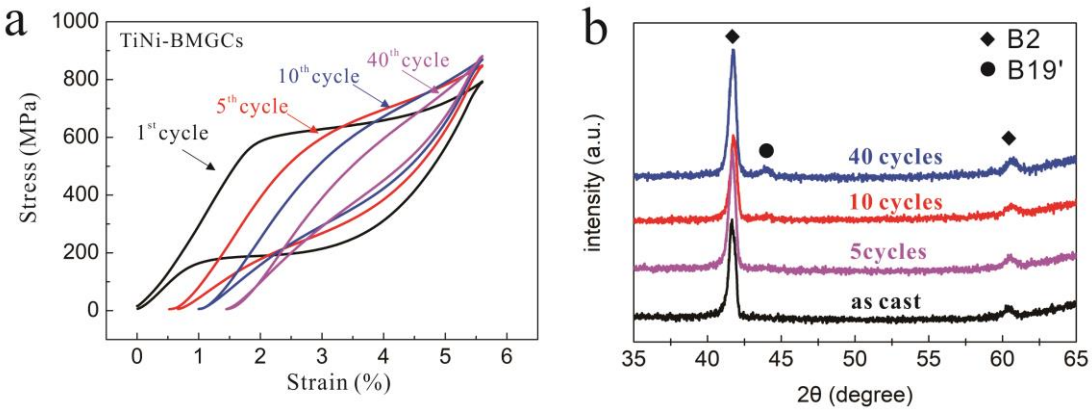

Fig. 4.3. (a) The loading-unloading cycle curves of $Ti_{40}Ni_{39.5}Cu_8Zr_{10}Co_2Y_{0.5}$ crystalline/amorphous alloy after different mechanical cycles (1st, 5th, 10th, 40th) with same total strain before unloading and (b) the corresponding XRD patterns

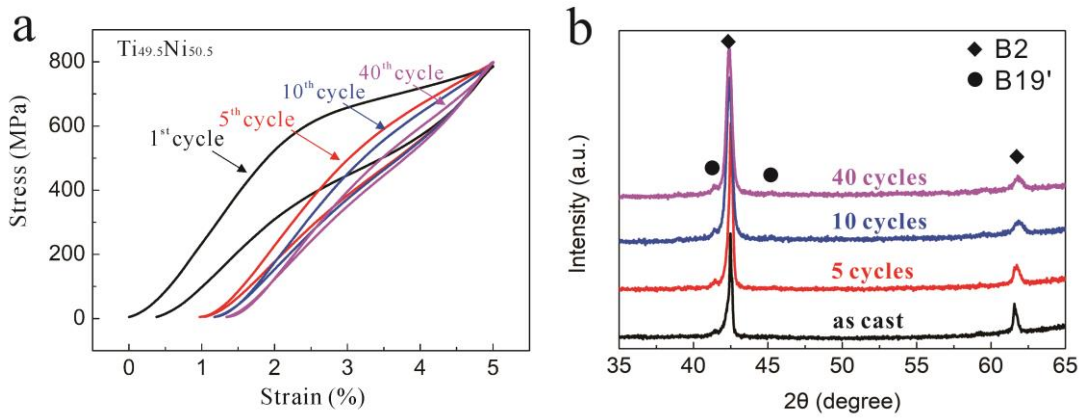

Fig. 4.4. (a) The loading-unloading cycle curves of $Ti_{49.5}Ni_{50.5}$ fully crystalline alloy after different mechanical cycles (1st, 5th, 10th, 40th) with same total strain before unloading and (b) the corresponding XRD patterns

Table 4.1 the value of the full width at half maximum (FWHM) as a function of mechanical cycling

FWHM	**As cast**	**5 cycles**	**10 cycles**	**20 cycles**	**40 cycles**	**80 cycles**
TiNi-BMGC	0.5477	0.5514	0.5538	0.56032	0.57162	0.5991
$Ti_{49.5}Ni_{50.5}$	0.29876	0.32852	0.36753	0.42298	0.46015	

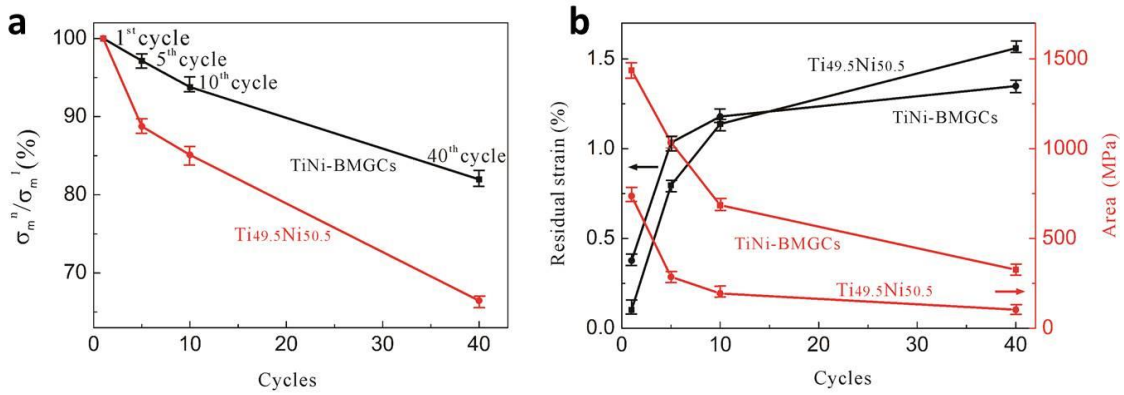

Fig. 4.5. The plots of martensitic transformation stress (a) and the plots of residual strain and hysteresis area (b) with different cycles.

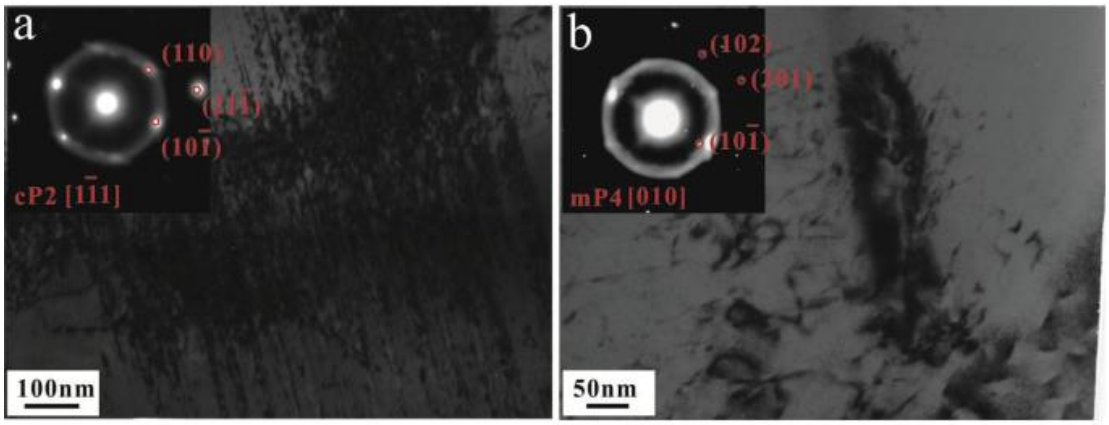

Fig. 4.6. TEM images for TiNi BMGC alloy after mechanical cycling (10 cycles). (a), Bright-field TEM micrograph showing cP2-austenite structure with corresponding SAED pattern shown in the inset. Straight lines possibly indicate dislocations created by cycling martensitic transformation. (b), The micrograph including mP4-martensite phase with corresponding SAED pattern shown in the inset.

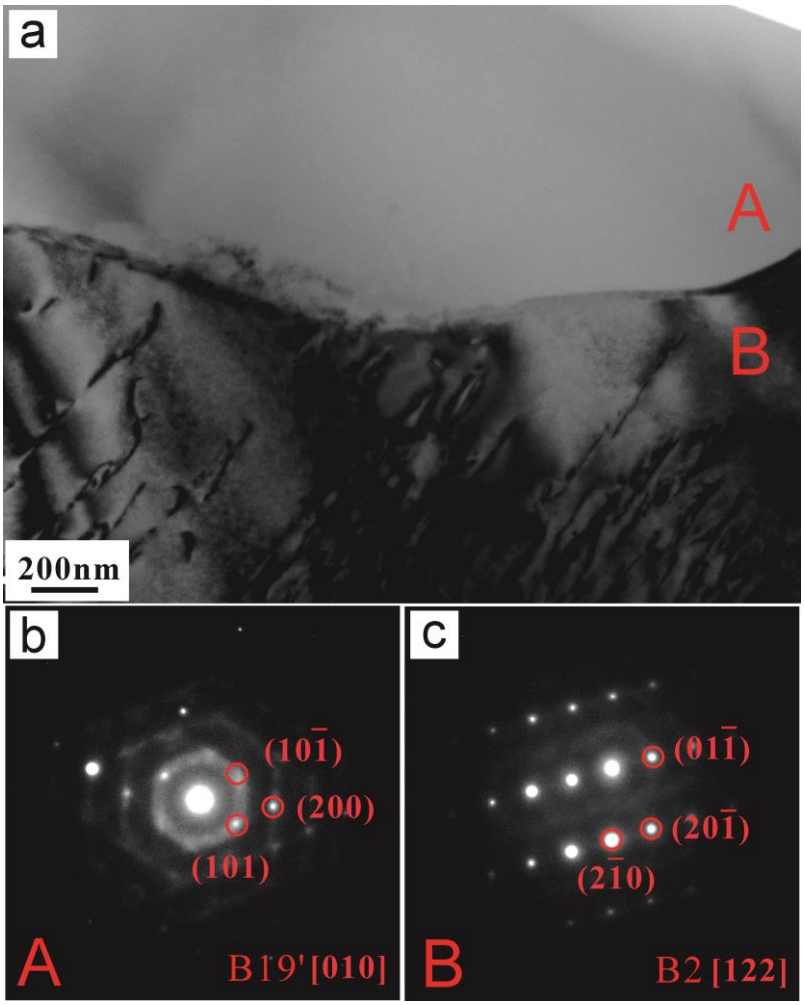

Fig. 4.7. TEM images for TiNi BMGC alloy after mechanical cycling (20 cycles). (a), Bright-field TEM micrograph showing light area martensite and amorphous structure with corresponding SAED (b), the dark area B2-austenite structure with corresponding SAED pattern(c). the dislocation forming and moving in the austenite phase stopped at the phase boundary

Chapter 5

The effect of cryogenic thermal cyclic processing on the mechanical properties

5.1 Introduction

Amorphous alloys (metallic glasses) have drawn a lot of attention in both functional and structural materials due to the unique properties that exhibiting excellent fracture strength combined with some other attractive features like high hardness, corrosion resistance and large yielding strains [1-3]. At same time they show some drawbacks like poor plasticity and catastrophic failure at room temperature, which is caused by the intrinsic no long-rang ordered microstructure and stress concentrating in relatively narrow shear band regions [4, 5]. The introduction of nano-crystalline particles or elastic heterogeneity was established to be effective in improving the mechanical properties of metallic glasses such as limited ductility [6-8]. Metallic glasses composites with dual amorphous and crystalline phase were fabricated by embedding crystal in the amorphous matrix as a second phase that restricts the propagation of shear bands and further impedes the catastrophic failure [7]. TiNi alloys with almost equiatomic B2 phase have great potential in the plastic property due to the recoverable phase transformation between austenite phase and martensite phase. Since then metallic glass composites that using B2 phase as the second phase, like TiNi [9-11], TiCu [12, 13], CuZr [14, 15] rise in response in material science. The cyclic loading-unloading under Superelastic mode inducing low

cycles mechanical fatigue is a generic characteristic feature of the TiNi alloys [16, 17]. During the cyclic loading process the accumulation of dislocation and internal stress assist the formation of the stress-induced martensitic transformation [18]. Therefore the critical martensite phase transformation stress is decrease with the cyclic number increase.

Different cooling rates in the casting process from liquid to the amorphous alloy induce different energy states of the amorphous solid. The random atomically disordered structure indicates the amorphous alloy at a high potential energy level which can be transformed to a lower energy state, namely relaxation or aging [19]. Relaxation is undesirable to the service reliability since the generating of brittleness. The higher energy state metallic glasses normally have higher plasticity. Rejuvenation which is the opposite or recovery effect to relaxation, increasing in the enthalpy and free volume leads to an enhancement of the metallic glasses plasticity at room temperature [20]. Controlling the structural rejuvenation is meaningful to improve the mechanical properties of amorphous alloys. Both mechanical and thermal methods were carried out to realize rejuvenation in the metallic glasses alloy, temperature and stress are equivalent on the dynamics of amorphous alloys. Mechanical rejuvenation can be driven by severe plastic deformation techniques such as high pressure torsion, shot-peening and cold rolling [21]. The severe plastic deformation induces disordering insider shear bands in the plastic deformation process that happen the shear dilatation, and hence, the amorphous transform into an inhomogeneous non-equilibrium state realizing the rejuvenation [22]. It has been reported that thermal

loading via heating and quenching process also realizes a local rejuvenation control.

Recently, an attractive and simple method [23], cryogenic thermal cycling between room and liquid nitrogen temperatures was introduced by Ketov et al. to achieve rejuvenation and improve the plasticity of the BMGs. The intrinsic disordered amorphous structure causes heterogeneous thermal expansion or contraction, therefore cyclic temperature changes induce local stress between the disordered atoms which is enough for an elastic strains to occur [24]. Thermal cycling is well applied for poly crystalline materials which have highly anisotropic thermal expansions, due to the simply changing in whole samples of any shape and size without any destruction.

In the present work, we applied the cryogenic thermal cycling method to TiNi based crystalline/amorphous alloy of composition $Ti_{40}Ni_{39.5}Cu_8Zr_{10}Co_2Y_{0.5}$. The influence of cryogenic thermal cycling on the mechanical properties was investigated. Homogeneous crystalline structure experiences affine contraction and expansion during cooling and heating process, inducing no any internal stresses and microstructure changes. However the non-affine atomic disordered structure in the heterogeneous metallic glasses induces internal stresses during the cryogenic thermal cycling realizes the rejuvenation effect. The boundary area in dual-phase alloys between crystalline and amorphous phases show much different coefficient of thermal expansion that rejuvenation effect is easy happens.

5.2 The cryogenic thermal cycling process

As shown in Fig. 5.1, the cryogenic thermal cycling process was performed between room temperature (303K) and liquid nitrogen temperature (77K). During the thermal cycling process many factors could be the tailored, the cyclic temperature, holding times of each cycle, cooling and heating rate. We focus the property changes induced by the thermal cycling so specified all the parameters. We do the cycling between the liquid nitrogen and ethanol which was kept at 303K. Samples were held for two minutes in each liquid and without any treatment moved to another solution.

5.3 The mechanical behavior after cryogenic thermal cycling

The compressive curves of the as-cast sample and the samples after cryogenic thermal cycling (for 10, 30, 50 times) are shown in Fig. 5.2. The critical stress inducing martensitic phase transformation (σ_m) shows an increase after the cryogenic thermal cycling treatment. Plots in Fig. 5.2b depict that the value of σ_m increases with the cryogenic thermal cycles. The critical stress σ_m increases with cyclic number increase in the beginning, showing a maximum value near 10 cycles almost 10 % higher than the as cast state, then followed by a decrease. Until 50 cycles, the value of σ_m in the thermally treated sample is higher than in the as cast sample.

As discussed in chapter 4, the cyclic loading-unloading behavior induces low time mechanical fatigue and the σ_m decreases. The typical fatigue defect that needs to be prevented is the decrease of critical phase transformation stress. The phase transformation happens when the elastic deformation finishes, the increasing volume fraction is saturated[25]. In general the larger recovering strain is obtained in the

samples with higher critical phase transformation stress [26]. The hysteresis area is increasing with increase in the critical stress σ_m which means that the dissipated work and recoverable strain energy in one loading unloading loop is increase indicating a better mechanical stability. The internal friction resistance against movement of the interface between the parent B2 phase and the B19' martensite phase could increase the phase transformation stress [27].

Fig. 5.3 reveals the loading unloading cyclic behavior of the as cast sample and the sample with cryogenic thermal cycling (10 cycles). The mechanical cyclic behaviors were obtained with three compressive cycles and unloading at same strain values. Fig. 5.3b represents stress-strain curves of the superelastic loading-unloading process compared to the as-cast alloy and the one underwent 10 times cryogenic thermal cycling before the mechanical test. The cyclic loading behavior in the superelastic mode takes place in the way similar to what was found in chapter 4. It reveals the typical behavior of the low cycles fatigue in TiNi shape memory alloys: decrease of the critical martensitic transformation stress and hysteresis area but increase of the residual strain. The one treated by the cryogenic thermal cycling shows more obvious hysteresis loop than the as-cast one.

The TiNi crystalline/ amorphous alloy after cryogenic thermal cycling presents a higher σ_m then the as cast state, induces larger transformation plateau area and hysteresis loop. More energy is dissipated at each cycle in the cryogenic thermal cyclic samples. Plots in Fig. 5.3c and 3d depict the value of σ_m and hysteresis area as a function of cryogenic thermal cycles. The tendency displays a decrease in the σ_m and

shrink of the hysteresis area in both the as-cast sample and the thermal-treated one. The critical phase transformation stress σ_m strongly affects the cyclic behavior for shape memory alloys. The plateau range and n-round transformation stress diminish with increasing the number of cycles. However compared with the as-cast sample, the attenuation of σ_m in thermally cycled sample is relatively weak because the cryogenic thermal cycling process dramatically increases the σ_m before the mechanical cycling. σ_m of the third cycle in the thermal treated sample is even higher than the first σ_m of as cast one. The same phenomenon is observed in the hysteresis width changes on the loading unloading cycle treatment.

Fig. 5.4 reveals the different compressive behavior of the samples with 10 thermal cycles and without thermal treatment, both two samples experienced 3 mechanical loading unloading cycles at firsty. Fig. 5.4a shows the 3 loading unloading cycles which both sample A and sample B carried out and the loops are similar in this two samples. The low cycles mechanical fatigue behavior shows same typical tendencies as we discussed in chapter 4. The critical martensitic transformation stress and plateau area decrease with the cycles. After the mechanical cycling, we did different treatments for these two samples, sample A experienced the cryogenic thermal cycling and sample B just relax in the air. Then the compressive test finished in both sample A and sample B. The strain stress curves of two samples are displayed in Fig. 5.4b. Sample A experience 3 loading-unloading cycles and 10 cryogenic thermal cycles, sample B experience only mechanical cycling. The sample B shows low martensitic phase transformation stress (σ_m) in final stain stress curves. Fig. 5.4c

depicts the plots of σ_m as a function of loading unloading cycles, both samples show similar decrease tendency at the beginning 3cycles. The σ_m of sample A shows nearly 10% increase at the 4^{th} test since experience the cryogenic thermal cycling. In sample B after relax in air the σ_m also shows recover but not over than the initial transformation stress. Fig. 5.4d reveals the XRD patterns of sample A comparing the as cast state (black curve), then after mechanical loading-unloading process (the red curve) showing a small martensite B19' peak, but after the cryogenic thermal cycling the martensite peak disappeared (blue curve). The unrecoverable martensite induced by the low cycles mechanical fatigue process could be activation by the thermal treatment and transform to room temperature stable austenite phase, shown in the XRD results. So we think the cryogenic thermal cycling defense the σ_m decrease by the mechanical fatigue in the TiNi crystalline/ amorphous alloy.

5.4 The mechanism of cryogenic thermal cycling effect

Fig. 5.5 represents the compressive stress strain curves of the TiNi fully crystalline alloy ($Ti_{49.5}Ni_{50.5}$) with different cycles of cryogenic thermal treatment. The mechanical behaviors show no obvious differences by thermal cycling compare with the TiNi crystalline/ amorphous alloy. The critical martensitic transformation stress σ_m of the thermally cycled samples are plotted in Fig. 5.5b. The values are slightly fluctuating around 800 MPa. On the other hand the σ_m of TiNi crystalline/ amorphous alloys (Fig. 5.2b) shows an obvious difference after different thermal cycles. The effect of the cryogenic thermal cycling has not acted in the TiNi fully

crystalline alloy which means that the existing of amorphous phase in the composite is an important factor.

Fig. 5.6a and b show the differential scanning calorimetry (DSC) traces of heating the melt-spun TiNi ribbons with different cooling rate. During the melt-spin process the cooling rate of the liquid alloy could be controlled by the rotation speed of the Cu wheel, higher rotation speed represent higher cooling rate it is easy to form an amorphous phase at such conditions. The corresponding XRD patterns reveal the peak of crystalline phase in the low cooling rate ribbon sample (Fig. 5.6c), while the high cooling rate one (Fig. 5.6d) shows only a broad peak which indicates a fully amorphous phase. DSC traces on heating of amorphous ribbons show an exothermal peak before glass transition at T_g. The shaded areas represent the overall heat of relaxation named ΔH_{rel} by subtraction of successive traces of specific heat, associated with the exothermic reaction. The changes of ΔH_{rel} have been used to characterize the effects of treatment, both thermal and mechanical, on metallic glasses. The heat of relaxation is increased after cryogenic thermal cycles in both low cooling rate ribbon and high cooling rate ribbon revealing the effect of rejuvenation. But the increase is much more obvious in the higher one which means that the amorphous phase triggered the rejuvenation process. As reported in the previous work [23], rejuvenation induced by the cryogenic thermal cycling leads to the decrease of the initial yield stress σ_y for the amorphous alloys. While it shows the opposite effect with the TiNi crystalline/amorphous alloys in which the critical stress for the phase transformation is increased by the cryogenic thermal cyclic treatment. The volume

fraction of the amorphous phase in the TiNi BMG composite is relatively low, therefore the rejuvenation of the amorphous phase inducing the decrease of the yield stress has no big influence in the TiNi dual phase alloys.

Fig. 5.7 shows XRD patterns taken from the cross surface of TiNi alloys after different cycles of cryogenic thermal treatment (a) and the patterns of fracture surface (c). Fig. 5.7a reveals that the B2 austenite phase was observed in the all of the specimens and show no big differences in XRD patterns. However, the magnified patterns between 2θ of 41 and 42degrees (Fig. 5.7b) display a shoulder near the main peak. The TiNi-B2 (cubic) phase and TiNi-B19' (monoclinic) phase both have a peak near 2θ of 41.5 degree, B2 facet (110) and B19' facet (020), respectively. It's hard to distinguish them in the normal XRD analysis. The patterns comparing as cast sample with B2 austenite phase and the broken surface with B19' martensite phase are shown in Fig. 5.7c. It reveals that the martensite peak (020) is located at the position of the shoulder of austenite peak (110). Thus, a weak fluctuation near the main B2 peak is considered as (020) of B19'. The shoulder in the pattern of the as cast sample is much more conspicuous than that in the 10-cycles thermally treated one, indicates that the volume fraction of martensite decreases after cryogenic thermal cycling. The residual martensite in the as-cast state was rejuvenated by the thermal cyclic process to attend the recoverable phase transformation that induces less martensite can be found at the room temperature austenite-stable state. The yield stress of the martensite phase is relatively low and more austenite phase at higher temperature generally induces a higher phase transformation stress as reported [28-30]. Thus, the responsibility of

critical stress increase in Fig. 5.2a is partly undertaken by the reduced fraction of martensite phase during cryogenic thermal cycling. The reduction of martensite phase is most obvious after 10 thermal cycles. Thus the corresponding critical stress for the martensitic phase transformation observed in the stress-strain curve (Fig. 5.2b) is the highest.

The microstructures shown in Fig. 5.8 were observed in TEM foils prepared from the TiNi as cast sample (Fig. 5.8a,c,e) and the 10-cycles cryogeniccally thermal treated sample (Fig. 5.8b,d,f). As we discussed before, the main phase of the TiNi crystalline/amorphous alloy is the B2 austenite phase, which is displayed as the dark area. The TEM images of Fig. 5.8a and 5.8b reveal the relatively light areas which correspond to the amorphous phase. During the casting process, three phases were formed, the high temperature stable austenite phase, the disordered amorphous phase, and a small amount of the low temperature martensite phase. The martensite phase is restricted by the amorphous phase and could exist at room temperature, so that the amorphous phase always appears close to the martensitic phase in the as-cast state. The twinning plate type martensite structure near the amorphous phase is shown in the Fig. 5.8a and the corresponding SAED patterns in Fig. 5.8b reveal the B19' martensite spots and a halo indicating the presence of amorphous structure. The sample after 10 cryogenic cycles exhibits fine lamellar structure and the corresponding SAED patterns shown in Fig. 5.8d indicates a layer type structure consisting of the austenite phase and the amorphous one. The results match well with those of the XRD analysis shown in Fig. 5.7 that the fraction of the martensite phase

was reduced after 10 thermal cycles. In the mixed two phases structure the crystalline B2 region and the amorphous region are formed as narrow alternating layers. The high resolution TEM image (Fig. 5.8f) displays the lamellar structure of the amorphous and crystalline phases which is different from that of the as-cast state (Fig. 5.8e) when the two phases are mixed in a disordered way. The amorphous layers in the lamellar structure act as the barrier for the motion of dislocations during the deformation, hence the critical phase transformation stress is increased after 10 thermal cycles (Fig. 5.2). Both the changes in phase composition and in the microstructure by the cryogenic thermal cycling play important role for the mechanical properties improvement.

5.5 conclusion

We applied the cryogenic thermal cycling to the $Ti_{40}Ni_{39.5}Cu_8Zr_{10}Co_2Y_{0.5}$ alloy with dual crystalline and amorphous structures. The mechanical behavior of the as-cast sample and cryogenically cyclized sample is different. The stress strain curves display an increase of the critical stress (σ_m) for the martensitic phase transformation which is opposite to the low cycle mechanical fatigue. The increase of σ_m cannot be found in the $Ti_{49.5}Ni_{50.5}$ fully crystalline alloy after cryogenic thermal cycling, which means that the presence of amorphous phase in the TiNi BMG composite alloy acts as an important factor responsible for the increase in σ_m by thermal cycling. The TiNi crystalline/ amorphous alloy has three phases in the as-cast state, B2 austenite (main phase), amorphous phase and a small amount of B19’ martensite phase. The TEM

images reveal that the amorphous phase normally appears around the B19’ martensite phase in the as cast state. It indicates that the low temperature stable martensite phase which should transform to B2 austenite phase at room temperature was restricted by the amorphous phase during the casting process. The XRD patterns show a decrease of the martensite peak after cryogenic thermal cycling indicating that the thermal treatment activates the martensite phase and enables it transformation into the austenite phase during the cycling process and finally leads to the decrease of the amount martensitic phase at room temperature. The yield stress of martensite phase is relatively low compares with the austenite phase, thus the reducing of marteinsite phase induces the increase of phase transformation stress σ_m. On the other hand, the crystalline structure near amorphous phase was transformed during the thermal cycling process, the as cast state twinning martensite phase changes to austenite phase with lamellar structure. The layer-type structure blocks the movement of dislocation which is also the reason for the increases in the critical stress for phase transformation.

References

1. K. Fujita, T. Hashimoto, W. Zhang, H. Nishiyama, C. Ma, H. Kimuta, A. Inoue, Reviews on advanced materials science, 2008. 18:p. 137-139
2. J.E. Gao, Z.P. Chen, Q. Du, H.X. Li, Y. Wu, H. Wang, X.J. Liu, Acta Materialia, 2013. 61(9): p. 3214-3223.
3. W.L. Johnson, Fundamental aspects of bulk metallic glass formation in multicomponent alloys. in Materials science forum. 1996. Trans Tech Publ.
4. A. Inoue, B. Shen, and A. Takeuchi, Materials Science and Engineering: A, 2006. 441(1-2): p. 18-25.
5. A.L. Greer, Metallic glasses… on the threshold. Materials Today, 2009. 12(1-2): p. 14-22.
6. J.W. Qiao, J.T. Zhang, F. Jiang, Y. Zhang, P.K. Liaw, Materials Science and Engineering: A, 2010. 527(29-30): p. 7752-7756.
7. R. Wei, S. Yang, C.J. Zhang, L. He, Materials Science and Engineering: A, 2014. 606: p. 268-275.
8. J. Qiao, H. Jia, and P.K. Liaw, Materials Science and Engineering: R: Reports, 2016. 100: p. 1-69.
9. D.V. Louzguine-Luzgin, A. Vinogradov, G. Xie, S. Li , A. Lazarev , S. Hashimoto, A. Inoue, Philosophical Magazine, 2009. 89(32): p. 2887-2901.
10. J. Jiang, D.X. Wei, T. Wada, D.V. Louzguine-Luzgin, H.Kato, Journal of Alloys and Compounds, 2018. 768: p. 176-180.
11. J Jiang, S Ketov, H Kato, D.V. Louzguine-Luzgin, Materials Science and

Engineering: A, 2017. 704: p. 147-153.

12. P. Gargarella, S. Pauly, M.S. Khoshkhoo, U. Kühn, Acta Materialia, 2014. 65: p. 259-269.
13. P. Gargarella, S. Pauly, K.K. Song, J. Hu, N.S. Barekar, Acta Materialia, 2013. 61(1): p. 151-162.
14. S. Pauly, J. Das, J. Bednarcik, N. Mattern, K.B. Kim, Scripta Materialia, 2009. 60(6): p. 431-434.
15. S. Pauly, G. Liu, G. Wang, U. Kühn, N. Mattern, J. Eckert, Acta Materialia, 2009. 57(18): p. 5445-5453.
16. K. Otsuka, X. Ren, Intermetallics, 1999.7: p. 511-528
17. R. DesRoches, J. McCormick, M. Delemont, Journal of Structural Engineering, 2004.130: p. 38-46.
18. R. Delville, B. Malard, J. Pilch, P .Sittner, D.Schryvers, International Journal of Plasticity, 2011. 27(2): p. 282-297.
19. C. Suryanarayana, and A. Inoue, Bulk metallic glasses. 2017: CRC press.
20. A. Concustell, F.O. Méar, S. Surinach, A.L. Greer, Philosophical Magazine Letters, 2009. 89(12): p. 831-840.
21. J. Saida, R. Yamada, M. Wakeda. Journal of Science and Technology of Advanced Materials, 2017. 18(1): p. 152-162.
22. W. Guo, R. Yamada, J. Saida, S. Lu, S. Wu, Journal of Non-Crystalline Solids, 2018. 498: p. 8-13.
23. S.V. Ketov, Y.H. Sun, S. Nachum, Z. Lu, A Checchi, A. R. Beraldin, H. Y. Bai, W.

H. Wang, D. V. Louzguine-Luzgin, M. A. Carpenter, A. L. Greer, Nature, 2015. 524(7564): p. 200-203.

24. T.C. Hufnagel, Nature materials, 2015. 14(9): p. 867-868.
25. I. Kaya, H. Tobe, H.E. Karaca, B. Basaran, Materials Science and Engineering: A, 2016. 678: p. 93-100.
26. S. Miyazaki, K. Mizukoshi, T. Ueki, T. Sakuma, Materials Science and Engineering: A, 1999. 273: p. 658-663.
27. H. Tobushi, Y. Shimeno, T. Hachisuka, K. Tanaka, Mechanics of Materials, 1998. 30(2): p. 141-150.
28. L. Krone, J. Mentz, M. Bram, H.P. Buchkremer, D. Stöver, M. Wagner, G. Eggeler, M. Epple, *et.al*, Advance Engineering Materials, 2005. 7(7): p. 613-620.
29. T. Inamura, Y. Takahashi, H. Hosoda, K. Wakashima, T. Nagase, T. Nakano, Y. Umakoshi, S. Miyazaki, Materials transactions, 2006, 47(3): p. 540-545
30. A.F. Saleeb, B. Dhakal, S. Dilibal, J.S. Owusu-Danquah, S.A. Padula, Mechanics of Materials, 2015. 80: p. 67-86.

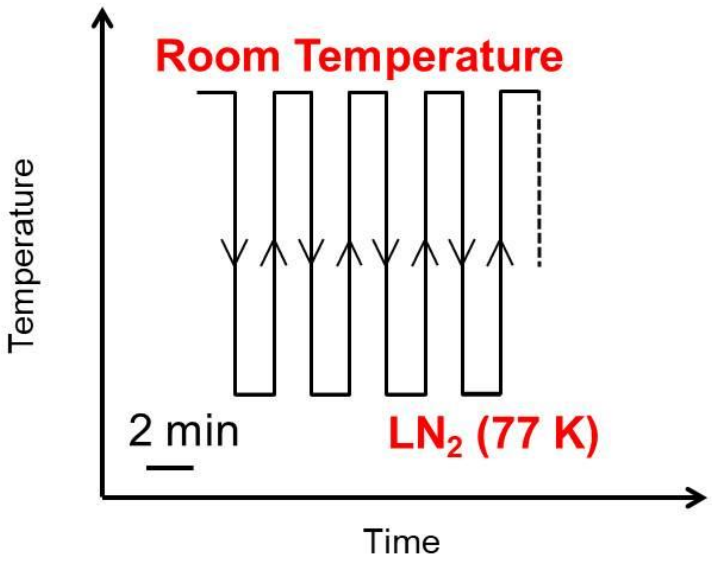

Fig. 5.1. The cryogenic thermal cycling process

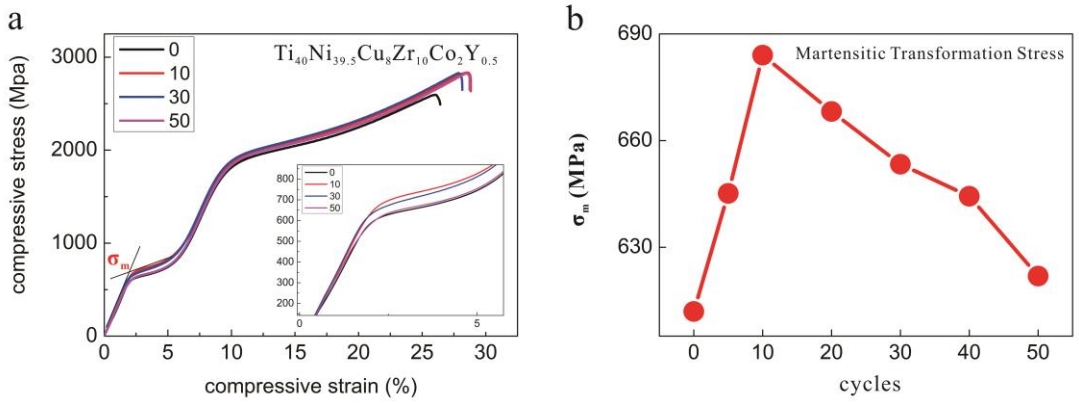

Fig. 5.2. The compressive stress strain curves of the TiNi cyrstalline/amorphous alloys with different cycles of cryogenic thermal cycling (a), and the coressponding critial stress for martensitic phase transformation, σ_m, functioned with the thermal cyclic number increase (b).

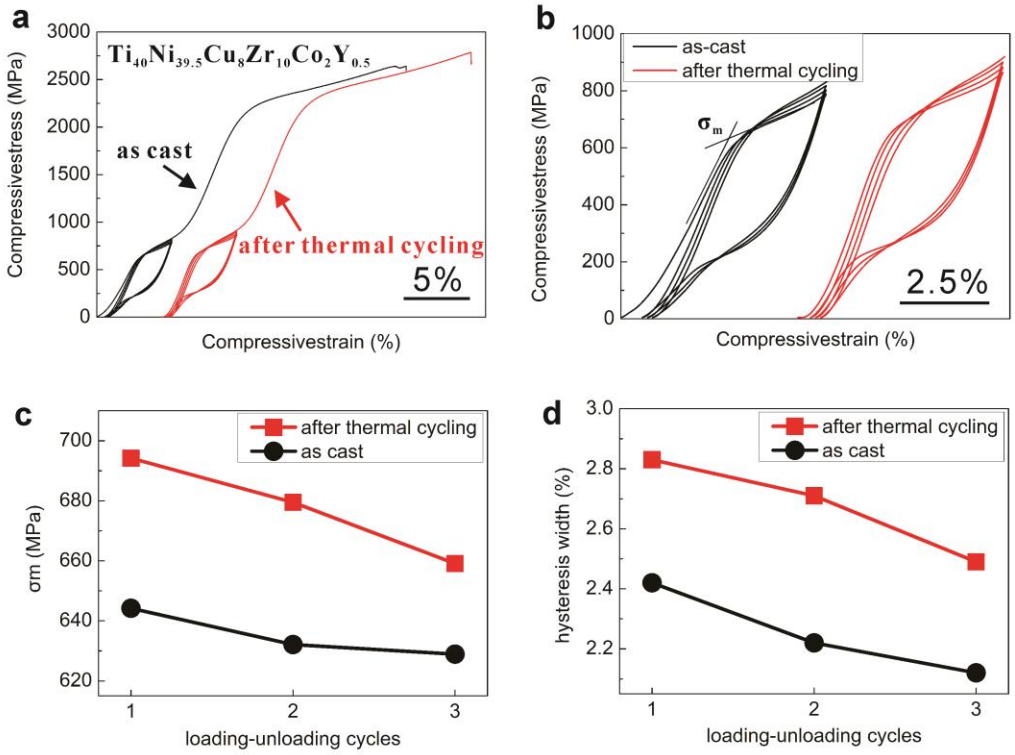

Fig. 5.3. The mechanical behavior compared the as cast state and cryogenic thermal cyclic state of TiNi crystalline/amorphous alloys

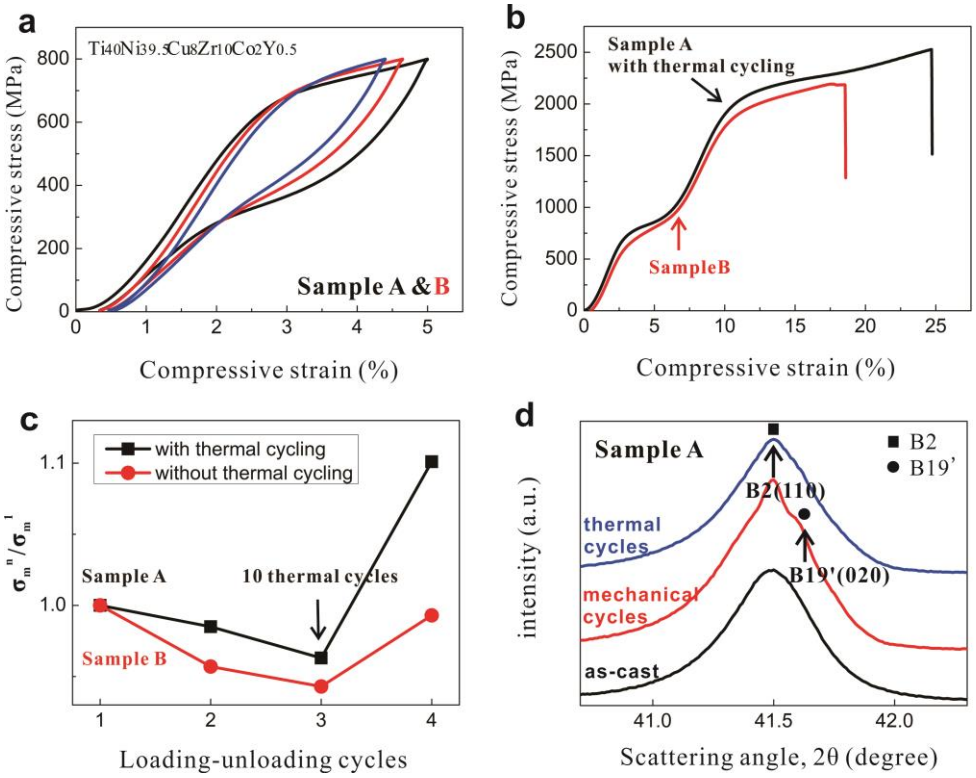

Fig. 5.4. The mechanical behavior shows the effect of thermal cycling on the mechanical cyclic

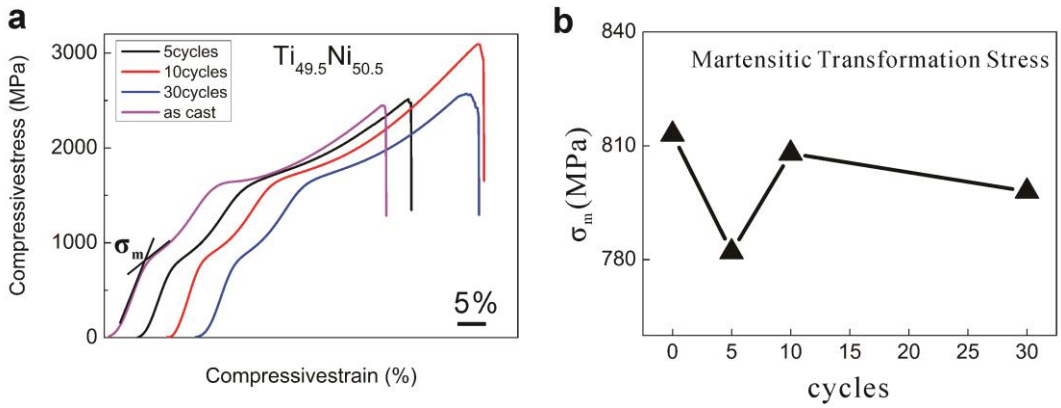

Fig. 5.5. The compressive stress strain curves of the $Ti_{49.5}Ni_{50.5}$ fully crystalline alloys with different cycles of cryogenic thermal cycling (a), and the coressponding critial stress for martensitic phase transformation, σ_m, functioned with the thermal cyclic number increase (b).

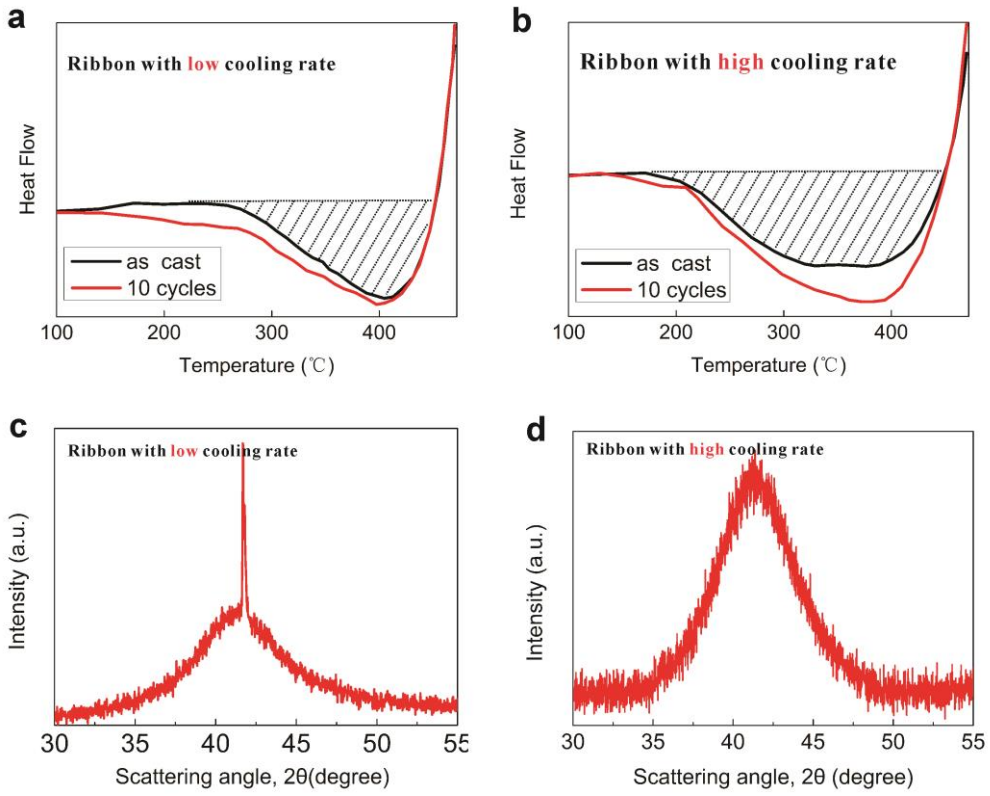

Fig. 5.6. The differential scanning calorimetry (DSC) traces of heating the melt-spun TiNi ribbons (a,b) and the corresponding XRD patterns (c,d) of TiNi ribbons with different cooling rate

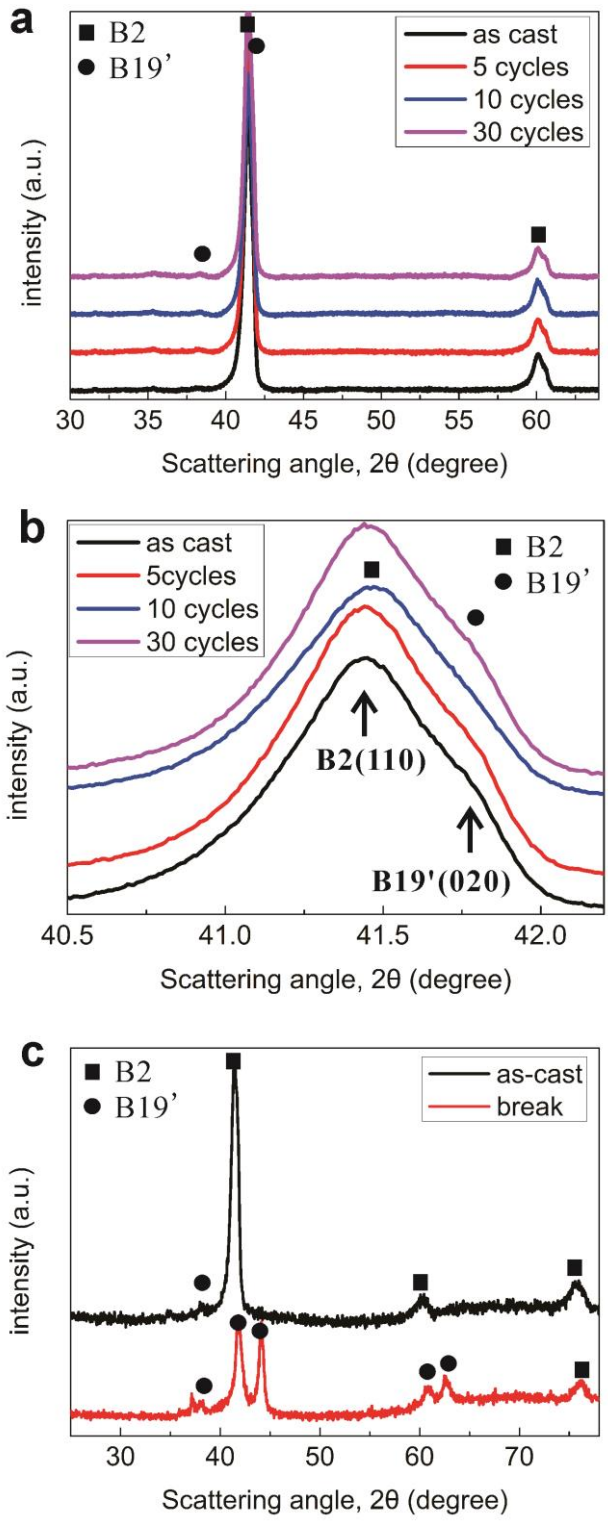

Fig. 5.7. XRD patterns of the the TiNi cyrstalline/amorphous alloys with different cycles of cryogenic thermal cycling (a), the magnified patterns between 2θ of 41 degree and 42degree (b) and the patterns of fracture surface (c).

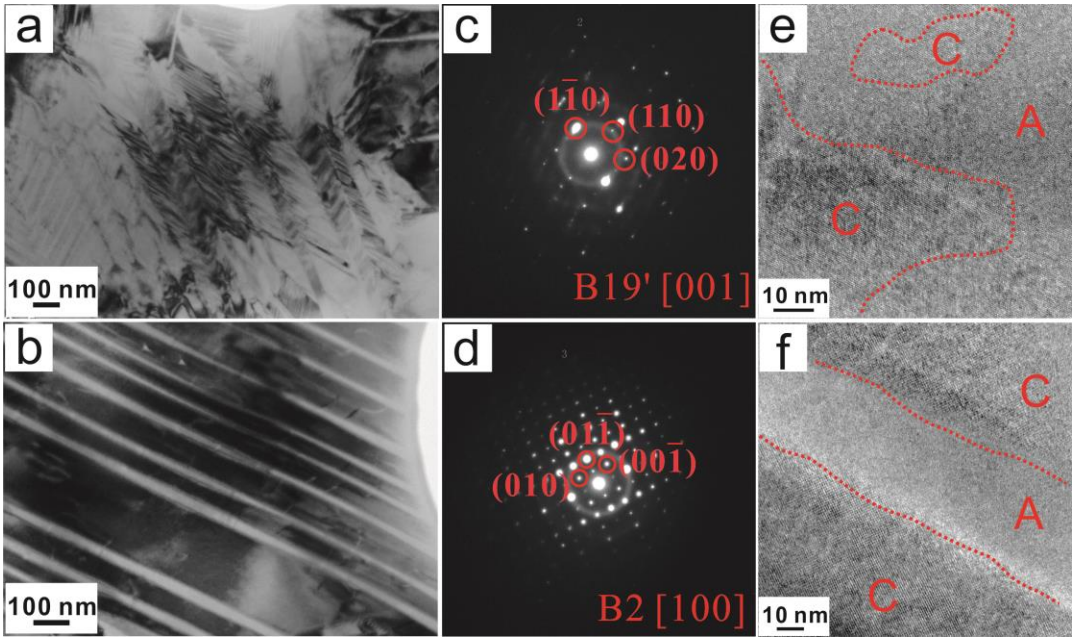

Fig. 5.8. TEM images of light field of TiNi crystalline/amorphous alloys in (a) as cast state and (b) cryogenic thermal cyclic state (10cycles). Corresponding SAED patterns (c,d) and high-resolution images (e,f), respectively.

Chapter 6

Conclusions

TiNi based BMG composites which have dual crystalline and amorphous phases were fabricated with excellent mechanical properties, combining a fairly strain of 20% in ductility and a high stress of 2300 MPa in strength. The compressive stress-strain curves has a double sigmoidal shape with three deformation stages, an elastic deformation stage, a plateau stage of martensitic transformation process and final plastic deformation stage. The critical stress inducing the plateau stage of phase transformation is defined as the martensitic phase transformation stress, σ_m, which is one of the most typical factors to demonstrate the mechanical properties of the TiNi crystalline/amorphous alloys. The crystalline phases in the as cast state include a high temperature stable austenite B2 phase and a low temperature stable martensite B19' phase which always appears near amorphous phase. The thermal induces phase transformation between TiNi austenite phase and martensite phase, the austenitic transformation start temperature (As) is around 260K and finish temperature (Af) is near 285K. Most measurements were performed at room temperature of 295K where the crystalline phase is stable in the austenite B2 phase. This study was carried out comprehensively from alloys synthesis and characterization to investigation of controlling the amorphous phase and crystalline phase in the alloys, the effects of different phase on the mechanical properties, finally improve the mechanical properties. The main findings are described separately as the follows:

1. The cooling rate employed during casting process affects the fraction of amorphous phase and induces differences in the crystalline phases. The mechanical properties perform distinguishing in the rod samples with different diameters since the different cooling rate. Compared with the larger rods formed at lower cooling rates, the smaller rods formed at higher cooling rates contains higher volume fraction of amorphous phase. The present of amorphous phase surrounding the crystalline phases confines the phase transformation between austenite and martensite. Thus, the smaller sample which including more amorphous phase shows a higher critical phase transformation stress during the compressive deformation.
2. High pressure torsion (HPT) process induces severe plastic deformation in the TiNi crystalline/amorphous alloys, leading to broaden of peaks in XRD patterns. The phase composition was controlled by HPT process at different temperatures, HPT process at 77K induces the main austenite phase change to martensite phase but the room temperature processed HPT keeps the austenite phase. The microstructure reveals an increasing volume fraction of amorphous phase by the HPT process.
3. TiNi crystalline/amorphous alloy exhibits a martensitic transformation behavior which induces superelastic effect in the deformation process. Cyclic loading-unloading behavior performing in the superelastic mode leads to the low cycle mechanical fatigue. Typical properties of the mechanical fatigue are shown as: the critical phase transformation stress (σ_m) and hysteretic width of each cycle

decrease, the residual stain increases with the cyclic numbers increase. The low cycles mechanical-fatigue properties during cyclic loading perform different in TiNi-BMGCs alloy and TiNi fully crystal alloy. A decrease in σm and hysteresis area in the TiNi crystalline-amorphous alloy suppressed due to the presence of the amorphous phase which acts as a sink for dislocations generated upon the superelastic cycling. It prevents the accumulation of dislocations, and simultaneously promotes creation of the new dislocations. The amorphous phase in TiNi BMGCs assists to the smooth progress of the martensitic transformation.

4. Cryogenic thermal cycling performing on the BMGs induces a rejuvenation effect. The mechanical properties of TiNi crystalline/amorphous alloy also show differences by the cryogenic thermal cyclic processing. The compressive stress strain curves display an increase of the critical stress (σ_m) for martensitic phase transformation which is the opposite behavior with the low cycles mechanical fatigue. The presence of amorphous phase in the TiNi crystalline/amorphous alloys acts as an important factor to responsible for the increase of σ_m by the cryogenic thermal cycling. The amorphous phase appears around the B19' martensite phase after casting and restrict the phase transform to B2 austenite phase, so the peak of low temperature stable martensite phase shows in the XRD patterns. After cryogenic thermal cycling the fraction of initial martensite phase reduces. The thermal treatment activates the initial martensite phase and enable it transform into the high temperature stable austenite phase during the cycling. The tendency of martensite volume fraction decrease is corresponding to the increase

of phase transformation stress (σ_m). On the other hand, the microstructure of crystal near the amorphous phase transformation could be found in the TEM images. The as cast state twinning martensite phase changes to austenite phase with lamellar structure. The layer-type structure blocks the movement of dislocation which is also the reason that increases the stress for phase transform.

Publications

1. **J. Jiang,** S. Ketov, H. Kato, D.V. Louzguine-Luzgin, Effect of the cooling rate on the mechanical properties of Ti-Ni-Cu-Zr-based crystal/glassy alloys, Materials Science & Engineering A, 704 (2017) 147-153.
2. **J. Jiang**, D.X. Wei, T. Wada, D.V. Louzguine-Luzgin, H. Kato, The mechanical cycling behavior of TiNi based crystal/glassy alloy in the superelastic mode, Journal of Alloys and Compounds, 768 (2018) 176-180.
3. D.V. Louzguine-Luzgin, M.Yu. Zadorozhnyy, S.V. Ketov, **J. Jiang**, I.S. Golovin, A. S. Aronin, Materials Science & Engineering A, 742 (2019) 526-531.
4. S. Ketov, **J. Jiang**, D.V. Louzguine-Luzgin, J. Eckert, J. Orava, A. Greer, *et. al*, On cryothermal cycling as a method for inducing structural changes in metallic glasses, NPG Asia Materials, (2018) 10: 137-145.
5. D.V. Louzguine-Luzgin, M. Ito, S. Ketov, A. Trifonov, **J. Jiang**, C.L. Chen, K. Nakajima, Intermetallics, 93 (2018) 312-317.
6. G.H. Zhao, S. Ketov, **J. Jiang,** H. Mao, A. Borgenstam, D.V. Louzguine-Luzgin, New beta-type Ti-Fe-Sn-Nb alloys with superior mechanical strength, Materials Science & Engineering A, 705 (2017) 348-351.
7. S.L. Zhu, **J. Jiang**, X. Zhang, Y.Q. Liang, Z.D. Cui, X.J. Yang, Novel nanosized anatase TiO_2 hexagonal prism filled with nanoporous structure, Materials and Design, 116 (2017) 238-245

Acknowledgements

First of all, I would like to sincerely thank my supervisor, Prof. Kato, for his valuable guidance, constructive suggestions throughout my three years PhD study. Not only the help in research and study, also in the daily life. I've obtained a lot of important experience which will benefit to my whole life. Prof. Kato is a good the scientist and an optimistic humor professor, with his encourage I have had a wonderful PhD life in Japan as a foreigner.

At same time, I want to thank Prof. Louzguine who gave me a lot of fundamental knowledge and experimental skills. The enthusiasm and attitude to do the scientific research that I've learn from Prof. Louzguine will greatly benefit my future academic career. He never had a problem praising me or offering encouragement to my work, even I know it's not always satisfactory, but these positive encourage really gave me confidence to face the problems that I could meet in the research and study.

Secondly, I would like to thank the distinguished thesis committee members, Prof. Chiba and Prof. Saida, for their invaluable time and helpful suggestions on my thesis.

I'm very grateful to Assoc. Prof. Wada and Assis. Prof. Joo, for their technical support with my experiments and the constructive discussions. They gave me a lot of valuable suggestions during my PhD study.

I want to take this opportunity to thank my colleagues in Kato-lab for their help and support during the three years. The secretary Ito san and the students: Dr. Liang, Dr. Park, Dr. Date, Dr. Gerelmaa, Ms. Noguchi, Ms. Kamata, Ms. Suga, Ms.Shoji, Ms.Sato, Ms. Kato and Ms. Chen.

During the three years life in Japan, I got many concern and help from Chinese friends and senior, I want to express my deeply thanks for you all to give me good memory and colorful life in the foreign country. Assis. Prof. Y. Zhang Dr.Lu, Dr.Wei and his wife Mrs. Jiang, Dr. Han, Dr. F. Zhang.

Finally, I would like to thank my families, my father, mother, brother and husband. Without your love I cannot successfully finish my study in Japan, even they all stay in China, but always concern about me and give me the energy. I’m very appreciate your support. You are the most important for me in my life.